

DESIGN OF NOVEL RF COILS FOR SIGNAL-TO-NOISE RATIO
IMPROVEMENT IN NMR

BY

WENHUA X. NI

A DISSERTATION PRESENTED TO THE GRADUATE SCHOOL
OF THE UNIVERSITY OF FLORIDA IN PARTIAL FULFILLMENT
OF THE REQUIREMENTS FOR THE DEGREE OF
DOCTOR OF PHILOSOPHY

UNIVERSITY OF FLORIDA

1997

ACKNOWLEDGMENTS

I would like to thank my research supervisor, Dr. Thomas Mareci, for his patience with me over the years, as well as his guidance and encouragement throughout my graduate career. Without his help, this thesis would be impossible. I would also like to express my sincere gratitude to Dr. Edward Wirth and Dr. Randy Duensing for their tremendous help during my research career. I appreciate the many hours spent with Dr. Randy Duensing on the discussion of coil design principles and thank him for sharing his expertise with me. Dr. Neil Sullivan is thanked for his caring help. It was Professor Raymond Andrew's inspiring lecture in China that brought me here. I thank him for that, and for his insights. I owe him dearly. Dr. Steve Blackband, a new addition to our group, is thanked for his kind help.

I express my sincere thanks to many colleagues who have truly made my stay at the University of Florida something that I will remember fondly for years to come. I would like to express my gratitude to Xeve Silver for his help in surgery and coil construction. I would like to thank Benjamin Inglis for his help on localized spectroscopy techniques. Thanks also go to Jon Bui and Beth Bossart for their encouragement and all the good time we have had. I would like to thank Debra Neil-Mareci for her expert assistance with the drawings in my dissertation. I would also like to extend my gratitude to Michel Bisset for his help to acclimate to American life and being my best friend during the years that I stayed in Hawaii. I would like to thank Jackie Combs, Carol

Tsekouras, Haiquan Dai, Mark Hubley, David Peterson, Dan Plant and Jim Rocca for their friendship. I would like to thank Professor Linxian Zhou, for all his advice and encouragement during my graduate study in Xiamen, China. I would also like to give my special thanks to Mr. Junsheng Zeng, Mr. Yourong Huang, Mr. Jintau Huang and Mr. Kwok Kwok Yu for their great help in my effort to come to the United States to pursue my Ph.D. Without their help this dream would not have been possible.

This thesis is dedicated to my mother, Qinfang Ye, who has been an unceasing source of support throughout my life and my long collegiate career. She has always encouraged me to pursue whatever I wished. For this I can never thank her enough. I thank my brothers and sisters for the love and support that they have given to me all these years. I also thank my sisters and brothers in the Lord, especially Tingting Cai and Dr. Jin-wen Hsu, for their love and encouragement.

My special gratitude must go to my husband, Dr. Wenhui Ni, for his love, support, patience, understanding, encouragement, sharing, and advice during my research and thesis preparation.

Finally I would like to thank God, who is my helper and the source of strength in my life.

TABLE OF CONTENTS

	<u>page</u>
ACKNOWLEDGMENTS.....	.ii
TABLE OF CONTENTS.....	.iv
LIST OF TABLES.....	.vi
LIST OF FIGURES.....	.vii
ABSTRACT.....	.x
CHAPTERS	
I. INTRODUCTION.....	1
The Principle of Nuclear Magnetic Resonance.....	1
Signal-to-Noise Ratio.....	7
II. RF COIL DESIGN PRINCIPLES.....	10
Introduction.....	10
Magnetic Field and Homogeneity.....	14
Impedance Matching.....	17
Coupling.....	22
Decoupling.....	30
III. IMPLANTED ^{31}P RF COILS.....	36
Introduction.....	36
Review of Literature.....	38
Methods.....	43

Simulation.....	43
RF Coil Designs.....	44
Magnetic Resonance Spectroscopy and Imaging.....	51
Surgical Procedures and RF Coil Implantation.....	53
Results.....	54
Coil Optimization.....	54
Contamination.....	62
Susceptibility and Coupling between ^1H and ^{31}P Implanted Coil.....	69
Test of ^{31}P RF Coil Implanted on a Rat Spinal Column.....	85
Conclusion.....	93
IV. QUADRATURE INDUCTIVELY COUPLED IMPLANTED RF COILS.....	94
Introduction.....	94
Review of Literature.....	94
Method.....	97
Simulations.....	97
RF Coil Design.....	101
Results.....	113
Discussion.....	130
Conclusion.....	133
V. CONCLUSION.....	134
Applications of Implanted ^{31}P Coils in Rat Spinal Cord Injury and Repair.....	134
Applications of Quadrature Inductively-Coupled Implanted Coils in Cat Spinal Cord Injury and Repair.....	135
Future of Implanted Coil Development.....	137
APPENDIX.....	138
REFERENCES.....	144
BIOGRAPHICAL SKETCH.....	150

LIST OF TABLES

<u>Table</u>	<u>Page</u>
3-1. SNR comparison between different ^{31}P implanted coils and surface coil.....	56
4-1. Inductance matrix of a quadrature inductively-coupled implanted coil.....	115
4-2. Coupling constant between coils in a quadrature implanted coil system.....	115
4-3. SNR comparison between a coil with a conventional balanced matching circuit and a coil with a balanced matching circuit.....	129
4-4. SNR (measured on a 1 cm tube phantom) comparison between the four coil systems and the linear surface coil.....	129
4-5. SNR (measured on a cat phantom) comparison between the four coil systems and a linear surface coil.....	129

LIST OF FIGURES

<u>Figures</u>	<u>page</u>
2-1 Coordination in a single-turn flat circular coil.....	15
2-2 Coordination in a half-saddle coil.....	15
2-3 Transmissions line with a load of impedance Z_L	17
2-4 Conventional matching circuit.....	20
2-5 Conventional balanced matching circuit.....	20
2-6 Balun matching circuit	21
2-7 Balanced matching circuit.....	21
2-8 Schematic diagram of an inductively coupled coil system.....	22
2-9 Schematic diagram for the signal-to-noise ratio simulation of an inductively coupled coil system.....	29
3-1. Schematic diagram of an inductively coupled ^{31}P implanted coil.....	45
3-2 Schematic diagram of an inductively coupled ^{31}P implanted coil using crossed diode decoupling scheme.....	46
3-3 Schematic diagram of an inductively coupled ^{31}P implanted coil using resonant block decoupling scheme.....	47
3-4 Position of the ^{31}P implanted coil.....	52
3-5 B_{xy} at the center cross-section of the 3 cm x 3 cm external ^{31}P coil.....	57
3-6 Current in an external coil and current induced from an external coil to an implanted coil without using any decoupling scheme.....	59
3-7 Current induced from an external coil to an implanted coil using crossed diode decoupling scheme.....	60

3-8	Current induced from an external coil to an implanted coil and its decoupling loop, where resonant blocking decoupling scheme is used.....	61
3-9	Transverse image of a rat phantom.....	63
3-10	^{31}P spectra of a rat phantom taken with the 3 cm x 3 cm surface coil.....	64
3-11	^{31}P spectra of a rat phantom taken with a directly driven implanted coil.....	65
3-12	^{31}P spectra of rat phantom taken with an inductively coupled implanted coil.....	66
3-13	Transverse image of a rat phantom with the “tissue” surrounding the “spinal cord” resected.....	67
3-14	^{31}P spectra taken with an inductively coupled implanted coil from a “rat” phantom with the surrounding “tissue” retracted.....	68
3-15	Localized ^{31}P spectrum from a rat phantom.....	70
...		
3-16	Transverse and sagittal ^1H images of rat spinal column with an inductively coupled coil implanted on rat spinal cord	71
3-17	Susceptibility distortion caused by a capacitor on a 200 MHz system.....	74
3-18	Susceptibility and RF field distortion caused by a copper wire loop on a 300 MHz system.....	79
3-19	Coupling between a 4 cm x 4 cm ^1H surface coil and a 4 mm x 5 mm ^{31}P implanted coil.....	83
3-20	Sagittal image of a rat with a ^{31}P coil implanted on the spinal cord.....	84
3-21	^{31}P spectra of a dead rat taken with an inductively coupled implanted transmit/receive ^{31}P coil.....	88
3-22	<i>In vivo</i> ^{31}P spectra of a rat taken with an inductively coupled Implanted transmit/receive ^{31}P	89
3-23	<i>In vivo</i> ^{31}P spectrum of a rat taken with an inductively coupled implanted receive-only ^{31}P coil	90
3-24	Image of a rat with a receive-only ^{31}P coil coated with PMMA in dome shape and implanted on the spinal cord.....	91
3-25	<i>In vivo</i> ^{31}P spectrum of a rat taken with and inductively coupled	

implanted receive-only ^{31}P coil coated with PMMA in dome shape.....	92
4-1 Configuration of an inductively-coupled quadrature implanted coil.....	99
4-2 Configuration of a quadrature implanted coil.....	100
4-3 Configuration and schematic diagram of a transmit-only and receive-only linear surface coil pair.....	103
4-4 Configuration and schematic diagram of a transmit-only linear surface coil and receive-only quadrature surface coil.....	105
4-5 Configuration and schematic of an inductively coupled linear implanted coil.....	107
4-6 Schematic diagram of a quadrature inductively coupled implanted coil.....	109
4-7 B_1 field mapping of a 14 cm x 20 cm transmit-only linear surface coil.....	116
4-8 B_1 field mapping of a 10 cm x 6 cm receive-only linear surface coil.....	117
4-9 Cross sectional B_1 field mapping of a quadrature inductively coupled implanted coil.....	118
4-10 Comparison of the direct coupling and crossed coupling constant of a quadrature implanted coil.....	119
4-11 Direct and crossed coupling constants varied with distance.....	120
4-12 SNR comparison between a coil with a conventional balanced matching circuit and a coil with a balanced matching circuit.....	122
4-13 SNR comparison (measured on a 1 cm tube phantom) between the four coil systems.....	123
4-14 SNR comparison (measured on a 1 cm tube phantom) between the quadrature surface coil and the linear surface coil.....	124
4-15 Images of a cat phantom taken with the four coil systems.....	125
4-16 SNR comparison (measured on a cat phantom) between the four coil systems.	126
4-17 SNR comparison (measured on a cat phantom) between the quadrature surface coil and the linear surface coil the.....	127
4-18 Comparison of the excised rat spinal cord images taken with the four coil systems.....	128

Abstract of Dissertation Presented to the Graduate School
of the University of Florida in Partial Fulfillment of the
Requirements for the Degree of Doctor of Philosophy

DESIGN OF NOVEL RF COILS FOR
SIGNAL-TO-NOISE RATIO IMPROVEMENT IN NMR

By

Wenhua Xu Ni

December, 1997

Chairman: Professor Thomas Mareci
Major Department: Physics

In this thesis, two different novel RF coils were designed to improve the available signal-to-noise ratio (SNR) in nuclear magnetic resonance (NMR) spectroscopy and imaging. One of them was an inductively coupled ^{31}P implanted coil. The other was an inductively coupled quadrature ^1H implanted coil.

The ^{31}P implanted coil was inductively coupled to an excitation/reception external coil and placed directly above the spinal cord of a rat to restrict the field of view (FOV) to the region of interest (ROI). The ^{31}P implanted coil had a resonant blocking circuit to decouple this coil from the external coil during transmission so that excitation was uniform in the ROI. A quadrature ^1H surface coil was mounted over the ^{31}P external coil for the acquisition of NMR images and shimming. Good quality ^{31}P spectra from ROI were obtained with the ^{31}P coil implanted over a rat's spinal cord. Therefore the ^{31}P

implanted coil could be used to study changes in metabolites of a rat's spinal cord after injury and repair.

The first quadrature implanted coil, which was receive-only and inductively coupled to an excitation/reception external quadrature coil, was designed. The SNR of this implanted coil was measured on a cat phantom and compared with that of an optimized linear surface coil, a quadrature surface coil or an inductively coupled linear implanted coil. In the ROI (i.e., a cat spinal cord), the quadrature implanted coil exhibited a factor of 7.04 increase in SNR relative to the linear surface coil; a factor of 4.48 relative to the quadrature surface coil and a factor of 2.59 relative to the linear implanted coil. The improved SNR for an inductively coupled quadrature implanted coil was observed as a dramatic improvement in the clarity of the images of an excised rat spinal cord. The high SNR available with the inductively coupled quadrature implanted coil allows the acquisition of high resolution NMR images and opens up the possibility of measuring localized spectroscopy *in vivo* within the spinal cord.

CHAPTER I INTRODUCTION

The Principle of Nuclear Magnetic Resonance

Magnetic resonance (MR) is a phenomenon found in magnetic systems that possess both magnetic moments and angular momentum. The significant property of a nucleus for the measurement of nuclear magnetic resonance (NMR) signal is the intrinsic angular momentum or spin of the nucleus. Here quantum mechanical theory is used to describe the principle of NMR.

The application of a magnetic field \vec{B} produces interaction energy with the nucleus of amount $-\vec{\mu} \cdot \vec{B}$, where $\vec{\mu}$ is the magnetic moment in a small volume at a point and $\vec{\mu} = \gamma \hbar \vec{I}$, where γ is the gyromagnetic ratio, \hbar is the Planck constant divided by 2π and \vec{I} is the spin of a nucleus. Therefore, a very simple Hamiltonian is obtained,

$$H = -\vec{\mu} \cdot \vec{B}. \quad [1-1]$$

If the field of magnitude B_0 is along z-direction, then

$$H = -\gamma \hbar B_0 I_z. \quad [1-2]$$

Therefore the allowed energies are

$$E = -\gamma \hbar B_0 m, \text{ where } m=-I, I-1, \dots, I. \quad [1-3]$$

To be able to detect the presence of such a set of energy levels an alternating magnetic field, which is a radio frequency (RF) magnetic field produced by an RF coil,

has to be applied perpendicular to the static field B_0 . The RF coil is the "antenna" of the MRI system that broadcasts the RF signal to the subject under study and/or receives the return signal and can be transmit and receive (transceiver) or receive-only, in which case another coil is used as a transmitter. If the RF field is $\vec{B}_1 \cos \omega_0 t$, a perturbing term will be obtained,

$$H_{\text{pert}} = -\gamma \hbar B_1 I_x \cos \omega_0 t. \quad [1-4]$$

From time-dependent perturbation theory, the interaction H_{pert} induces a transition from state m with energy E_m to state m' with energy $E_{m'}$. The probability per second $P_{m \rightarrow m'}$ is

$$P_{m \rightarrow m'} \propto | \langle m | I_x | m' \rangle |^2 \delta(E_{m'} - E_m - \hbar\omega), \quad [1-5]$$

where $\langle m' | I_x | m \rangle$ vanishes unless $m' = m \pm 1$. Consequently the allowed transitions are between levels adjacent in energy, giving

$$\hbar\omega_0 = \Delta E = \hbar\gamma B_0 \quad [1-6]$$

or

$$\omega_0 = \gamma B_0. \quad [1-7]$$

The effect of an RF magnetic field $\vec{B}_1(t) = \vec{B}_1 \cos \omega_0 t$ can also be analyzed by breaking it into two rotating components, each of amplitudes B_1 , one rotating clockwise and the other counterclockwise.

$$\vec{B}_1 = B_1 (\vec{i} \cos \omega_z t + \vec{j} \sin \omega_z t), \quad [1-8]$$

where $\omega_z = \pm \omega_0$, $+\omega_0$ is for clockwise and $-\omega_0$ is for counterclockwise. Near resonance the counterclockwise component may be neglected. The total field $\vec{B}(t)$ is then

$$\vec{B}(t) = B_1(\vec{i} \cos \omega_0 t + \vec{j} \sin \omega_0 t + \vec{k} B_0), \quad [1-9]$$

and the Schrödinger equation is

$$-\frac{\hbar}{i} \frac{\partial \Psi}{\partial t} = -H\Psi = -\gamma\hbar[B_0 I_z + B_1(I_x \cos \omega_0 t + I_y \sin \omega_0 t)]\Psi. \quad [1-10]$$

If resonance occurs when $\omega_0 = \gamma B_0$, then (Slichter, 1989)

$$\Psi(t) = e^{-i\omega_0 t I_z} e^{-(i/\hbar)H't} \Psi'(0), \quad [1-11]$$

where $H' = -\gamma\hbar B_1 I_x$. Thus (Slichter, 1989)

$$\langle \mu_z(t) \rangle = \int \Psi^*(t) \mu_z \Psi(t) d\tau = \langle \mu_z(0) \rangle \cos \gamma B_1 t. \quad [1-12]$$

For a unit volume we can obtain

$$M_z(t) = M_0 \cos \gamma B_1 t, \quad [1-13]$$

where M_0 is the thermal equilibrium magnetization and $M_0 = M_z(0)$. Similarly we can obtain

$$M_y(t) = M_0 \sin \gamma B_1 t \cos \omega_0 t, \quad [1-14]$$

$$M_x(t) = M_0 \sin \gamma B_1 t \sin \omega_0 t. \quad [1-15]$$

In this thesis we will be studying proton (1H) and phosphorus (^{31}P) nuclei which have a spin $I=1/2$. Under a static magnetic field, the nuclei are allowed in two different energy states α : $m=-1/2$ and β : $m=1/2$. The thermal equilibrium magnetization, M_0 , of the sample is the resultant of the individual magnetic moments $\vec{\mu}$. At equilibrium, M is along the $+z$ direction and has a magnitude

$$M_0 = n_\alpha \langle \mu_\alpha \rangle + n_\beta \langle \mu_\beta \rangle = n_\alpha \langle \mu_{z\alpha} \rangle + n_\beta \langle \mu_{z\beta} \rangle = \frac{1}{2} \gamma \hbar (n_\alpha - n_\beta), \quad [1-16]$$

where n_α and n_β are the populations per unit volume, μ_α and μ_β are the magnetic moments in the two α and β energy states. It is shown in statistical mechanics that, at high temperature T ($\sim 300^0$ K), the final equilibrium populations n_α and n_β are given by

$$\frac{n_\alpha}{n_\beta} = e^{\Delta E / \kappa T}, \quad [1-17]$$

where κ is the Boltzmann's constant. For a sample containing N magnetic moments per unit volume $n_\alpha + n_\beta = N$, and thus

$$M_0 = \frac{1}{2} \gamma \hbar N \frac{e^{\Delta E / 2\kappa T} - e^{-\Delta E / 2\kappa T}}{e^{\Delta E / 2\kappa T} + e^{-\Delta E / 2\kappa T}} \quad [1-18]$$

However, for nuclei, the ratio $\Delta E / 2\kappa T$ is a very small number, $(n_\alpha - n_\beta)/N$ is typically on the order of 10^{-5} for typical NMR situations which is the root of the problem of sensitivity in NMR. Therefore a linear expansion of the Boltzmann exponential can be used and the magnetization becomes

$$M_0 = \frac{N(\gamma\hbar)^2 B_0}{4\kappa T}. \quad [1-19]$$

It can be seen that after B_1 is applied on resonance for duration τ , such that the angle of rotation about B_1 becomes $\Theta = \gamma B_1 \tau = \frac{\pi}{2}$ (90^0 pulse), and the magnetization can be written as

$$M_z(t) = 0, \quad [1-20]$$

$$M_y(t) = M_0 \cos \omega_0 t, \quad [1-21]$$

$$M_x(t) = M_0 \sin \omega_0 t. \quad [1-22]$$

The magnetization is in the x-y plane. Following the cessation of the B_1 field, the magnetic moment will precess in the laboratory frame of reference in a plane normal to the static field. As a result, the moments will produce a flux through an RF coil that will alternate as spins precess. From Equations [1-20] to [1-22], we can see that \vec{M} rotates in the x-y plane at rate ω_0 and the dot product, $\vec{B}_1 \bullet \vec{M}$, varies as $\cos \omega_0 t$. So the resultant induced electromagnetic force (EMF) from sample volume V_s is

$$e_S = - \int_{\text{sample}} (\partial / \partial t) (\vec{B}_1 \bullet \vec{M}) dV_s = G\omega_0 (B_1)_{xy} M_0 V_s \cos \omega_0 t \quad [1-23]$$

Thus after a 90° pulse, the magnitude of the induced EMF in the receiving RF coil is

$$E_S = G\omega_0 (B_1)_{xy} M_0 V_s = G\gamma B_0 (B_1)_{xy} \frac{N(\gamma\hbar)^2 B_0}{4kT} V_s = G\gamma^3 B_0^2 (B_1)_{xy} \frac{N(\hbar)^2}{4kT} V_s, \quad [1-24]$$

where G is a numerical factor depending on the receiving coil geometry. So far the EMF would persist indefinitely, but in practice, interactions cause the magnetization to decay. One interaction is between the spin and its surroundings or lattice, which is termed the spin-lattice relaxation; the relaxation time constant of this process is called T_1 . The other interaction is between spins, which is termed spin-spin relaxation and has the exponential time constant T_2 .

The local magnetic field of a nucleus is responsible for the exact Larmor frequency of the particular spin moment. This is described by the chemical shift that is the frequency difference of a particular nucleus compared to some standard. This property along with many other more complicated interactions involving relaxation time differences, and coupling between nuclei through a number of different mechanisms, allow precise characterization of local chemical environments and thus chemical structure.

Since ^1H concentration is much higher than other nuclei ^1H magnetic resonance image (MRI) is often used to observe the nuclear distribution without regard to small environmental differences between nuclei. The common experiments produce contrast through differences in spin density, T_1 and T_2 . To produce a one-dimensional picture of the spin density in a sample, a strong linear gradient of magnetic field is added to the homogeneous main field. This serves to spread the frequency to such an extent that chemical shift differences are normally unnoticeable. Furthermore the frequency differences encode the spatial dimension and allow an image of the material to be produced. The most basic imaging sequence currently used involves the use of the magnetic field gradient described above for the frequency encoding in one dimension and then a repetitive gradient that varies incrementally with an acquisition at each step. This gradient set produces phase encoding and allows an inversion via Fourier transform to the two spatial dimensions.

From the results above it can be seen that

- I. The strict proportionality of E_s to N makes NMR useful for quantitative studies, such as the metabolic changes observed in a spinal cord after it is injured or repaired.
- II. The heavy dependence on γ infers that those nuclei resonating at high frequencies tend to have a relatively intense signal. Proton has the highest abundance and γ (except for radioactive tritium) (Harris, 1983), so it is the most popular study object in NMR imaging.

Signal-to-Noise Ratio

Regardless of whether electric current is flowing in a resistor, the electrons undergo random Brownian motion, which may be detected as a tiny, randomly varying voltage across the ends of the resistor. The variation of the voltage is called Johnson noise. This Johnson noise places a lower limit upon the size of a signal that may be detected in the presence of the resistance (Chen, Hoult, 1989). The power dissipated in a coil increases the resistance in a coil and the power can be lost in four fundamental ways. First, the coil may be made of a non-superconducting material that infers ohmic losses in the conductor. The electrical element that dissipates energy by ohmic processes is the resistance. This is worsened by the skin effect. The skin depth decreases as $\omega^{1/2}$ that implies that the resistance increases as $\omega^{1/2}$. Of course, no inductor or capacitor is free of resistance, unless it happens to be made of superconducting material and, even then, it may exhibit a small resistance to alternating current. Second, there will be non-conservative electric fields associated with the coil components. If a sample is conductive this electric field will deposit power in the sample. Third, the magnetic field that is the primary property of interest of the coil will also generate eddy currents in a conducting sample that represents power loss. Fourth, tissue can radiate energy as an antenna. When the size of the sample becomes comparable to a wavelength, the radiation is an important term and the signal induction formula must be modified.

If a coil is in thermal contact with the sample, the total noise voltage of the coil will be (Murphy-Boesch, 1985)

$$E_N = \sqrt{4kT_s R \Delta f}, \quad [1-25]$$

where the Δf is the bandwidth, in Hertz, of the measuring equipment, T_s is the sample temperature and R is the resistance of the coil, including the resistances associated with all losses. From Eq. [1-24] and Eq. [1-25], the signal-to-noise ratio (SNR) can be calculated as

$$\text{SNR} = \frac{E_S}{E_N} \propto GM_0\omega_0(B_1)_{xy}V_s \sqrt{\frac{1}{4\kappa T_s R \Delta f}}. \quad [1-26]$$

It can be rewritten as (Hoult, Richards, 1976)

$$\text{SNR} = G\eta M_0 \sqrt{\frac{\mu_0 \omega_0 Q V_c}{4F\kappa T_s \Delta f}}, \quad [1-27]$$

where η is the "filling factor," i.e., a measure of the fraction of the coil volume occupied by the sample; μ_0 is the permeability of free space; Q (with the sample loaded) is the quality factor of the coil; V_c is the volume of the coil and F is the noise figure of the preamplifier.

Due to the low concentrations of biochemical compounds in tissue, it is important to optimize the SNR of NMR signals, especially when higher resolution and/or shorter scan times are required. We may consider that the primary factors involved in any analysis of SNR are those contained within the Eq. [1-27], whether or not the quadrature detection and/or decoupling are used. Secondary factors, such as the availability of Fourier transform techniques, though of great importance, are not of such a fundamental nature and will not further be considered.

From Eq. [1-27], we can see that the SNR available is proportional to $\omega_0^{3/2}$ (M_0 increases linearly with B_0 and thus ω_0). The inverse proportionality to T_s indicates that low temperature operation is desirable, but in practice questions of solubility or freezing

put a strict limit to the utility of this statement for solution-state studies. The filling factor and the quality value Q of a coil can be improved by optimizing the coil design.

CHAPTER II RF COIL DESIGN PRINCIPLES

Introduction

Factors important in RF coil design optimization include field homogeneity, sensitivity, tuning, matching, balancing, radiation, sample loading, multiple coil interactions, the susceptibility of the material used for the implanted coil, and the proper size and location of the coil. The magnetic field of an RF coil should be perpendicular to the static field and homogeneous across the region of interest (ROI). The receiver coil must be sensitive to the NMR signal within the ROI, and at the same time be as insensitive as possible to the noise from any sources other than the ROI. The coil should be matched to the optimum noise figure of the preamplifier (Peterson et al., 1997), tuned to the frequency of the nuclei in the magnet, and, if possible, electrically balanced (Murphy-Boesch, Koretsky, 1983). An RF coil should inductively couple to a conductive sample; therefore, the power should dissipate primarily in the near field close to the conductor. In an effort to achieve high sensitivity and homogeneous magnetic fields, multiple coils can be used. With this method, decoupling schemes should be applied to remove the interaction between the coils. The RF coil for receiving the NMR signal should be placed as close to the ROI as possible for the high sensitivity. The exact shape of the coil should fit the object from which the NMR signal is taken. The susceptibility of material of the coil should match the susceptibility of the load in the ROI. If the

susceptibility of the material of the coil element is different from the load, it will interfere with the NMR signal. Because of this effect, the components of a coil, e.g. capacitors and diodes, should be located away from the tissue, shielded with nonelectric material or made of a neutral susceptibility material. All the factors that influence the coil must be evaluated with the load in place to have reliable results.

To optimize coils for MRI systems, many techniques are used. Decreasing the losses can improve the Q of a coil. The ohmic loss can be addressed by maximizing the cross section of the conductor as far as possible, using the best available material, and choosing high quality discrete components. For mid to high frequencies the noise picked up from the sample and the radiated loss are dominant and the loss by the resistance of the coil is normally negligible. The dielectric loss of electric field can be reduced by using a balanced matching coil (Murphy-Boesch, Koretsky, 1983), reducing the effective inductance of the coil (Chen, Hoult, 1989), and by using Faraday shields (Gadian, Robinson, 1979). It is well known that distributed capacitance effectively makes the current more uniform. The standard for RF coils is to have no more than a distance of approximately $\lambda / 20$ (λ is the wavelength) between the capacitors (Chen, Hoult, 1989). Distribution of capacitance around the loop also reduces the maximum voltage present around the loop. This in turn reduces dielectric loss and the shift of the coil resonance frequency upon introduction of the sample or due to the movements of the animal during experiment (Decorps et al., 1985). An unbalanced coil produces a local electric field higher than necessary. Such a high electric field causes more power loss in the sample and produces substantial radiation locally. The use of a balanced matching circuit may solve this problem (Murphy-Boesch, Koretsky, 1983). The coil-to-ground dielectric

losses due to the coil-to-ground lumped capacitor is approximately halved by the use of a balanced circuit instead of an unbalanced one (Murphy-Boesch, Koretsky, 1983). A distributed circuit model indicates that the efficiency of the balance circuit is even greater, a quarter of that of the unbalanced one, than that obtained with the lumped circuit (Murphy-Boesch, Koretsky, 1983). However, if the sample is not situated symmetrically within an NMR coil, the advantages of a coil balanced with respect to the ground are reduced. The inductive loss of magnetic field remains if a coil couples to the sample. The ideal would be to have the magnetic field only in the ROI. The radiative loss also can be moderated by use of geometries that have lower radiation resistances, for example quadrupoles. A quadrature detection coil system provides $\sqrt{2}$ gain in SNR over a linear coil (Chen et al., 1983). The use of separate transmitter and receiver surface coils with decoupling can combine the high sensitivity of the small coil for reception and the homogeneity of large coils for transmission and optimization of the SNR.

The improvement of an RF receiving coil is a major factor in optimization of an RF coil design in NMR. Both the characteristics of the coil and its electric and magnetic field interactions with the sample determine the performance of a coil. A fundamental problem in NMR is how best to image an ROI at a distance from the surface of a specimen. Often, it is desirable to limit the field of view (FOV) so as to avoid extraneous noise and all unwanted signals from neighboring regions. Surface coils have the potential for improving the SNR, particularly for anatomical regions near the body surface (Ackerman et al., 1980). Qualitatively speaking, surface coils can have two sources of advantage in terms of the SNR. First, by being closer to the ROI, they can detect a stronger signal. Secondly by being physically smaller than conventional receiver coils,

they will receive less of the sample-generated thermal noise. Implanted coils were proven to have even better SNR than surface coil when the ROI is the internal structure. SNR advantage of surgically implanted, inductively coupled coils over surface coils was shown from the following (Arnder et al., 1996)

$$\frac{\text{SNR}_i}{\text{SNR}_s} \equiv \left[\frac{(b_s^2 + D^2)^3}{2^3 b_s b_i^5} \frac{R_s}{R_i} \right]^{1/2} \quad [1-33]$$

where SNR_i is the SNR for the implanted coil, SNR_s is the SNR for the surface coil, b_s is the radius of the external surface coil, b_i is the radius of the implanted coil, D is the separation between the implanted and the external surface coil, R_s and R_i are the isolated resistances of the surface coil and the implanted coil. The SNR advantage of surgically implanted, inductively coupled coils over surface coils depends only on the geometry, i.e., the respective coil radii and the depth of the ROI. There is no real dependence of implanted coil SNR on pick-up coil (the coil used to couple with the implanted coil and pick up the NMR signal received by the implanted coil) size over the range used. But as the pick-up coil becomes very small or very large, this will break down. It can be seen that the deeper a coil is implanted, the higher SNR will an implanted coil gain over a surface coil. The currents in the ground loops and the associated resistive and radioactive losses (Hoult, Richards, 1976), and the shifts of the resonance frequency of the coil due to the movements of the patient or the animal under study modulate the free induction signal and contribute to the noise. An implanted coil inductively coupled to a transmit-receive coil is a nearly perfectly balanced coil with respect to the sample (Murphy-Boesch, 1985). Thus it reduces the electric losses in the sample and also the radioactive and resistive losses in the ground loops and the frequency shift of the coil

resonance frequency upon introduction of the sample or due to the movements of the animal under study.

Magnetic Field and Homogeneity

We are interested in both the circular coil and the half saddle shape coil. The magnetic field of the coils (with uniform currents and in low complex permeability environment) in the near field region (the distance from the region to the coils is much smaller than the coil size) can be calculated by the Biot-Savart law.

For a single-turn flat circular coil oriented as in Figure 2-1, the magnetic field generated at any point, q, in the near field region, resulting from a unit current flowing in the coil is (Smythe, 1968),

$$B_p = \frac{\mu}{2\pi} \frac{y}{p[(a+p)^2 + y^2]^{1/2}} \left[-K + \frac{a^2 + p^2 + y^2}{(a-p)^2 + y^2} E \right], \quad [2-1]$$

$$B_y = \frac{\mu}{2\pi} \frac{y}{p[(a+p)^2 + y^2]^{1/2}} \left[K + \frac{a^2 - p^2 - y^2}{(a-p)^2 + y^2} E \right]. \quad [2-2]$$

where B_y and B_p are axial (y) and radial (p) component of the field at point q; a is the coil radius; μ is the permeability of the medium in the region of the coil;

$K = \int_0^{\pi/2} \frac{d\Psi}{\sqrt{1 - k^2 \sin^2 \Psi}} = F(\frac{\pi}{2}, k)$, where F is the complete elliptic integrals of first kind; and $E = \int_0^{\pi/2} \sqrt{1 - k^2 \sin^2 \Psi} \cdot d\Psi = E(\frac{\pi}{2}, k)$, the complete elliptic integrals of second kind.

From Figure 2-1, we can see that the magnetic field $(B_1)_{xy}$ generated at any given point q is given by

$$|(B_1)_{xy}| = \sqrt{B_y^2 + (B_\rho \sin \theta)^2}, \quad [2-3]$$

where θ is the angle between the direction of B_ρ and B_0 .

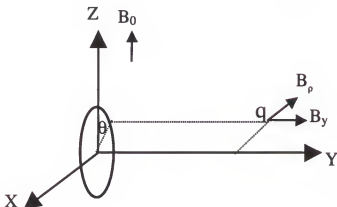


Figure 2-1. Coordination in a single-turn flat circular coil.

For a half-saddle shaped coil oriented as in Figure 2-2, at any point (x, y, z) in the y-z plane, the magnetic field generated by a coil with one unit current is (see appendix for the detail of the calculation)

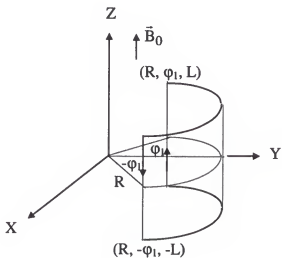


Figure 2-2. Coordination in a half-saddle coil

$$B_z = 0$$

$$B_x = 2L \left\{ \frac{\frac{(y - R \cos \varphi_1)}{[(x - R \sin \varphi_1)^2 + (y - R \cos \varphi_1)^2] \sqrt{(x - R \sin \varphi_1)^2 + (y - R \cos \varphi_1)^2 + L^2}}}{\frac{(y - R \cos \varphi_1)}{[(x + R \sin \varphi_1)^2 + (y - R \cos \varphi_1)^2] \sqrt{(x + R \sin \varphi_1)^2 + (y - R \cos \varphi_1)^2 + L^2}}} \right\} \\ + \frac{2LR}{\sqrt{A+P}} \left\{ 2 \cos \alpha \frac{1}{k^2 \Delta} + \sin \alpha \left[\frac{1}{k^2} \left(1 - \frac{2}{k^2} \right) E(\psi, k) - \frac{1}{k^2} (2 + k^2) \frac{\sin \psi \cos \psi}{\Delta} + \frac{2}{k^2} F(\psi, k) \right] \right\} \frac{\frac{\varphi_1 - \alpha}{2}}{\frac{-\varphi_1 - \alpha}{2}} \quad [2-4]$$

$$B_y = 2L \left\{ \frac{\frac{(x - R \cos \varphi_1)}{[(x - R \sin \varphi_1)^2 + (y - R \cos \varphi_1)^2] \sqrt{(x - R \sin \varphi_1)^2 + (y - R \cos \varphi_1)^2 + L^2}}}{\frac{(x + R \cos \varphi_1)}{[(x + R \sin \varphi_1)^2 + (y - R \cos \varphi_1)^2] \sqrt{(x + R \sin \varphi_1)^2 + (y - R \cos \varphi_1)^2 + L^2}}} \right\} \\ + \frac{2LR}{\sqrt{A+P}} \left\{ \cos \alpha \left[\frac{1}{k^2} \left(1 - \frac{2}{k^2} \right) E(\psi, k) - \frac{1}{k^2} (2 + k^2) \frac{\sin \psi \cos \psi}{\Delta} + \frac{2}{k^2} F(\psi, k) \right] - \frac{2 \sin \alpha}{k^2 \Delta} \right\} \frac{\frac{\varphi_1 - \alpha}{2}}{\frac{-\varphi_1 - \alpha}{2}} \quad [2-5]$$

where

$$A = x^2 + y^2 + L^2 + R^2; \tan \alpha = x/y; \psi = \frac{\varphi - \alpha}{2}; P = 2R \sqrt{x^2 + y^2} \geq 0; \\ k = \frac{2P}{A+P}; \Delta = \sqrt{1 - k^2 \sin^2 \psi}; k' = \sqrt{1 - k^2};$$

$$F(\Psi, k) = \int_0^\Psi \frac{d\Psi}{\sqrt{1 - k^2 \sin^2 \Psi}}; E(\Psi, k) = \int_0^\Psi \sqrt{1 - k^2 \sin^2 \Psi} \cdot d\Psi \quad (\text{See the appendix for the details of the calculation}).$$

From Equations [2-4] and Eq. [2-5], we can see that the magnetic field $(B_1)_{xy}$ generated at any given point (x, y, z) is given by

$$|(B_1)_{xy}| = \sqrt{B_x^2 + B_y^2}. \quad [2-6]$$

Equations [2-3] and [2-6] can be used to calculate the magnetic field at any given point in the x-y plane for a half-saddle coil, and at any given point for a circular coil with different sizes. From the magnetic field we can determine the optimal size for each kind of coil to provide a homogeneous field within the ROI.

Impedance Matching

After the voltages are induced in the receiving coil, the problem is how to get them from within the confines of the magnet into the receiver of the instrument without introducing extra noise. A wire carrying the NMR signal out of the magnet can radiate and act as an antenna. In order to prevent this from occurring, a shielded RF transmission cable of the coaxial variety is used.

Referring to Figure 2-3, the input impedance of the transmission line with characteristic impedance Z_0 at distance d is (Gonzalez, 1997)

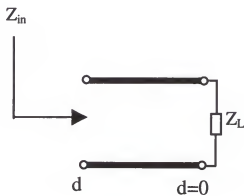


Figure 2-3. Transmissions line with a load of impedance Z_L .

$$Z_{IN}(d) = Z_0 \frac{(Z_L + jZ_0 \tan \beta d)}{(Z_0 + jZ_L \tan \beta d)}, \quad [2-7]$$

and the reflection coefficient is

$$\Gamma_{IN}(d) = \Gamma_0 e^{-j2\beta d}, \quad [2-8]$$

where $\beta = 2\pi / \lambda$, d is the length of the cable and Γ_0 is the load reflection coefficient

$$\Gamma_0 = \frac{Z_L - Z_0}{Z_L + Z_0}. \quad [2-9]$$

Equation [2-9] shows that $\Gamma_0=0$ when $Z_L = Z_0$. That is, there is no reflection from the load when $Z_L = Z_0$. A line with $Z_L = Z_0$ is called a properly terminated or matched transmission line. From Eq. [2-7] it can be seen that a very important property of a transmission line is its ability to change load impedance to another value of impedance at its input. For a half wavelength matched transmission line, $Z_{IN}(\lambda/2) = Z_L$ and $\Gamma_{IN}(\lambda/2) = \Gamma_0$. So the input impedance of a half wavelength matched transmission line is the same as without the transmission and there is no reflection. So we can use a matched half wavelength transmission line for our coil to keep the load impedance unchanged. If, at the end of a transmission line, there is only a termination of load impedance, i.e., $Z = Z_L$, dissipated power in the impedance Z will be maximum, $|V|^2 / 4 \operatorname{Re}(Z)$. If Z differs from the value Z_L , then power will not be maximally transferred to the load. It is conventional to transform RF coils for MRI to have 50Ω nominal impedance. It is more likely to have impedance not equal to 50Ω . This impedance must be transformed to 50Ω resistance in order to employ the coaxial cable optimally. Many possible matching schemes, capacitive, inductive, and mutually inductive have been talked about in the literature (Chen, Hoult, 1989). The precise method is not substantially important, but there are several considerations that are relevant. First, the matching scheme is assumed to be lossless since the reactive element

is the only one allowed in the matching network. Second, it is important that balanced matching techniques are used (Murphy-Boesch, Koretsky, 1983). Any lack of balance reduces the effectiveness of the circuit.

The primary concern for the coils is SNR. It is assumed that the preamplifier has an optimum noise figure when the source impedance is 50Ω that is often used on modern MRI systems. The impedance mismatch does not reduce the SNR even though it reduces the power delivered to the preamplifier. The circuits discussed below all can be used for matching by carefully selecting components (Peterson et al., 1997).

Figure 2-4 shows the circuit diagram for a conventional matching technique. For this case $V_a = V(1+jX_m/R)$ and $V_b = 0$, which is unbalanced around the center line of the coil. In Figure 2-5, $V_a = V(1-jX_m/2R)$ and $V_b = V(1+jX_m/2R)$. The potential difference is the same, but some of the voltage now is antisymmetric around the center line of the coil, so there still remains a voltage V , which is unbalanced. Figure 2-6 (b) shows a balun (an balanced electrical circuit shown in Figure 2-6 (a)) used for matching (Chen, Hoult, 1989), where $V_a = V(1/2-jX_m/2R)$ and $V_b = V(1/2+jX_m/2R)$. These results are the same as above, except the unbalanced voltage has become both symmetric and half as large in amplitude. The circuit shown in Figure 2-7 was developed to produce an entirely balanced voltage (Peterson et al., 1997), where

$$V_a = -V_b = \left(\frac{x}{y} + j\frac{2x^2}{yR}\right)V \quad [2-10]$$

$$Z = \frac{y^2 R}{4a^2}. \quad [2-11]$$

This is a balanced circuit and is good for balanced matching.

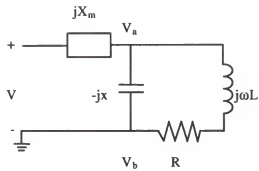


Figure 2-4. A conventional matching circuit.

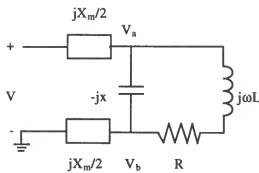
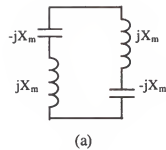
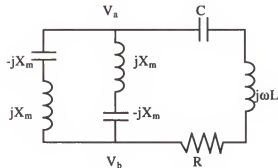


Figure 2-5. A conventional balanced matching circuit.



(a)



(b)

Figure 2-6. Balun matching circuit. (a) A balun; (b) A balun used in a matching circuit.

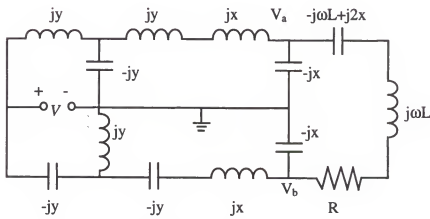


Figure 2-7. A balanced matching circuit

Coupling

When a coil is placed near another coil to detect the NMR signal induced in that coil, flux lines produced by current in this coil link it to the other coil, and the two coils are said to be inductively coupled. The effect that this coupling produces can be expressed in terms of a property called the mutual inductance, M . The circuit diagram of this coil system is shown below

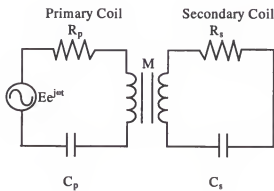


Figure 2-8. Schematic diagram of an inductively coupled coil system.

Here, we have replaced the actual EMF, $E \cos \omega t$, by a complex quantity $E e^{j\omega t}$ to make the calculation simpler.

From the circuit diagram in Figure 2-8 we obtain the following equations

$$R_p i_p + L_p \frac{di_p}{dt} + \frac{\int i_p dt}{C_p} - M \frac{di_s}{dt} = E e^{j\omega t} \quad [2-12]$$

$$R_s i_s + L_s \frac{di_s}{dt} + \frac{\int i_s dt}{C_s} - M \frac{di_p}{dt} = 0 \quad [2-13]$$

If we let $i_p = I_p e^{j\omega t}$ and $i_s = I_s e^{j\omega t}$, and substitute them into Eq. [2-12] and Eq. [2-13], we obtain

$$I_p = \frac{E}{Z_p} \quad [2-14]$$

$$I_s = \frac{j\omega ME}{Z_p Z_s} \quad [2-15]$$

where $Z_p = \sqrt{R_p^2 + X_p^2}$; $Z_s = \sqrt{R_s^2 + X_s^2}$; $X_p = L_p \omega - \frac{1}{C_p \omega}$; $X_s = L_s \omega - \frac{1}{C_s \omega}$; $Z_p' = \sqrt{R_p^2 + X_p^2}$;

$$R_p' = R_p + \frac{M^2 \omega^2}{Z_p^2} R_s \text{ and } X_p' = X_p - \frac{M^2 \omega^2}{Z_p^2} X_s$$

We can then obtain

$$\left| \frac{I_p}{I_s} \right| = \frac{|Z_s|}{\omega M} = [(1 - \omega_s^2 / \omega^2)^2 + 1/Q_s^2]^{1/2} / K \quad [2-16]$$

where $\omega_s = \frac{1}{\sqrt{L_s C_s}}$, $Q_s = \frac{\omega L_s}{R_s}$, $K = k(L_p / L_s)^{1/2}$ and $k = M / (L_s L_p)^{1/2}$, where k is

called the coupling constant. In the case where the secondary coil is just a loop, the above analysis will be simplified

$$I_p / I_s = [1 + 1/Q_s^2] / K \quad [2-17]$$

For a coil whose Q_s is about 100, $I_p / I_s = 1 / K = \frac{1}{k(L_p / L_s)^{1/2}}$. It is seen that the

stronger the coupling and the larger the ratio of primary inductance to the secondary inductance, the closer the secondary current is to the primary current.

Generally the efficiency, ϵ , for transfer of power to the secondary coil is defined as

$$\epsilon = \frac{P_s}{P_p + P_s} = \frac{1}{1 + \frac{P_p}{P_s}} \quad [2-18]$$

Here we go back to our original current equations, Eqs. [2-14] and [2-15], then we have

$$\frac{P_s}{P_p} = \frac{M^2 \omega^2 R_s}{Z_s^2 R_p}. \quad [2-19]$$

It is seen that, for a fixed value of M , ω , R_s , R_p , this ratio is maximum when $X_s=0$, that is

$$\left(\frac{P_s}{P_p}\right)_{\max} = \frac{M^2 \omega^2}{R_s R_p}. \quad [2-20]$$

So

$$\epsilon_{\max} = \frac{M^2 \omega^2}{M^2 \omega^2 + R_s R_p} \quad [2-21]$$

and

$$|I_s| = \frac{M \omega E}{R_s \sqrt{\left(R_p + \frac{M^2 \omega^2}{R_s}\right)^2 + X_p^2}} \quad [2-22]$$

To make $|I_s|$ a maximum, we require X_s to be zero. So we then have

$$\omega = \omega_p = \frac{1}{\sqrt{L_p C_p}} = \omega_s = \frac{1}{\sqrt{L_s C_s}} = \omega_0 \quad [2-23]$$

and

$$I_s(\epsilon_{\max}) = \frac{M \omega E}{R_p R_s + M^2 \omega^2}. \quad [2-24]$$

For the efficiency approaches unity, it is required that $M^2 \omega_0^2 \gg R_s R_p$, then the current, I_s , approaches zero.

For given values of certain constants (power source, mutual-inductance, self-inductance and capacitance) of a coupled system, two different adjustments, one of the primary reactance and the other of the secondary reactance, give a maximum amplitude for the secondary current. This is attained by setting

$$\left. \frac{\partial I_s}{\partial X_p} \right|_{X_s \text{ when } \frac{\partial I_s}{\partial X_s} = 0} = 0. \quad [2-25]$$

That is, solve X_s by setting the first derivative of I_s with respect to X_s to zero, substitute X_s into I_s , and then solve X_p by setting the first derivative of I_s with respect to X_p to zero. From this we find

$$X_s = \frac{M^2 \omega^2}{Z_p^2} = X_p, \quad [2-26]$$

and

$$X_p(R_s - M^2 \omega^2 R_p / Z_p^2) = 0. \quad [2-27]$$

$$R_p R_s$$

We know consider this equation in these different regimes of $M^2 \omega^2$ with respect to $R_p R_s$.

$$(a) \text{ In the case where } M^2 \omega^2 < R_p R_s, \quad [2-28]$$

i.e.,

$$k < \frac{1}{\sqrt{Q_p Q_s}}, \quad [2-29]$$

then $X_p = 0$, and $X_s = 0$, i.e.,

$$\omega = \omega_p = \frac{1}{\sqrt{L_p C_p}} = \omega_s = \frac{1}{\sqrt{L_s C_s}} = \omega_0 \quad [2-30]$$

are the conditions for the largest attainable amplitude of secondary current. The coupling of this system is called deficient coupling or under coupling (Pierce, 1920; Terman, 1955). The secondary current obtained under these conditions is

$$I_{s\max} = \frac{M\omega E}{R_p R_s + M^2 \omega^2}. \quad [2-31]$$

The current is seen to increase with increasing M when the circuit is under coupling. If we differentiate Eq. [2-31] with respect to M , and we obtain a negative quantity for all values of $M^2 \omega^2$ less than $R_p R_s$.

(b) In the case where $M^2 \omega^2 > R_p R_s$, [2-32]

i.e.,

$$k > \frac{1}{\sqrt{Q_p Q_s}} \quad (Q_p = \frac{\omega L_p}{R_p}), \quad [2-33]$$

then

$$\frac{X_s}{X_p} = \frac{R_s}{R_p} = \frac{M^2 \omega^2}{Z_p^2} \quad [2-34]$$

are the conditions for the largest attainable amplitude of secondary current, and the coupling of the system is called sufficient coupling or over coupling. The current induced in the secondary coil

$$i_{s\max} = \frac{E \cos(\omega t + \pi/2 - \tan^{-1} \frac{X_p}{R_p})}{2\sqrt{R_p R_s}}, \quad [2-35]$$

$$I_{s\max} = \frac{E}{2\sqrt{R_p R_s}}; \quad [2-36]$$

and the current in the primary coil

$$i_{p\max} = \frac{E \cos \omega t}{2R_p}, \quad [2-37]$$

$$I_{p\max} = \frac{E}{2R_p}. \quad [2-38]$$

So we can see that at sufficient coupling if $R_p = R_s$, then the current induced in the secondary coil is the same as that in the primary coil; however, when $X_p=0$ there is 90° phase difference. The average power supplied to the primary coil is

$$\overline{P_{pt}} = EI_p = E^2 / 2R_p \quad [2-39]$$

and the power converted into heat or radiated as electric waves from the primary coil

$$\overline{P_p} = i^2 R_p = E^2 / 4R_p. \quad [2-40]$$

The difference between the input power and the converted power in the primary coil is the power communicated to the secondary coil,

$$\overline{P_{ps}} = E^2 / 4R_p, \quad [2-41]$$

which is one-half of the input power.

The frequencies in the coils are (Terman, 1955)

$$\omega = \frac{\omega_0}{\sqrt{1 \pm k[1 - \frac{1}{2k^2}(\frac{1}{Q_p^2} + \frac{1}{Q_s^2})]}}, \quad [2-42]$$

It is seen that in the case of over coupling the value of secondary current obtained is independent of the mutual inductance.

(c) In the case where

$$M^2\omega^2 = R_p R_s, \quad [2-43]$$

i.e.,

$$k = \frac{1}{\sqrt{Q_p Q_s}}, \quad [2-44]$$

then $X_p = 0$, and $X_s = 0$, i.e.

$$\omega = \omega_p = \frac{1}{\sqrt{L_p C_p}} = \omega_s = \frac{1}{\sqrt{L_s C_s}} = \omega_0 \quad [2-45]$$

are the conditions for the largest attainable amplitude of secondary current. The coupling of the system is called critical coupling. The secondary current obtained under this condition is

$$I_{s_{\max}} = \frac{M\omega E}{R_p R_s + M^2 \omega^2} = \frac{E}{2\sqrt{R_p R_s}}. \quad [2-46]$$

It is seen that the critical coupling is the point where the value of secondary current obtained is independent of the mutual inductance.

For an inductively coupled implanted coil system during reception of the NMR signal, the primary coil is the implanted coil and the secondary coil is the external coil. The signal and noise are inductively coupled to the external coil, as shown in Figure 2-9. The output voltage of the signal from the external can be written as (personal communication with Dr. G.R. Duensing, Electrical and Computer Engineering Department, University of Florida)

$$V_O = \alpha V_{IS} + \beta V_{IN} + \gamma V_{EN}, \quad [2-47]$$

where α, β are fractions of signal voltage and noise from a implanted coil over the total output voltage and γ is the factor noise from an external coil over the total output voltage.

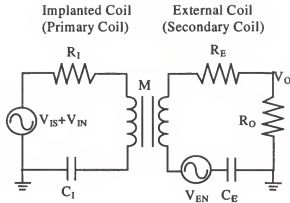


Figure 2-9. Schematic diagram for the signal-to-noise ratio simulation of an inductively coupled coil system.

Then the SNR can be written as

$$\text{SNR} = \frac{\alpha V_{IS}}{\beta V_{IN} + \gamma V_{EN}}. \quad [2-48]$$

When at resonance ($\omega L - \frac{1}{\omega C} = 0$), and thus

$$V_{IN} + V_{IS} = i_I R_I - i_E j \omega M, \quad [2-49]$$

$$V_{EN} = i_E (R_O + R_E) - i_I j \omega M. \quad [2-50]$$

So

$$V_O = R_O i_E = R_O \left[\frac{V_{EN} + \frac{j \omega M}{R_I} (V_{IS} + V_{IN})}{(R_O + R_E + \frac{\omega^2 M^2}{R_I})} \right] = \xi V_{EN} + j \omega M \frac{\xi}{R_I} V_{IS} + j \omega M \frac{\xi}{R_I} V_{IN} \quad [2-51]$$

$$\text{where } \xi = \frac{R_O}{R_O + R_C + \frac{\omega M^2}{R_I}}.$$

Thus

$$|\text{SNR}|^2 = \frac{\frac{\omega^2 M^2}{R_I^2} \xi^2 \langle v_{IS}^2 \rangle}{\xi^2 \langle v_{EN}^2 \rangle + \xi^2 \frac{\omega^2 M^2}{R_I^2} \langle v_{IN}^2 \rangle} = \frac{\frac{\omega^2 M^2}{R_I^2} \langle v_{IS}^2 \rangle}{\langle v_{EN}^2 \rangle + \frac{\omega^2 M^2}{R_I^2} \langle v_{IN}^2 \rangle} \quad [2-52]$$

Since $\langle v_{EN}^2 \rangle = R_E; \langle v_{IN}^2 \rangle = R_I$ and at critical coupling $\omega^2 M^2 = R_E R_I$,

$\frac{\omega^2 M^2}{R_I^2} \langle v_{IN}^2 \rangle = \langle v_{EN}^2 \rangle$, i.e., the noise contributed from the implanted coil and from the external coil are the same. When the coupling is sufficient, the noise from the external coil dominates and when the coupling is deficient the noise from the external coil dominates. It can also be seen that the stronger the coupling the higher the SNR is.

Decoupling

For high sensitivity, a small single surface coil is used in NMR experiments. When a single surface coil is used as both transmitter and receiver, the RF excitation field is not uniform. This nonuniform excitation makes it impossible to produce accurate flip angles over the entire ROI. This problem can be overcome if a large area surface coil is used for the excitation and a small surface coil used for reception of the signal from the ROI. In this method the larger coil can produce a uniform excitation over large portion of the sample and the small coil can receive the signal with high sensitivity.

The separation of transmitting and receiving coils introduces other problems, due to the interactions between them. During the transmission, the current induced in the receiving coil produces a B_1 field. Since the receiving coil is resonant, the EMF is

$$\epsilon = \frac{\partial \Phi}{\partial t} = \omega B_1 A, \quad [2-53]$$

where A is the area enclosed by the receiving coil loop, however, the resistance R_s is very small, so the current induced by the transmitting coil,

$$I_s = \frac{\epsilon}{R_s} = \frac{\omega B_1 A}{R_s}, \quad [2-54]$$

can be very high. The receiving surface coil effectively concentrates the applied field of the transmitting coil. The RF excitation field in affecting the adjacent sample has the spatial variation characteristic of the receiving coil and not the larger transmitting coil, therefore the advantage of using a large transmitting coil is lost. The power ratings from the transmitting coil might be as high as 15 kW and part of this energy could be coupled to the receiver coil. The capacitor in the small receiving coil can burn out and the sample can be overheated. A method for decoupling the transmitting coil from the receiving coil is required to protect the sample against possible RF heating, the capacitor from burning, and provide uniform B_1 field.

During the reception of the NMR signal, noise currents flowing in the transmitting coil induce noise currents in the receiving coil by the way of the mutual inductance M between the coils. Extra noise will appear in the image, which therefore degrades SNR. The presence of the resonant transmitting coil also tends to degrade the field of the receiving coil.

One way to alleviate these problems is to place the two coils so that the RF magnetic fields are physically and electrically orthogonal (Crowley et al., 1985). However, to reduce interactions to a tolerable level by this method, it is necessary to position the coil with a high degree of accuracy. The subject must then be maneuvered into a position in order to conform to this arrangement. It is often difficult to do this with animals or patients. Another way is to decouple the two coils which allows the placement

of the transmitting and receiving coils at an arbitrary relative orientation. An ideal decoupling scheme would open the receiving coil in the transmitting mode and the transmitting coil in the receiving mode. A lossy or reactive "switch" may degrade the SNR, shift the frequency and/or distort the magnetic field profile of either the receiving or transmitting coil (Edelstein et al., 1986). A number of schemes have been published, including magnetic reed relay (Bendall et al., 1984), passive decoupling using cross diodes (Bendall et al., 1986), active decoupling using PIN diodes in a resonant blocking circuit (Edelstein et al., 1986), and a "counterrotating current pair" (Froncisz et al., 1986) or "antisense coil" (Chen, 1992). As pointed out in a recent study (Chen, 1992), most of these schemes are far from ideal, the degradation of SNR probably being the most serious drawback. However, in human or animal studies, the noise arising from the sample itself generally dominates, rendering the decoupling circuit less sensitive to imperfections. This is not the case when small surface coils are used. Compared with a single-coil circuit, the "antisense coil" method introduced significant SNR losses when employed with unloaded coils. Any increase in the length of connection would lead to the loss of sensitivity (Prichard et al., 1983). On the other hand, the combination of susceptibility problems and high sensitivity requirement precludes components, such as capacitors, from being placed in the immediate vicinity of the coil. A quarter wave line in series with the surface coil (Haase et al., 1984) effectively blocks currents in the surface coil during transmission, but the quarter wave line becomes part of the coil during reception. This can adversely affect the Q and hence SNR. Another approach is to use a resonant blocking circuit, which is a highly effective decoupling scheme.

Among the schemes used for decoupling only the crossed diode method and the resonant blocking circuit method are appropriate for the small implanted coils because of the physical limitation. We will show that the resonant blocking circuit scheme is a more effective decoupling scheme than the crossed diode scheme.

The crossed diode decoupling scheme is shown in Figure 3-7. When it is transmitting, the current induced in the receiving coil is large. This activates the diodes and the receiving coil becomes a closed, conducting loop. The current I_R induced in the receiving surface coil can be obtained from Equation [2-53]

$$I_R = \frac{\omega B_1 A}{X_R} = \frac{B_1 A}{L}. \quad [2-55]$$

The current induced is small compared to the case without decoupling. This is because the impedance ωL is generally much larger than the real impedance of the receiving coil.

A resonant blocking circuit in parallel with a receiving coil is shown in Figure 3-3. The diodes conduct during transmission when a large RF signal is present, but they are open during the reception when the current is small. This is accomplished by placing a series combination of an inductor (L_1) and crossed PIN diodes D_1 and D_2 in parallel with the capacitor (C_2) on the receiving coil. The value of the inductor is chosen such that the loop resonates at 200 MHz for 1H (the Larmor frequency for 1H at 4.7 Tesla) or 81 MHz for ^{31}P (the Larmor frequency for ^{31}P at 4.7 Tesla), where the loop consists of the inductor, the capacitor (C_2) and the crossed diodes. For the transmitting only surface coil and the receiving only coil system, crossed diodes in series with the transmitting coil are also provided. During transmission, a strong current flows in the transmitting coil. The receiving coil resonant blocking circuit, which activates the diodes in the transmitting coil and the diodes in the resonant circuit L_1-C_2 , L_1-C_2 , then has a high impedance. This keeps

significant current from flowing in the receiving coil. The current in this case is much smaller than that in the crossed diode scheme. Thus, the RF excitation gets through to the sample essentially unaffected.

The B_1 field is unaffected by the currents in the receiving coil if the impedance of the receiver blocking circuit is substantially greater than the impedance of a closed loop of a receiving surface coil (Edelstein et al., 1986), i.e.,

$$\frac{Q}{\omega C_2} \gg \omega L = \frac{N}{\omega C_2}, \quad [2-56]$$

where Q is the quality factor of the blocking circuit, L is the loop inductance, and N is the number of divided capacitors in the receiving surface coil. This condition is not difficult to achieve. For example, if you have six capacitors, Eq. [2-56] says that the Q must be substantially greater than six.

During reception a small current flows in the receiving coil, so the diodes in the resonant blocking circuit and in the transmitting coil are not activated. The impedance of the resonant blocking circuit is small, so all the induced current is in the receiving coil. Since there is no mutual coupling between the transmitting and receiving coils, a very small current flows in the transmitting coil and produces a very small B_1 field. Therefore, no field distortion from the receiving coil and no extra noise appears in the NMR signal from the transmitting coil. Thus the receiving coil is not degraded.

The Pspice (Microsim Cooperation Inc.) simulation results shown in Figure 3-7 and Figure 3-8 also prove that the resonant blocking circuit scheme is a more effective decoupling scheme compared with the cross diodes scheme. It can be seen that without decoupling the current induced in the receiving coil is very large, while with the crossed

diode decoupling, the current is fairly small, and that with the resonant blocking circuit the current is even smaller.

Therefore we provided a resonant blocking circuit in parallel with the receiving coil in our implanted coils. The diodes conducted during the transmitting phase of NMR experiment, when a strong RF signal was present, but were open during the receiving phase when currents were small.

CHAPTER III IMPLANTED ^{31}P RF COILS

Introduction

Phosphorous nuclear magnetic resonance (^{31}P NMR) spectroscopy was first used to observe the phosphorus containing metabolites in intact, excised muscle (Hoult et al., 1974). Since then the method has been used to study a variety of medical problems (Ackerman et al., 1980; Faden et al., 1990; Koretsky et al., 1983; Morikawa et al., 1995; Nicolay et al., 1987; O'Donell et al., 1996; Schnall et al., 1986a; Schnall et al., 1986b; Vink et al., 1989a; Vink et al., 1989b; Schnall et al., 1986b). ^{31}P NMR spectroscopy is a powerful tool for investigation of metabolism *in vivo*. The technique permits measurement of the phosphate energy stored in high-energy phosphates such as adenosine triphosphate (ATP), creatine phosphate (PCr) and inorganic phosphate (Pi). This is done in undisturbed functioning tissue, so the chemical shifts of the PCr and Pi peaks yield a fairly direct estimate of intracellular pH. Due to their noninvasive nature, the measurements can be made repeatedly on the same subject. Also, because they are thought to be free of hazard, they can be used on human subjects. However, there are problems associated with *in vivo* NMR. Spatial selection of specific tissues and adequate SNR are examples. The introduction of the surface coil refined NMR signal localization, since surface coils have a restricted FOV compared to volume coils. Use of surface coils also results in an increase in sensitivity for superficial regions directly beneath the coil

(Ackerman et al., 1980). However, the penetration of the effective B_1 field of a conventional planar surface coil is proportional to its size. Therefore it is required to have surface coils of large diameter for a deep organ such as the spinal cord. For a surface coil of large diameter the FOV is fairly large while the filling-factor is low. It is difficult to localize spectra to a deep organ such as spinal cord without contamination by surrounding tissues like skeletal muscle. The use of special pulse sequences provides improved localization with a large ROI uniformly excited by a large surface coil, but this occurs at the expense of SNR.

Implanted RF coils have a FOV restricted to the actual ROI and the filling factor of the coil is high. The performance advantage of surface coils can be further extended to obtain images and spectra of internal organs (e.g., heart, kidney, spinal cord, liver, carotid artery and skin) via directly driven or inductively coupled implanted coils attached to the structure of interest (Arnder et al., 1994; Farmer et al., 1990; Farmer et al., 1989; Ford et al., 1994; Hollett et al., 1987; Kantor et al., 1984; Murphy-Boesch, 1985; Schnall et al., 1986a; Schnall et al., 1986b; Summers et al., 1995; Wirth et al., 1993; Zhou et al., 1994).

There are problems though with a directly driven implanted coil. First, the coil must be connected to a spectrometer via a wire going through the skin of the animal. This creates a risk for infection. In addition, the wire also contributes extra resistance that may become a dominant source of noise. Second, the coil is small in dimension so the magnetic field is not homogeneous over the ROI. An inductively coupled implanted coil avoids such infection problem and is good for long term observation. However, it also has the problem of magnetic field nonuniformity in the ROI.

We solved all these problems by applying a decoupling scheme to an inductively

coupled implanted coil of small size (4 mm x 5 mm) during the RF transmission. So a larger external coil is used for RF field excitation. In this fashion, we combined an external surface coil with uniform magnetic field for excitation/reception and a small implanted coil with high sensitivity for reception.

Literature Review

Since ^{31}P NMR is an inherently insensitive spectroscopic technique, the localization and sensitivity are of critical importance. High SNR coils are needed to obtain a ^{31}P NMR signal. A flat four-turn surface coil, with mean radius of 0.55 cm, was first applied in ^{31}P NMR to map the metabolism in a whole animal, and it showed an increase in sensitivity (Ackerman et al., 1980). Later, different surface coils were developed to acquire localized spectra from surface structures. The narrow, elongated, crossover surface coil provided shallow B_1 field penetration, thus an intrinsic surface localization (Nicolay et al., 1987). A zigzag coil was introduced to limit B_1 field penetration via inductive interactions between close inductors with opposite directional currents (Nakada et al., 1987). Surface localization strategies require minimizing depth sensitivity while maintaining high coil sensitivity over the extended surface area. The slotted crossover surface coil achieved both objectives (Nagel et al., 1990).

When the ROI, such as a section of a rat spinal cord, is a small volume of tissue, coils with even higher SNR than that of surface coils are required to obtain ^{31}P NMR signal. Implanted RF coils were developed to obtain *in vivo* NMR signals from internal organs without signal loss from intervening tissue. The first chronically implanted coil approach involved connecting a wire through the skin of a rat to the implanted coil. A

two-turn, approximate 1.2 cm diameter, directly driven implanted coil was used to detect the ^{31}P spectra of rat kidneys on a 5.6 Tesla system (Murphy-Boesch, Koretsky, 1983). The connecting wire, extending from the implanted coil through the skin of the animal, increased the risk of infection. To remove the problem of infection, a two-turn, 2 cm diameter implanted coil inductively coupled to an external coil was developed and used to take NMR ^{31}P spectra of a rat internal organs on a 2.1 Tesla system (Schnall et al., 1986a; Schnall et al., 1986b; Schnall et al., 1985). The inductively coupled implanted coil was fine-tuned and impedance-matched remotely by tuning capacitors in the external coil. The inductively coupled implanted coil made chronic high-quality spectroscopy of deep internal structures feasible in a "relatively undisturbed" system.

With the intravenous surface coils or implanted coils, ^{31}P NMR spectroscopy has been applied extensively to study *in vivo* cellular metabolism and has been successfully applied to the study of a number of central nervous system (CNS) insults, including hypoxia (Faden et al., 1989; Vink et al., 1987; Vink et al., 1989a; Vink et al., 1989b; O'Donell et al., 1996; Akino et al., 1997). ^{31}P NMR spectroscopy has been shown to be useful in the characterization of metabolic changes following traumatic brain injury (Vink et al., 1987). *In vivo* ^{31}P NMR was used to measure the effects of the anti-tumor drug adriamycin on the energy metabolism of a rat heart and the exclusive acquisition of NMR signal from cardiac muscle was assured by positioning a solenoid RF coil around the heart (Nicolay et al., 1987). Despite the potential of NMR, few studies of the vertebrate spinal cord have been undertaken with ^{31}P NMR spectroscopy (Faden et al., 1989; Vink et al., 1987; Vink et al., 1989a; Vink et al., 1989b). This can be attributed largely to the relatively small size of the spinal cord, which limits one's ability to acquire

NMR spectra with adequate SNR. Furthermore, signals collected from spinal cord tissue are easily contaminated by signal from nearby tissue. With a small coil placed very close to the ROI, it has been possible to examine the CNS after ischemic or traumatic injury.

^{31}P NMR spectroscopy was first applied to the study of metabolic changes that occurred following experimental lumbar spinal cord trauma in rabbits by using a 1.2 cm x 1.2 cm x 1.2 cm, two-turn saddle surface coil (Vink et al., 1987). The authors reported that losses of high energy phosphates, accompanied by a drop in intracellular pH and free magnesium in the rabbit spinal cord, resulted from weight-drop injury. These studies represented the first *in vivo* analysis of the spinal cord by NMR. These studies were vulnerable to the problems associated with poor spatial localization and sensitivity. Also they used chronic exposure at the spinal cord and the animal did not survive. To help minimize these problems, one could examine larger spinal cords with a combination of higher magnetic field and an implanted coil. An oval-shaped, two-turn, 5 mm x 7 mm implanted coil was used to study swine spinal cords (O'Donell et al., 1996). The RF coil was carefully placed directly on the surface of the spinal cord and NMR data were then acquired by using an adiabatic 90° excitation pulse without any additional spatial localization technique. This was because localizing a voxel of spinal cord tissue would further reduce sensitivity. Despite efforts to retract all muscle from the site adjacent to the surface coil, NMR data consistently showed significant contamination. Further studies should identify a coil with high sensitivity and a localization technique appropriate for the spinal cord. This step is crucial for the measurement of the phosphate metabolite concentrations in spinal cord (i.e., ATP, PCr and Pi).

Since the localization accuracy of a surface coil is not good enough, various NMR pulse sequence techniques for localization, such as DRESS (Bottomley, 1987), STEAM (Frahm et al., 1989), ISIS (Ordidge et al., 1986; Schwartz et al., 1992), DEPTH (Bendall, Pegg, 1985) and integrated OVSISIS (De Graaf et al., 1995) have been used to obtain NMR signals from deep ROIs. These techniques (except for DEPTH) utilize a combination of a frequency-selective RF pulse with a magnetic field gradient to localize the NMR signal. However, signal loss during the localization process is unavoidable. Although some spatial localization methods, such as DEPTH pulse (Bendall, Pegg, 1985) can significantly suppress unwanted signal outside the volume of interest without losing sensitivity, the degree of suppression may not be enough. This is particularly true if the suppressed volume is large, rich in metabolites, and not sufficiently retracted, like when observing muscle, relative to volume of interest (e.g., spinal cord). Since the RF pulses must be both frequency-selective and B_1 -intensive, at present only ISIS can achieve optimal sensitivity in localization experiments conducted with a surface coil. Although ISIS allows for short T_2 , ISIS has some drawbacks. For example, the localization accuracy of ISIS is T_1 weighted. The drawbacks can be alleviated by adding selective excitation followed by gradient dephasing, i.e., outer-volume suppression (OVS). This method of localization is referred to as integrated OVS-ISIS (IOVSSISIS) (De Graaf et al., 1995). IOVSSISIS is also less sensitive to the eddy currents and good for taking localized ^{31}P (having short T_2) spectra.

In the case of small experimental animals, it was difficult to perform noninvasive NMR spectroscopic techniques with localization techniques that combine accurate spatial resolution with satisfactory sensitivity. For example, an *in vivo* 1H spectrum was obtained

after 3072 scans from 13 μl voxel in the T₁₃/L₁ (which is the largest section of the spinal cord) of a rat (Zelaya et al., 1996). The spectrum was acquired with a 64 mm diameter birdcage transmit-only coil and a 17 mm receive-only surface coil on a 4.5 T system with a respiration gating system. It was illustrated that microvolume localized ¹H spectroscopy was achievable only with a respiration gating system.

Most of the experiments using ³¹P NMR spectroscopy with inductively coupled implanted coil have been designed in order to avoid acute surgical effects, but not to follow long term changes. Few successive observations of NMR spectra over long term were reported (Koretsky et al., 1983; Morikawa et al., 1995). The inductively coupled implanted coil had the advantage of permitting repeated NMR observations of a single animal, which was not the case with the NMR experiments that accompany a surgical operation. Inductively coupled implanted coils greatly reduced the risk of infection while providing higher SNR than birdcage or surface coils (Farmer et al., 1989; Murphy-Boesch, 1985; Wirth et al., 1993).

We used an implanted coil placed directly above the spinal cord of a rat. The implanted coil was 4 mm x 5 mm, with a resonant blocking circuit and inductively coupled to an external coil. The implanted coil was decoupled during transmission and a larger external coil was used for uniform excitation. This coil was used to obtain a spectrum from the ROI with high sensitivity. The use of the implanted RF coils also allows long-term *in vivo* studies of phosphorous metabolites after injury and fetal tissue transplantation with optimum sensitivity.

Methods

Simulation

The formula in Eq. [2-3] was used to calculate the magnetic field of the coils operating with a unit current by the software package Mathematica (Wolfram Media, Inc.). The magnetic field of various external coil sizes was simulated to determine the RF homogeneity in the approximate location of the spinal cord relative to the coil used. From the simulated field, the optimal coil dimensions were determined for the transmit-receive external linear surface coil.

Pspice (Microsim Corporation Inc.) was used to simulate the coupling between the ^{31}P implanted coil and the external coil. The schematic diagram of our inductively coupled implanted ^{31}P coil system is shown in Figure 3-1. The frequency and Q of each coil were measured by a HP8725C network analyzer (Hewlett Packard, Inc.). The resistance and the inductance of each coil were calculated from the capacitance, the frequencies and the Q of each coil. We changed the coupling constant in the Pspice program until the two simulated peaks matched the two peaks measured from the network analyzer. This assured that the simulation coupling constant was close to the actual coupling constant between the implanted coil and the external coil. The decoupling efficiencies of the coils using a crossed diode decoupling scheme (its schematic diagram is shown in Figure 3-2) and a resonant blocking circuit scheme (its schematic diagram is shown in Figure 3-3) were also simulated by Pspice, where all parameters in both decoupling schemes were the same.

RF Coil Designs

The sensitivity of an RF coil is directly related to the geometry and the size of the coil. Of the common RF coil geometries (e.g., solenoid, saddle, birdcage and surface coils) used in NMR, solenoid coils have the highest sensitivity (Hoult, Richards, 1976) and are commonly used for NMR spectroscopy. Our initial work involved the optimization of an implantable solenoid coil design for the maximum reception of the ^{31}P NMR signal. This was accomplished by measuring the SNR on a phantom of a 5 mm NMR tube containing a solution of 0.15 M sodium phosphate. We measured the SNR while varying the number of turns in the solenoid (one to four), the gauge of the wire (22, 25 and 28) and the configuration (circular, or elliptic while keeping the cross section area of the implanted coil constant). The external coil was mounted on the inside of a half-cylinder Plexiglas cradle with dimensions of 77.5 cm in length, 4.7 cm outer diameter and 4.1 cm inner diameter. Adjustable capacitors in the external coil provided tuning for the circuit, and an adjustable capacitor in series with the coil provided impedance matching. The cradle was designed to support the rat in a supine position during the experimental procedure, with the implanted receiving coil in position to couple with the external coil. By placing the animals in a supine position, spinal cord motion and the possibility of resulting artifacts, are minimized (Wirth et al., 1993). The final optimized design of the inductively coupled coils was implanted in rats to test for long-term performance and durability.

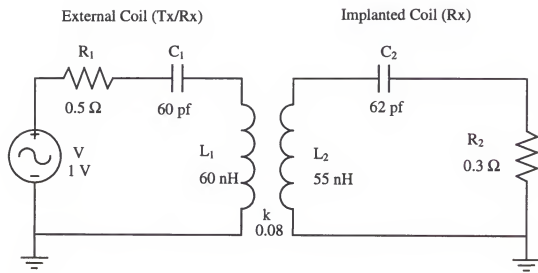


Figure 3-1. Schematic diagram of an inductively coupled ^{31}P implanted coil.

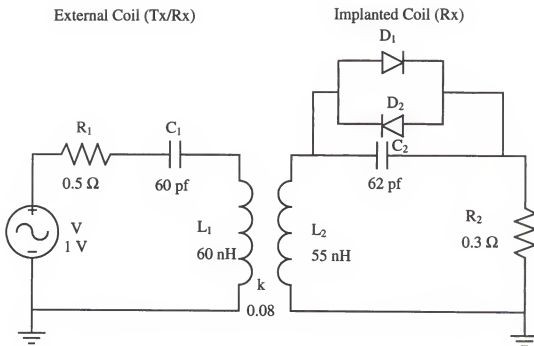


Figure 3-2. Schematic diagram of an inductively coupled ^{31}P implanted coil using crossed diode decoupling scheme.

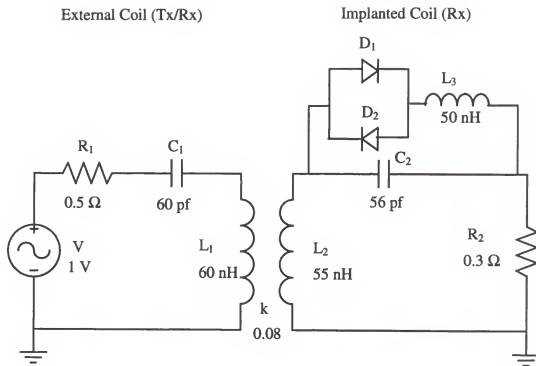


Figure 3-3. Schematic diagram of an inductively coupled ^{31}P implanted coil using resonant block decoupling scheme.

Before proceeding to the implantation of this coil design in rats, we tested the coil on a "rat" phantom. The phantom was made of a 5 mm NMR tube containing a solution of 0.15 M phenylphosphonic acid (phantom spinal cord) embedded in a 4.1 cm diameter half-cylinder. The half-cylinder was made of 0.15 M sodium phosphate and 2% agar gel (phantom rat body). The NMR tube, the "spinal cord" phantom, was positioned so that its center was 7 mm from the center of the surface of the half-cylinder "rat body" phantom, which was the approximate location of the spinal cord in a rat. The use of the different ^{31}P containing chemicals (with different chemical shifts) allowed us to quantitate the amount of signal we receive from the "surrounding tissue" relative to the signal from the "spinal cord". The implanted coil was coated with polymethyl methacrylate (PMMA) to simulate the *in vivo* condition. The implanted coil was positioned directly over the tube. *In vivo*, PMMA was placed over the coil both close to the site of the laminectomy and to secure the coil into position over the spinal cord. PMMA is used clinically to seal craniotomies and has been used regularly by Dr. Doug Anderson's (Professor of Department of Neuroscience, College of Medicine, at University of Florida) research team to close laminectomies in cats. This material produces no ^{31}P NMR signal, sets quickly, and is tolerated well by animals. In addition, the PMMA plug prevented paraspinal muscle from entering the sensitive volume of the RF coil, thus ensuring that most of the observed NMR signal came from the spinal cord. We investigated the possibility that ^{31}P NMR signal might come from the surrounding tissue. We used the "rat" phantom, which allowed us to separately measure the two chemicals (and hence separate spatial regions) of the phantom, for these tests. We investigated the source of

this contamination. We first resected some "tissue" near the implanted coil. Then we moved the phantom 3 mm away from the external coil.

We used IOVSISIS localized NMR technique to overcome the problem of contaminating signal from surrounding tissue. However, to provide good spatial localization, an RF coil is needed to produce a relatively homogeneous field in the ROI. Therefore we designed a relatively large external ^{31}P coil, 3 cm x 3 cm, to provide a good homogeneous field in the region of the spinal cord and the surrounding tissue. Without decoupling the external and the implanted coils during transmission, the small implanted coil would strongly couple to the external coil during transmission and the field would be concentrated into the small implanted coil. The field from the implanted coil would be relatively inhomogeneous in the surrounding tissue. We added a passive decoupling modification to the design of the implanted coil to remove this effect of the implanted coil during transmission, so the external field again was homogeneous. We applied a resonant block circuit (Bendall et al., 1986; Bendall et al., 1984; Bendall, Pegg, 1985; Chen, 1992; Froncisz et al., 1986; Haase, 1984; Picard et al., 1995) for the decoupling between the external surface coil and the implanted coil during the transmission. Our inductively coupled implanted coil with the decoupling circuit combined the homogeneous field from the external surface coil and the high sensitivity and good localization from the small implanted coil. The reason that the decoupling scheme had to be used was also because that the transmitting coil had a very high power rating and part of this energy could be coupled to the small implanted coil. Especially when the adiabatic pulse sequence was used to obtain the localized spectra a lot of heat would be produced in the implanted coil and the chip capacitor could be burned. A method to decouple the

transmitting coil from the receiving coil during transmission was also required for the protection of the rat against possible RF heating and the capacitor from burning.

We compared the performance of the inductively coupled coil design to the case where the coil had a direct connection to the spectrometer. The comparison between the directly driven and the inductively coupled coil was accomplished by measuring SNR in ^{31}P spectra from the "rat" phantom described above.

Since the magnetic susceptibility of the capacitor and the wire are different from the tissue, the components of the coil might cause the magnetic field inhomogeneity, which interferes with the imaging gradient fields and results in local image distortions and spectral broadening. We isolated the problem by imaging each RF coil's element separately while they were immersed in water.

We implanted an inductively coupled ^{31}P RF coil in each of six rats within the spinal columns between T₁₂ and T₁₃ (see Figure 3-4). In order to correlate the metabolic changes observed by ^{31}P NMR spectroscopy with the extent of injury and growth of intraspinal fetal tissue grafts, a ^1H surface coil (4 cm x 4 cm) was mounted over the ^{31}P external coil and on the outer of the rat cradle. First a ^1H surface coil (4 cm x 4 cm) was built as a $^1\text{H}/^{31}\text{P}$ transformer-coupled double tuned coil. Then a quadrature surface ^1H coil (two coils, 10 cm x 4 cm each, making the combined coil 10 cm x 6 cm) was built to eliminated the RF field distortion from the $^1\text{H}/^{31}\text{P}$ transformer-coupled double tuned coil. The ^1H resonance was also used to shim the B_0 field on the water signal and to image the ROI. Although it was critical to restrict the FOV to a small area for ^{31}P NMR spectroscopy of the spinal cord, a large FOV was desired for MRI studies of the anatomical changes that occur after spinal cord injury (SCI) and repair. The dimension of

this coil was determined by the required FOV. Although the SNR for the ^1H surface coil was moderate, but it was adequate for MRI studies because the relatively strong proton signal from water in biological tissue.

Magnetic Resonance Spectroscopy and Imaging

Data for this study were acquired using an imaging spectrometer (Spectroscopy Imaging System VIS 200) with a 4.7 Tesla main magnetic field and 33 cm bore magnet system. The Varian VNMR software program (Varian Associates, Inc.), running on a SPARC10 workstation (Sun Microsystems, Inc.), was used for the data acquisition and processing. For MRI studies, this system was equipped with actively-shield gradient coils (Nalorac Cryogenics Corporation) that produced magnetic field gradients of up to 5 gauss/cm. During all magnetic resonance procedures, animals were anesthetized with 2% halothane and monitored continuously throughout the duration of the experiment for changes in respiratory rate. Animals were placed in the magnet, and an optimization of main magnetic field homogeneity was performed while monitoring the ^1H signal from water.

For ^{31}P studies, the RF circuit was tuned and matched to observe ^{31}P at 81 MHz (4.7 T) by adjusting the capacitors in the external coil. This procedure could be performed while the animal was in the bore of the magnet. Our protocol for obtaining ^{31}P spectra called for the acquisition of 512 scans using a one-pulse acquire sequence or IOVSISIS (De Graaf et al., 1995) localization RF pulse, a 2 s recycle delay, and a 6000 Hz sweep width, which results in a total acquisition time of approximately 20 minutes.

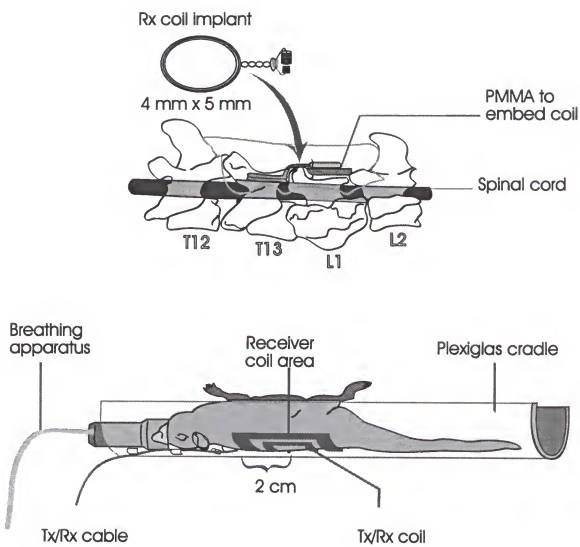


Figure 3-4. Position of the implanted coil.

The ratios of the metabolite status of the tissue, intracellular pH, can be determined according to the equation (Prichard et al., 1983)

$$\text{pH} = 6.77 + \log(\delta P_i - 3.29) / (5.68 - \delta P_i), \quad [3-1]$$

where δP_i was the chemical shift of Pi relative to PCr.

Surgical Procedures and RF coil implantation

Before implantation in the animal, the coil was covered with PMMA. The covering was shaped to provide a smooth and thin surface (1 mm) of PMMA on the side next to the spinal cord. The capacitor and the decoupling components were mounted up away from the spinal cord and oriented so as to keep susceptibility distortion to a minimum.

All animal procedures involved adult male and female Long-Evans hooded rats, and all surgeries were performed under general anesthesia with strict adherence to aseptic procedures. Surgeries were carried out in dedicated surgical rooms. The skin over the vertebral column at the lower thoracic level was incised, the muscle retracted, and three vertebrae exposed. In all animals, the dorsal spinal processes of T₁₃ and L₁ were removed followed by a one level laminectomy at T₁₃. An implantable RF coil was then positioned over the exposed spinal cord and cemented in place with super glue. The paraspinal muscles and skin incision were then sutured closed in layers.

ResultsCoil Optimization

Since it was critical to maximize SNR for the observation of ^{31}P nuclei from the small amount of tissue in the spinal cord, the coil was placed as close to the spinal column as possible without compressing the spinal cord. From the SNR measurements on the phantom, we observed that the SNR of a single turn loop was always lower than that of two- or three-turn coils, but four turn coils did not provide further gain in SNR. Separations consecutive turns by a distance equal to the wire thickness did not improve the SNR. From the measured SNR (shown in Table 3-1) and the constraints from the laminectomy above T₁₃ vertebral level, a three turn (with no separation between turns), 4 mm x 5 mm, elliptic shaped coil made with and 25 AWG wire was determined to be optimal. This coil was placed directly above the spinal cord. A very miniature capacitor, 1.3 mm x 1.3 mm x 1.2 mm, 56 pf (Dielectric Laboratory Inc.), was placed in parallel with the coil to bring the resonant frequency to 81 MHz (the resonant frequency of ^{31}P at 4.7 T). The implanted ^{31}P coil (SNR=144) improved the SNR about three times over the surface coil (SNR=50).

The size of the external coil was optimized to have uniform magnetic field over the ROI and to have strong coupling with the implanted coil. From plots of the magnetic fields of various sizes of coils it was determined that the optimal coil dimension for the ^{31}P transmitting/receiving external coil was 3 cm x 3 cm. The coil gave the optimal mutual coupling, homogeneous field, and high RF field sensitivity. The magnetic field (\mathbf{B}_1)_{xy} on the cross section of the coil at z=0 cm (the coordinate system is shown in Figure

2-2) for the 3 cm x 3 cm ^{31}P external coil is shown in Figure 3-5. It can be seen that across the ROI, 7 mm from the inner center surface of the cradle and 4 mm diameter, (where the spinal cord position when a rat lay in the rat cradle) the variation of the field was less than 10%. The ^{31}P external coil was mounted as close to the implanted coil as possible to have as strong coupling as possible since the stronger the coupling, the greater the SNR (see Eq. [2-52]).

From the Pspice simulation we obtained that the coupling constant between the external coil and the implanted coil in the rat was about 0.08. The current induced in the implanted coil (about 1.0 A) without using any decoupling scheme was close to that in the external coil (about 1.5 A) (see Figure 3-6). In contrast, the current induced in the implanted coil with a crossed diode decoupling scheme was reduced by a factor of 6 (about 0.15 A) (see Figure 3-7). However it was not enough since the magnetic field induced by the implanted coil was comparable with the field from the external surface coil. So a resonant blocking circuit parallel with the capacitor in the implanted coil was used and in this case the current in the implanted coil (see in Figure 3-8) was negligible. The current in the decoupling loop (about 0.15 A) (see Figure 3-8), which was also the current across the capacitor, was about ten times less than that without using any decoupling scheme. So in this case the capacitor was free from burning.

Table 3-1. SNR comparison between different ^{31}P implanted coils and surface coil.

- (a) SNR of a 5 mm diameter circular loop coil with different gauges and number of turns.
- (b) SNR of three turn coil with different gauges and shapes.
- (c) SNR of the surface coil and ^{31}P implanted coil.

Wire Gauge (AWG)	Number of Turns		
	1	2	3
22	110	102	120
28	52	62	109

(a)

Wire Gauge (AWG)	Dimensions	
	$\phi = 5 \text{ mm}$ (circular)	4 mm x 6mm (elliptical)
22	120	104
25	127	144
28	109	135

(b)

Coils	SNR
3 cm x 3 cm surface coil	50
4 mm x 6 mm, 3 turn, elliptic	144

(c)

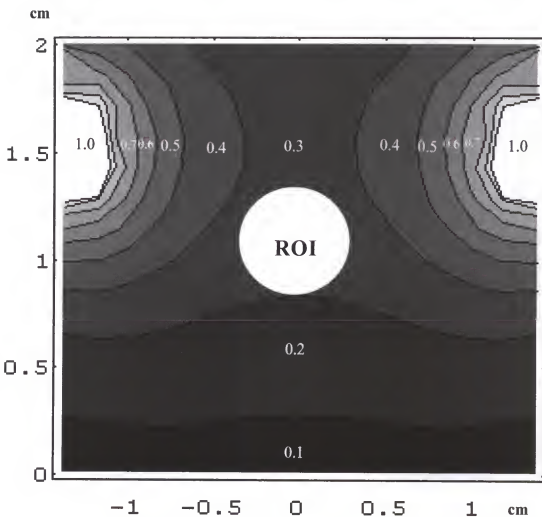


Figure 3-5. B_{xy} at the center cross-section of the $3\text{ cm} \times 3\text{ cm}$ external ^{31}P coil.

The spectra in Figures 3-11 and 3-12 show that the inductively coupled implanted coil (SNR=47) had higher SNR than the directly driven implanted coil (SNR=22, the transmitting power was set to be the same as that for the inductively coupled implanted coil). As the size of the sample is reduced, the noise originating within the sample becomes negligible when compared to the noise of the coil (Hoult and Lauterbur, 1979). Therefore sample loading effects are negligible when using room-temperature small coils to examine biological samples at a field of several Tesla. The resistance (R_{coil}) of the small coil itself is the dominant source of noise ($R_{noise} \sim R_{coil}$). Careful attention was given to maintaining the lead lengths, as the leads contribute additional resistance to R_{coil} (Peck et al., 1995). The inductively coupled implanted coil has a higher SNR than the directly driven implanted coil. This was because the long wire leads connecting the directly driven implanted coil to the spectrometer picked up additional noise and therefore contributed the dominant resistance in the source of noise. Therefore we concentrated our efforts on the inductively coupled implanted coils.

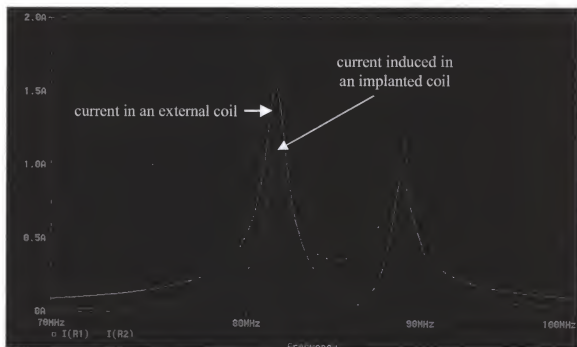


Figure 3-6 Current in an external coil and current induced from the external coil to an implanted coil without using any decoupling scheme.

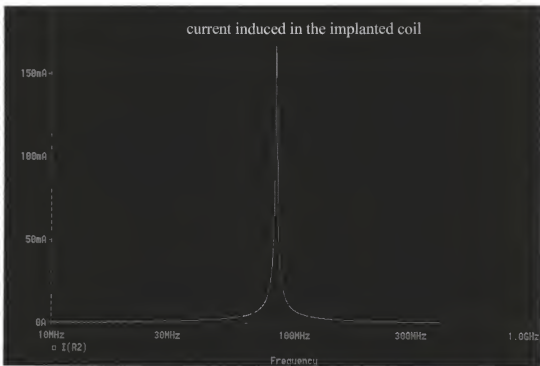


Figure 3-7 Current induced from an external coil to an implanted coil using crossed diode decoupling scheme.

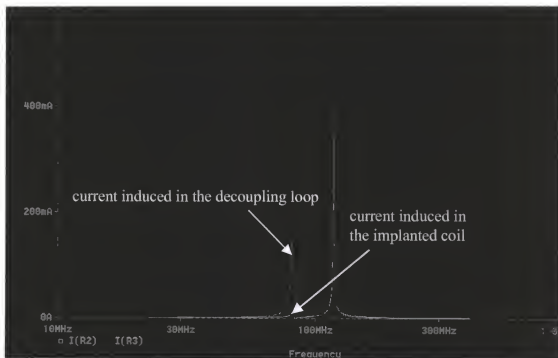


Figure 3-8 Current induced from an external coil to an implanted coil and its decoupling loop, where the resonant blocking decoupling scheme is used.

Contamination

The FOV of a coil should be as close as possible to the ROI, and the spectra should not be significantly contaminated by the signal from outside the ROI. In addition to the determination of optimal SNR, we investigated the possibility that ^{31}P NMR signal might come from the surrounding tissue. From Figure 3-10 we could see that the ^{31}P surface coil received the signal mainly from outside the ROI. However, the implanted ^{31}P coil detected the signal mainly from the ROI (see Figures 3-11 and 3-12). It can also be seen that an inductively coupled implanted coil had similar contamination as a directly driven implanted coil. Both the inductively coupled implanted coil and the directly driven implanted coil could localize the signal much better than the surface coil. From these measurements we determined that our inductively coupled implanted coil system had about 30% signal contamination from the surrounding material of the "rat body" phantom relative to the signal from the "rat spinal cord" phantom. When we first resected some of the agar gel near the implanted coil, we saw the contamination decrease. From Figure 3-14, it can be seen that the contamination decreased to 20%. The contamination was decreased only a little more when we resected additional agar gel near the implanted coil. However, when we moved the entire phantom 3 mm away from the external coil. Thus it appeared that the source of this contamination was from signal detected near the external coil elements. Near the coil elements the magnetic field can be strong even when the current is very low in the coil.



Figure 3-9. Transverse image of a rat phantom. The image was taken with a 4 cm x 4 cm ^1H surface coil

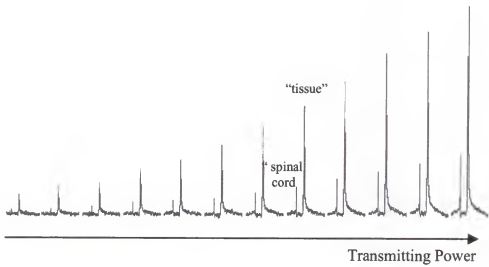


Figure 3-10. ^{31}P spectra of a rat phantom taken with a 3 cm \times 3 cm surface coil. The image from the phantom is show in Figure 3-9. The distance between the implanted coil and the external coil was 7 mm and the transmitting power was arrayed from 50 DAC (11.8 W) to 94 DAC (149.6 W) at 4 DAC (2.0 dB) interval.

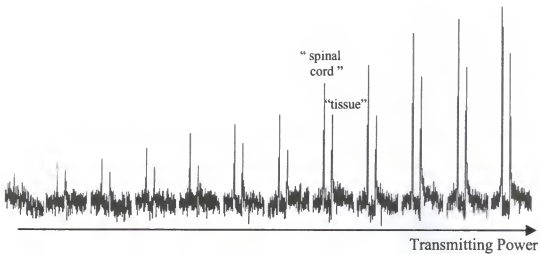


Figure 3-11. ^{31}P spectra of a rat phantom taken with a directly driven implanted coil. The distance between the implanted coil and the external coil was 7 mm and the transmitting power was arrayed from 50 DAC (11.8 W) to 94 DAC (149.6 W) at 4 DAC (2.0 dB) interval. The spectra were taken from the phantom shown in Figure 3-9.

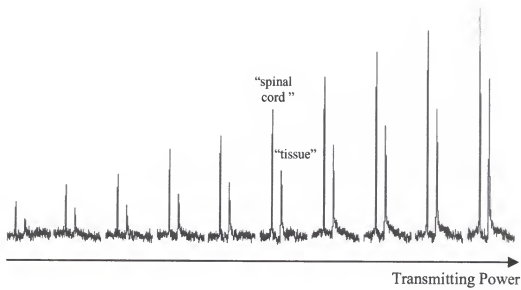


Figure 3-12 ^{31}P spectra of rat phantom taken with an inductively coupled implanted coil. The distance between the implanted coil and the external coil was 7 mm and the transmitting power was arrayed from 40 DAC (6.7 W) to 76 DAC (53.1 W) at 4 DAC (2.0 dB) interval. The spectra were taken from the phantom shown in Figure 3-9.



Figure 3-13. Transverse image of a rat phantom with the "tissue" surrounding the "spinal cord" resected. The image was taken with a 4 cm x 4 cm ^1H surface coil.

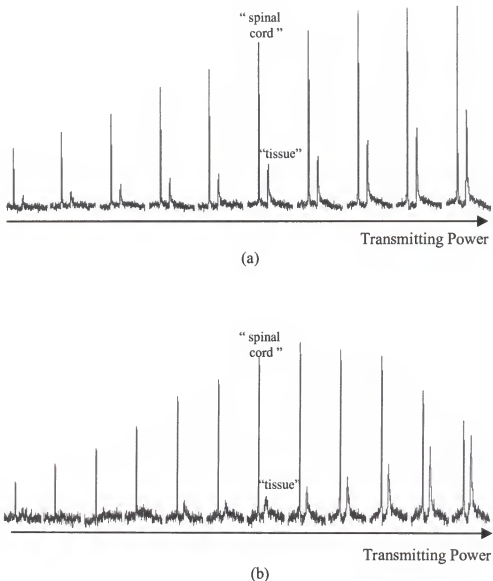


Figure 3-14. ^{31}P spectra taken with an inductively coupled implanted coil from a “rat” phantom with the surrounding “tissue” retracted. The spectra were taken from a phantom shown in Figure 3-13.

(a). The distance between the implanted coil and the external coil was 7 mm, and the transmitting power was arrayed from 50 DAC (11.8 W) to 86 DAC (94.4 W) at 4 DAC (2.0 dB) interval.

(b) The distance between the implanted coil and the external coil was 10 mm, i.e., the implanted coil moved 3 mm away from the external coil, and the transmitting power was arrayed from 50 DAC (11.8 W) to 105 DAC (about 281.8 W) at 5 DAC (2.5 dB) interval.

The IOVSISIS localized NMR technique was used to remove the contamination from the surrounding tissue. The localized spectrum from the "rat" phantom (see in Figure 3-15) was from a voxel of 5 mm x 5 mm x 5 mm with 128 scans. The SNR of the localized spectrum and the global spectrum (30% contamination) were 15 and 20 respectively. The ^{31}P concentration in the phantom was about ten times of that in the spinal cord and thus it indicated that at least 2048 scans would be required to obtain *in vivo* localized spectra from T₁₃ of a rat using the IOVSISIS localization sequence.

Susceptibility and Coupling between ^1H and ^{31}P Implanted Coil

When we examined the placement and status of the implanted coil within the rat spinal column with ^1H imaging (Figure 3-16), we noticed a distortion interfered with the image in the area of the spinal cord. These images were taken by a 4 cm x 4 cm transformer-coupled double tuned $^1\text{H}/^{31}\text{P}$ coil.

The magnetic susceptibility of the capacitor and the wire are different from the tissue leading an inhomogeneous field which, in turn, interferes with the imaging gradient fields resulting in local image distortions and the line broadening. The amount of the distortion depends on the form of the object and is proportional to the main magnetic field and inversely proportional to the magnetic gradient strength. For a cylinder oriented along y axis, the maximum spatial displacement could be evaluated by the following equation (Ludeke et al., 1985)

$$\Delta y = \Delta\chi B_0 / 2G_y, \quad [3-2]$$

where $\Delta\chi$ is the susceptibility difference between the interior and the exterior materials, B_0 is the main magnetic field and G_y is the magnetic field gradient strength in y direction.

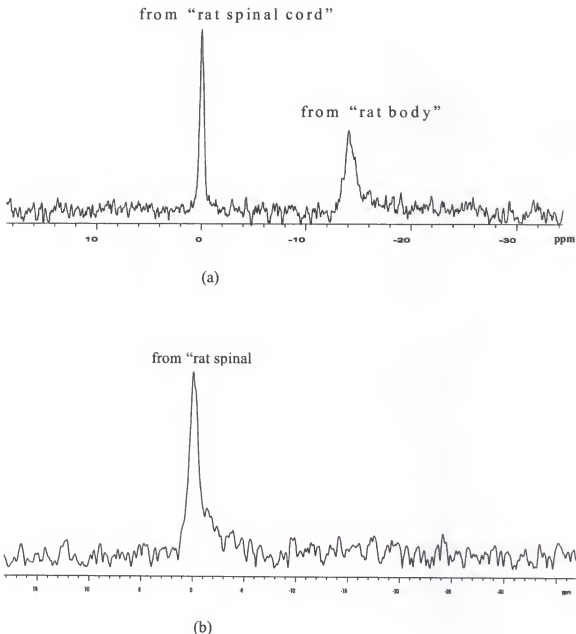
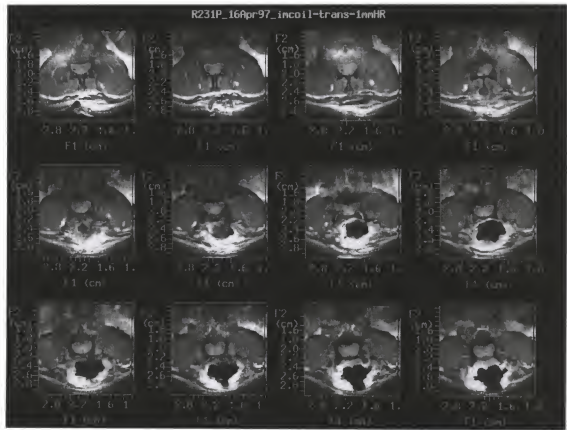


Figure 3-15. Localized ^{31}P spectrum from a rat phantom.

- (a) Global ^{31}P spectrum from the whole rat phantom, where transmitting power is 44 DAC (8.9 W) in our system and the scan number is 128;
- (b) Localized ^{31}P spectrum of a voxel 5 mm \times 5 mm \times 5 mm from the "rat spinal cord", where transmitting power is 44 DAC (8.9 W) in our system and the scan number is 128.

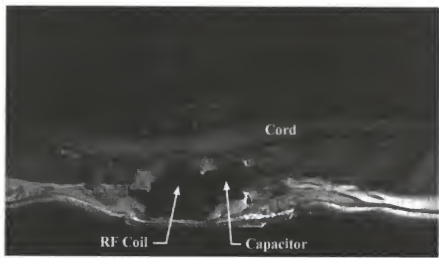


(a)

Figure 3-16. Transverse and Sagittal ^1H images of rat spinal column with an inductively coupled implanted coil on rat spinal cord. The image was taken with a 4 cm x 4 cm $^1\text{H}/^3\text{P}$ double tuned coil.

(a) Transverse image;

(b) Sagittal image.



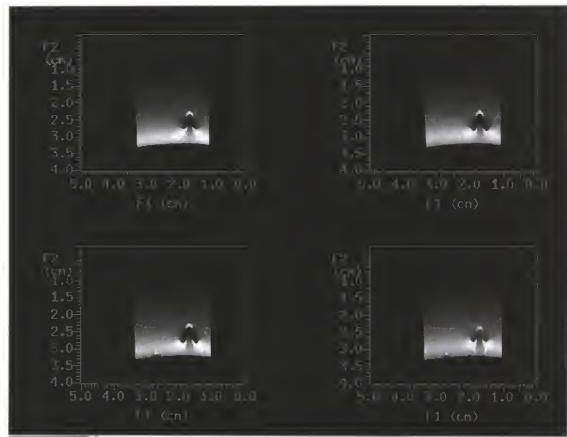
(b)

Figure 3-16 (continued)

The maximum distortion is not more than 1 mm from a coil made of copper wire ($\Delta\chi = 6 \times 10^{-6}$) working on a 4.7 T system and imaging with 1.5 Gauss/cm magnetic gradient.

In Figure 3-17 are the images of a bottle (2 cm in diameter and 4 cm in length) of water with the capacitor held in. The images shown in Figure 3-17 were taken by a quadrature surface RF coil (10 cm x 4 cm each, 10 cm x 6 cm overall) on a 4.7 T (200 MHz) system. In Figure 3-18 shows images of a 1.5 cm NMR tube that acquired with a full saddle RF coil on a 7 T (300 MHz) system. The NMR tube contained a 3-turn 4 mm x 5 mm, elliptical loop of 25 AWG copper wire surrounding by water. It can be seen that the capacitor was creating a magnetic field dependent susceptibility distortion within a few millimeters of its surface. As expected the distortion was orientation dependent and worse for the capacitor than for the wire loop. When the normal direction of the wire loop was in the z direction we almost did not see the distortion. Since the distortion as calculated was less than 1 mm, which was caused by a magnetic susceptibility difference between the materials of the coil and the surrounding water.

From Figure 3-18, we observed that when the normal direction of the wire loop was in the x direction (which is the normal direction of the saddle RF coil), the distortions were worst and symmetric about the x and y direction. However, we did not see this kind of distortion with the wire loop oriented in other direction. We concluded it to be the RF field distortion. When a wire loop is oriented in the x direction the saddle coil strongly coupled to it and thus induced a current in it. So the field from the wire loop interfered with the field from the saddle coil and caused the RF field distortion. This distortion was also tested on the 4.7 T system and similar results were obtained.



(a)

Figure 3-17. Susceptibility distortion caused by a capacitor on a 200 MHz system. The size of the capacitor is 1.3 mm x 1.3 mm x 1.2 mm. These images were taken with a quadraura surface coil.

- (a) The plate of the capacitor is oriented along x in the magnetic field coordinate system and the image slice is in the x direction.
- (b) The plate of the capacitor is oriented along x in the magnetic field coordinate system and the image slice is in the z direction.
- (c) The plate of the capacitor is oriented along x in the magnetic field coordinate system and the image slice is in the y direction.
- (d) The plate of the capacitor is oriented along y in the magnetic field coordinate system and the image slice is in the y direction.
- (e) The plate of the capacitor is oriented along z in the magnetic field coordinate system and the image slice is in the y direction.

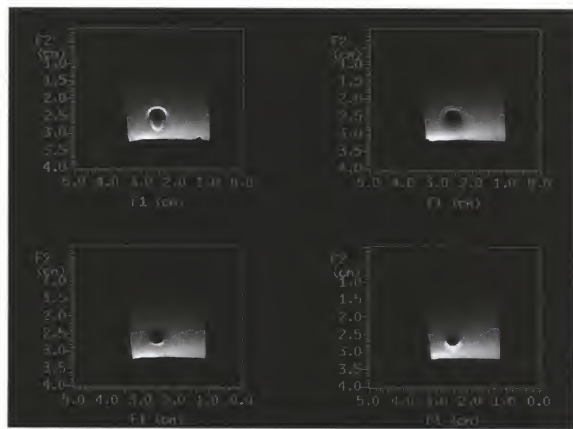


Figure 3-17 (continued)

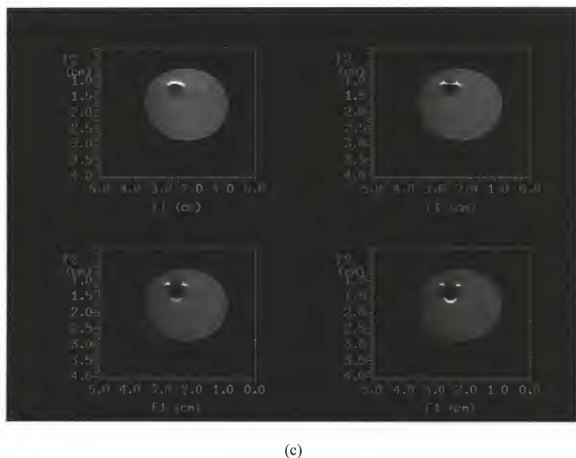
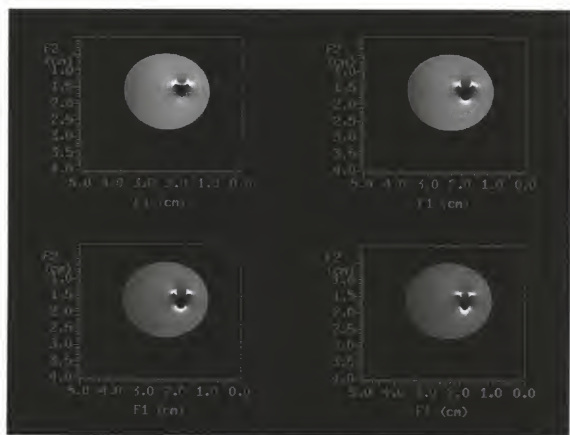
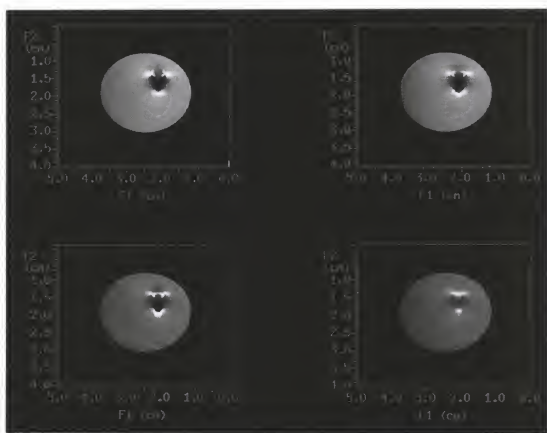


Figure 3-17 (continued)



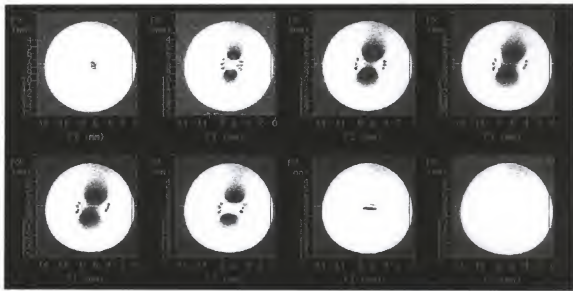
(d)

Figure 3-17 (continued)



(e)

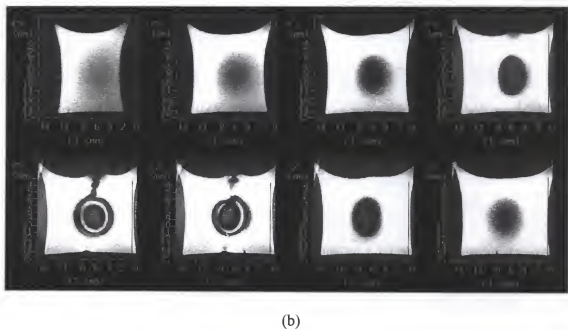
Figure 3-17 (continued)



(a)

Figure 3-18. Susceptibility and RF field distortion caused by a copper wire loop on a 300 MHz system. The wire loop is three turn 4 mm x 5 mm, elliptic shape. These images were taken with a saddle coil.

- (a) The wire loop is oriented along x in the magnetic field coordinate system and the image slice is in the y direction.
- (b) The wire loop is oriented along x in the magnetic field coordinate system and the image slice is in the x direction.
- (c) The wire loop is oriented along y in the magnetic field coordinate system and the image slice is in the y direction.
- (d) The wire loop is oriented along z in the magnetic field coordinate system and the image slice is in the z direction.

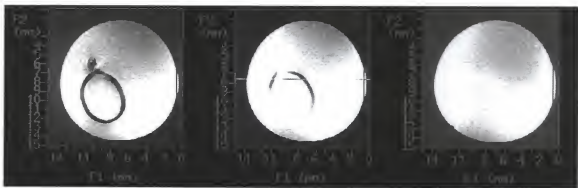


(b)

Figure 3-18 (continued)



(c)



(d)

Figure 3-18 (continued)

We used Pspice to simulate the coupling between a ^1H (4 cm x 4 cm) surface coil and the implanted ^{31}P implanted coil (see Figure 3-19). From Figure 3-19, we could see that there was a current induced in the small 4 mm x 5 mm ^{31}P implanted coil and the current was about one tenth of that in the 4 cm x 4 cm ^1H surface coil. Though the current was much smaller than that in the ^1H surface coil, the field near the small implanted coil was comparable to the field produced from the surface coil. The field from the implanted coil interfered with the field from the ^1H surface coil and caused the distortion.

The difference was similar between the coil elements and tissue or biological fluids. The distortion from susceptibility was overcome by coating the implanted coil with PMMA or by using neutral susceptibility components or by bending the wire leads which hold the capacitor so that the capacitor was up away from the spinal cord. We also used a quadrature surface coil instead of the linear double tuned ^1H coil to take images. The coupling between the quadrature coil and the ^{31}P external coil (which serves as the relay between the coupling of the ^1H coil and the implanted coil) could be minimized by adjusting the space between them (Adriany, Gruetter, 1997). Therefore the coupling between the ^1H surface coil and the ^{31}P implanted coil could be minimized. The quadrature surface coil also provided images with high SNR. These modifications minimized the susceptibility distortion and the RF field distortion, which could be seen from Figure 3-20.

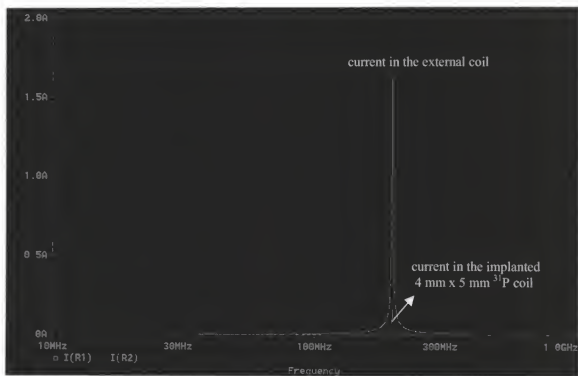


Figure 3-19. Coupling between a 4 cm x 4 cm ^1H surface coil and a 4 mm x 5 mm implanted ^{31}P coil.

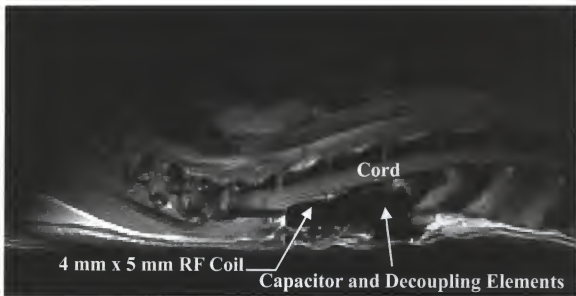


Figure 3-20. Sagittal image of a rat with a receive-only ^{31}P coil implanted on the spinal cord. It was taken with a quadrature surface coil (10 cm x 4 cm each, 10 cm x 6 cm overall).

Test of ^{31}P RF Coil Implanted on a Rat Spinal Column

We implanted an inductively coupled ^{31}P RF coil in each of six rats within the spinal columns over the site of laminectomy at T₁₂ and T₁₃ (see Figure 3-4). Two rats died due to complications, i.e., hypothermia following surgery. Thus we subsequently delayed a few days following surgery to reduce the overall stress to the animal and then measured ^{31}P MR spectra. In a third rat we acquired ^{31}P MR spectra once per week following surgery for a month. A representative spectrum taken by a one-pulse-acquire sequence shown in Figure 3-22. All resonances of the spectra were superimposed on top of a broad peak that came from bone. This broad resonance spanned from -30 ppm to 30 ppm. We used convolution difference to subtract the broad resonance and correct the baseline. The spectrum might be contaminated by the surrounding tissue. However, it clearly indicated the quality of the spectra that we were able to obtain in a relatively short time of 20 minutes.

However two months after surgery, the PMMA covered RF coil broke through the skin and was expelled from the animal. We contributed this to the fact that we did not suture the connective tissue immediately above the PMMA plug. Therefore the tissue built up scar tissue around the PMMA and forced the PMMA free from the spinal column and out of the tissue.

Then the fourth animal implantation procedure was performed. For this animal, we further modified the coil implantation procedure. For the previous animal, the RF coil had been covered with PMMA during the surgery with the coil in place in the laminectomy site above the spinal cord. Using this procedure, we found it difficult to control the form and the shape of the PMMA coating. Therefore, we did not follow the

procedure for this animal. Before implanting the coil in this animal, the RF coil was coated in PMMA and the coating was shaped to provide a smooth and thin surface (1 mm thick, as mentioned above) on the side next to the spinal cord. The capacitor was mounted away from the spinal cord and turned so as to provide the minimum susceptibility distortion. We also rounded the top of the PMMA surface, which was to go next to the surrounding tissue. We sutured the connective tissue closed over the site of implantation. It was observed that the implanted coil was functioning very well and the animal had no infections around the implanted coil. Unfortunately the system had broken down for more than two months and the rat died from some disease.

For the fifth animal, the receive-only (transmission-decoupled) coil design was implanted using the modified procedure described above for handling the PMMA. Then we measured the ^{31}P spectrum for this animal with the standard a one-pulse acquire sequence (see Figure 3-23). This receive-only coil system allowed us to use IOVSISIS localization technique to obtain signal from the ROI while providing high SNR. We obtained localized ^{31}P from a voxel slightly larger than the spinal cord region of a dead rat with 1024 scans. However, the IOVSISIS localization technique degraded the sensitivity of NMR due to the sensitivity to the motion. In fact, other investigators have reported that it is extremely difficult to obtain localized ^1H spectra from the rat spinal cord without respiratory gating (Zelaya et al., 1996). Naturally, we were unable to obtain localized ^{31}P from the spinal cord of a rat without respiration gating.

For the sixth animal, the receive-only coil coated with PMMA in a dome shape (3 mm on the side of the coil and 4 mm on the top of the coil) was implanted. The coating of the PMMA prevented the paraspinal muscle from entering sensitive volume of the ^{31}P RF

coil and reduced the signal from the surrounding tissue. In addition the separation between the external coil and the rat was held at 3 mm to greatly reduce the signal from the tissue near the elements of the external coil. This implanted coil design function well and the animal had no infections or reactions to the implanted coil.

The location of the implanted coil is shown in Figure 3-24 and a representative spectrum taken by a one-pulse acquire sequence from a rat three days after surgery is shown in Figure 3-25. In this spectrum, the PCr to β -ATP ratio is about 2, as expected for nervous tissue (Hida, et al., 1992). Therefore, this spectrum does not appear to be contaminated by the signal from the surrounding tissue and it clearly indicated the quality of the spectra that we were able to obtain in a relatively short time of 20 minutes. From this *in vivo* spectrum, we determined the pH to be 7.26 by applying Eq. [3-1], which showed the rat was healthy and PCr/Pi ratio to be 1.23. The reason for high Pi and thus, low PCr/Pi ratio might be that the rat was under anesthesia and therefore the oxygen delivery was low.

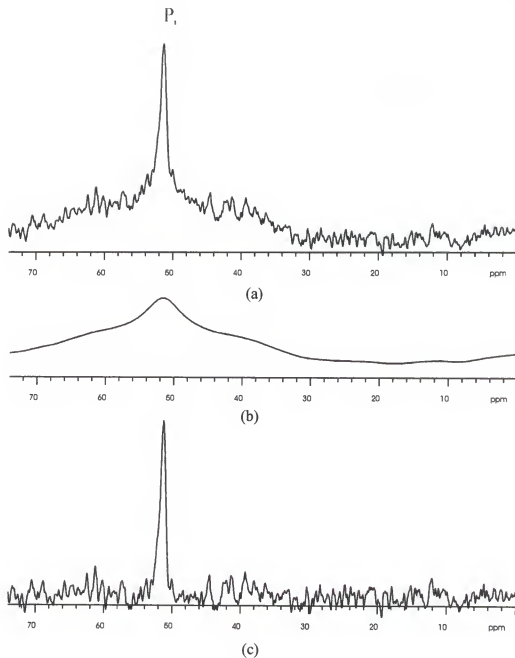


Figure 3-21. ^{31}P spectra of a dead rat taken with an inductively coupled implanted transmit/receive ^{31}P coil.

- (a) Original spectrum.
- (b) Same as (a) except a 600 Hz broadening exponential multiplication was used (a resonance from bone).
- (c) Difference spectrum of (a) minus (b).

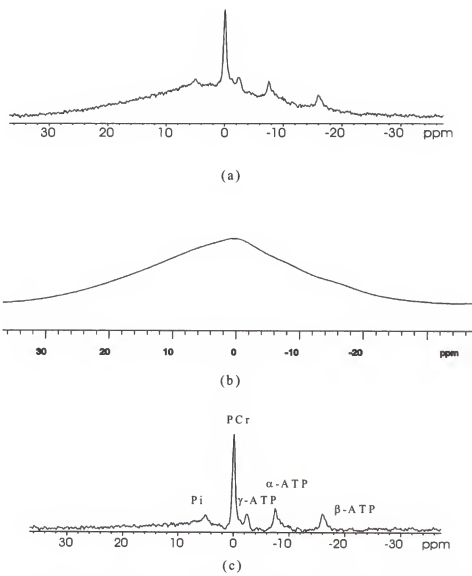


Figure 3-22 *In vivo* ^{31}P spectra of a rat taken with an inductively coupled implanted transmit/receive ^{31}P coil. The spectrum was taken with 512 scans in 20 minutes.

- (a) Original spectrum.
- (b) Same as (a) except a 600 Hz broadening exponential multiplication was used (a resonance from bone).
- (c) Difference spectrum of (a) minus (b).

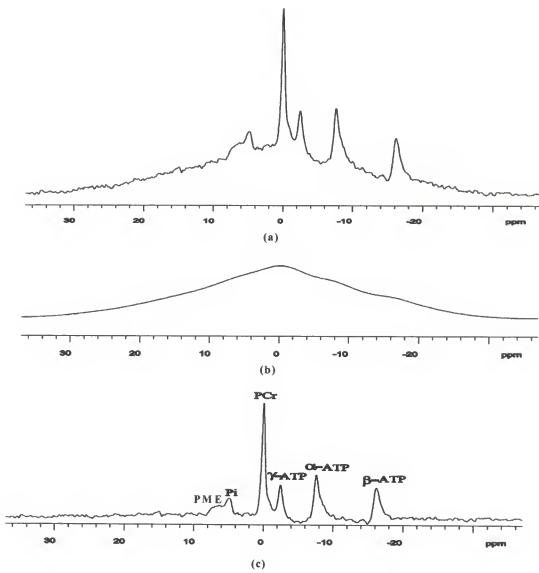
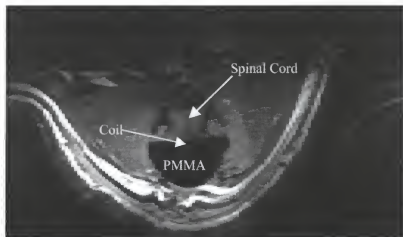
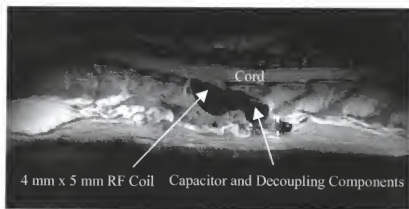


Figure 3-23. *In vivo* ^{31}P spectrum of a rat taken with an inductively coupled implanted receive-only ^{31}P coil. The spectrum was taken with 512 scans in 20 minutes.

- (a) Original spectrum.
- (b) Same as (a) except a 600 Hz broadening exponential multiplication was used (a resonance from bone).
- (c) Difference spectrum of (a) minus (b).



(a)



(b)

Figure 3-24. Image of a rat with a receive-only ^{31}P coil coated with PMMA in dome shape and implanted on the spinal cord. It was taken by a quadrature surface coil (10 cm x 4 cm each, 10 cm x 6 cm overall).

(a) Transverse image.

(b) Sagittal image.

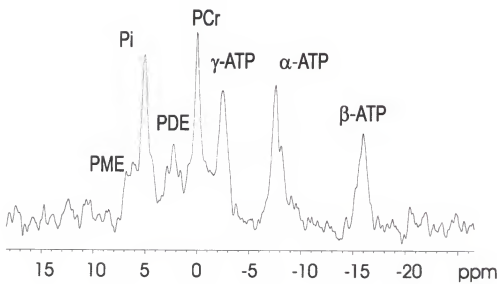


Figure 3-25. *In vivo* ^{31}P spectrum of a rat taken with an inductively coupled implanted receive-only ^{31}P coil coated with PMMA in dome shape. The spectrum was taken with 512 scans in 20 minutes.

Conclusion

The results show that the optimized inductively coupled implanted coil with the decoupling circuit can be placed on the spinal column to maximize SNR. Using inductively coupled implanted RF coils, we have demonstrated the feasibility of measuring ^{31}P spectroscopy *in vivo* from a highly localized region of spinal cord tissue. Our coil design resulted in high SNR that allows the acquisition of the high quality spectra, without apparent contamination from surrounding tissue, in a relatively short time.

Our research indicates that although laminectomy may temporarily depress spinal cord blood flow, spinal cord energy metabolism is not adversely affected by the procedure. Therefore the ^{31}P NMR spectra can provide information regarding normal spinal cord metabolism. We do not find any adverse effects from laminectomy or the chronic RF coil implantation on energy metabolism in these rats. With this coils, we can monitor spinal cord metabolism following injury and repair on a longitudinal basis for extended periods [from the acute (hours to days) to the chronic phase (months to years)].

CHAPTER IV

INDUCTIVELY COUPLED QUADRATURE IMPLANTED RF COILS

Introduction

When two coil systems are orthogonal, they are completely independent, and the noise in the two receiving circuits is uncorrelated. It follows that, with an approximate 90^0 phase shift, the signals may be combined to give $\sqrt{2}$ improvement in SNR (Chen et al., 1983; Fitzsimmons, Beck, 1992; Hoult et al., 1984). The orthogonal coils may be used to generate a rotating B_1 field that efficiently uses transmitting power, since no wasted counter-rotating B_1 component is generated. A saving of a factor of 2 in power might therefore be expected.

Therefore this work combined the features of an implanted coil with the quadrature detection. We designed a quadrature detection implanted coil, which is inductively coupled to a quadrature excitation/reception surface coil to improve the SNR of our linear implanted coil system (Wirth et al., 1993).

Review of Literature

An inductively coupled implanted coil, which made chronic high-quality spectroscopy of deep internal structures feasible in a “relatively undisturbed system”, was extended to NMR microscopy and showed a ten-fold increase in the SNR over whole body birdcage coils in a study of rat kidneys (Hollett et al., 1987). The design of NMR

coils for insertion into peripheral orifices of the body and the possibility of using parasitic coils without direct connections in conjunction with conventional whole body coils were studied (Harman et al., 1988). Later on a surgically implanted RF coil, approximately 2.5 mm radius, 22 AWG tinned copper wire, inductively coupled to a 2.0 cm diameter circular RF coil, was used to study rat carotid artery at 300 MHz by magnetic resonance microscopy (MRM) (Arnder et al., 1994). The study showed that the coil was good for localizing the ROI. Further, a similar coil with a diameter 5 mm x 7 mm was used and the SNR improvements were sufficient to define the wall of the carotid artery after balloon injury (Summers et al., 1995). Then an implanted coil was also used to study of rat liver (Zhou et al., 1994) and it was demonstrated that the implanted coil could be used to follow pathological changes in living tissue successfully. An implanted RF coil was also used to obtain high resolution *in vivo* MRI from an injured rat spinal cord on a 1.9 T system. The calculation of the relative SNR revealed an increase in sensitivity for the circular implanted coil over that of the external surface coil by a factor of 10.4 and 12 for a square implanted coil (Ford et al., 1994). An inductively coupled coil (copper/Teflon/copper substrate, 3 cm middle diameter, 8 mm width), coupled to a pick-up coil was constructed to minimize the magnetic susceptibility and used to study the rat spine on a 7.0 T (Banson et al., 1992) system.

A preliminary investigation of quadrature coil design revealed the feasibility of quadrature detection (Chen et al., 1983). The theory underlying the quadrature coils was developed and the potential, particularly with regard to imaging and biomedical studies was explored in more detail (Hoult et al., 1984).

The work of our research group has shown that linear inductively coupled implanted RF coils could provide a significant gain in SNR for imaging the spinal cord relative to the SNR of optimized surface coil (Wirth et al., 1993). The overlying muscle structure contaminates the signal received by surface coils and the actual filling factor due to the small volume of the spine itself is low. To overcome these limitations, implanted coils were placed under the muscle and directly on the vertebrae over the spinal cord, the ROI, thus limiting the FOV to the spinal cord alone. However, the surrounding muscle tissue is a very lossy dielectric and serves as a very heavy load upon the coil that negatively affects coil sensitivity. An implanted coil was constructed of a single rectangular loop of round wire bent in the shape of a half saddle (matching the symmetry of the cat vertebrae structure), and resonant blocking circuit decoupling schemes were applied to the implanted RF coil (Edelstein et al., 1986; Hyde et al., 1990). The spinal imaging and spectroscopic applications were performed on a cat model at a 2.0 Tesla (85.5 MHz) system. Despite the heavy sample loading, *in vivo* SNR of this prototype implanted coil system was 2.19 times the SNR of the optimized linear surface coil and 1.65 times the SNR of the optimized quadrature surface coil (Wirth et al., 1993).

Although inductively coupled linear implanted RF coils provided a significant gain in SNR for imaging the spinal cord compared to the SNR of optimized surface coils, quadrature detection coils offered an additional, potentially significant gain in SNR (Fitzsimmons, Beck, 1992; Fitzsimmons et al., 1993; Fitzsimmons et al., 1989; Hoult et al., 1984; Hyde et al., 1987). Therefore, we examined the feasibility of a coil system combining both features of inductive-coupling and quadrature detection. Our design uses an implanted quadrature coil pair inductively coupled to an external quadrature

transmitting/receiving coil pair. We investigated whether this design would have significant gains in performance over an inductively coupled linear implanted RF coil. We also determined the optimal dimensions of the coil system for the ROI, i.e. the spinal cord, and compared the SNR between the following four types of coil systems:

- a) A transmit-only linear surface coil and receive-only linear surface coil pair;
- b) A transmit-only linear surface coil and receive-only quadrature surface coil;
- c) A transmit-receive linear surface coil coupled to receive-only linear implanted coil;
- d) A transmit-receive quadrature surface coil coupled to receive-only quadrature implanted coil.

Method

Simulations

The Maxwell 3D Field Simulator (Ansoft Corporation, Pittsburgh, PA) was used to calculate the magnetic field of coils operating at 200 MHz frequency (the Larmor frequency of proton in 4.7 Tesla) with unit current. Figure 4-1 illustrates the spatial arrangement of an implanted quadrature pair inductively coupled to an external quadrature pair and Figure 4-2 illustrates the structure of the implanted coil pair. These quadrature coil pairs were concentric with respect to the central axis of their cylindrical former and to each other. The implanted coils had a length of 4 cm, a radius of 1 cm, 100 degree angular length for each and the sum of the overlapped arcs subtended 180 degrees.

The external coils had a radius of 7 cm, a length of 14 cm, 100 degree angular length for each and the sum of overlapped arcs also subtended 180 degrees.

We calculated the self-inductance, mutual inductance and the corresponding coupling constants of the coils in the presence of a 2 mm radius cylinder of simulated spinal cord and 6 cm radius cylinder of simulated muscle tissue, 14 cm in length, which are concentric with the implanted coils. The calculations were repeated for a range of distances (when the implanted coil pair and the external coil pair are concentric, the distance is 70 mm) varied from 30 mm to 70 mm at 10 mm intervals.

Obtaining uniform excitation is important for accurately comparing the sensitivities of the implanted and the surface coils. Otherwise, the results could be confounded by tip angle variation during excitation. In order to optimize the homogeneity in 1 cm^3 region, 2 cm from the arc center of the external coil pair (i.e., the approximate location of the spinal cord relative to the coil used), the magnetic field of various coil sizes were simulated.

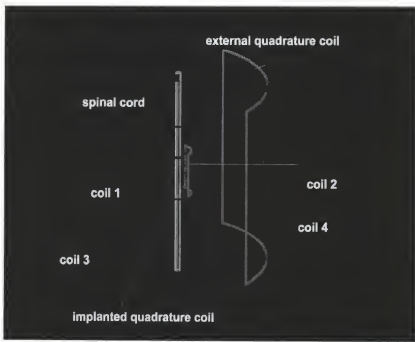


Figure 4-1. Configuration of a quadrature inductively coupled implanted coil.

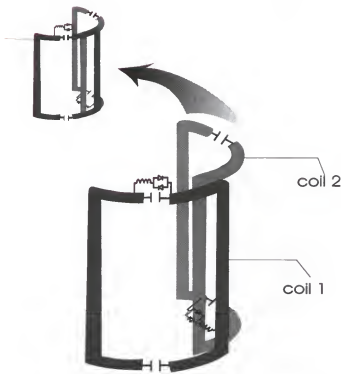


Figure 4-2. Configuration of a quadrature implanted coil. It indicates the relative layout of coil structure and placement of components. The two coils (4 cm x 2 cm each, 4 cm x 3.2 cm overall, bent on a cylindrical former with 1 cm radius to form a half saddle shape) together form the receive-only quadrature implanted coil.

RF Coil Design

The use of a large coil for transmitting and a small surface coil for receiving can combine the high sensitivity of small coils for reception and the field homogeneity of large coils for excitation. However, a method for decoupling the transmitting coil from the receiving coil during transmission is required to obtain the homogeneous magnetic field, which is also required for protecting the sample against possible RF heating and preventing the capacitor from burning. From the theoretical calculation and the Pspice simulation shown in the previous chapter, the resonant blocking circuit scheme is a more effective decoupling scheme for our coil system.

a.) Transmit-only linear surface coil and receive-only linear surface coil

The receive-only linear surface coil consisted of a single 10 cm x 6 cm rectangular (Figure 4-3 (a), inner loop A), constructed with 6 mm wide copper foil, centered within the transmit coil (Figure 4-3 (a), outer loop B, refer to the following discussion) and mounted on a cat cradle. The cradle was a Plexiglas, half-cylinder with dimensions of 77.5 cm length, 14 cm outer diameter, 12.5 cm inner diameter. The cradle was also used to support a cat during the imaging. The corresponding schematic diagram is shown in Figure 4-3 (b) (and Figure 4-3 (c)).

b.) Transmit-only linear surface coil and receive-only quadrature surface coil

The quadrature coil pair (Figure 4-4 (a), coil A & B) was constructed with a pair of circuit loops that were overlapped by a specific amount to minimize their mutual inductance. To obtain a FOV equivalent to that of the linear surface coil, shown in Figure

4-3 (a), each loop of the quadrature pair was 10 cm x 4 cm, constructed from 6-mm wide copper foil. In addition, inductors and PIN diodes were used to decouple the quadrature coil pair from the excitation coil (Figure 4-4 (a), coil C, refer to the following discussion) in a similar fashion to that described for a receive-only linear surface coil. The corresponding circuit diagram is in Figure 4-4 (b).

c). Transmit-receive linear surface coil coupled to receive-only linear implanted coil

The implanted coil (Figure 4-5 (a) coil A) consisted of a half-saddle shaped loop (4 cm x 2 cm x 1 cm) of coated copper wire (16 AWG) with two breaks. The physical layout of this coil, along with the excitation coil is shown in Figure 4-5 (a) (refer to the following discussion). The corresponding circuit diagram is shown in Figure 4-5 (b).

d). Transmit-receive quadrature surface coil coupled to receive-only quadrature implanted coil

The quadrature implanted coils consisted of a pair of rectangular loops (4 cm x 3.2 cm) with 1 cm radius of enamel-coated copper wire (16 AWG) and two breaks. The rectangular loop was bent on a cylindrical former to form a saddle shape, 4 cm x 2 cm x 1 cm, in length, width and height respectively, as shown in Figure 4-2. The separation between the capacitors was 7.2 cm, which is less than $\lambda/20$ (at 200 MHz), and implies that there is a uniform current in the coil. The coil pair overlap was adjusted to minimize mutual inductance. The corresponding circuit diagram of the implanted and external quadrature coils is shown in Figure 4-6.

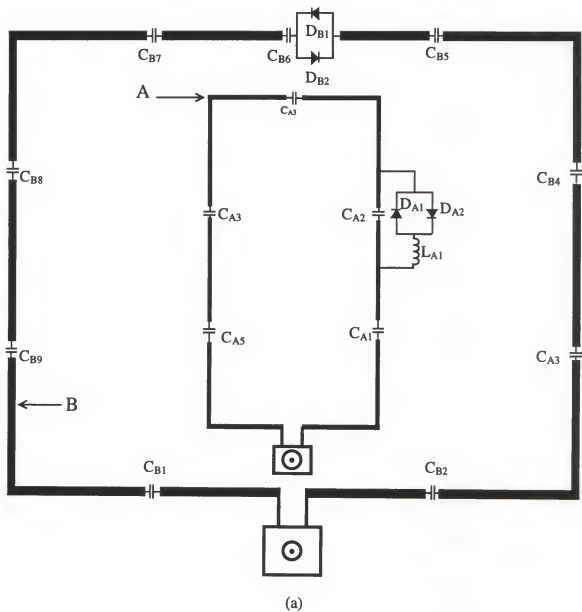
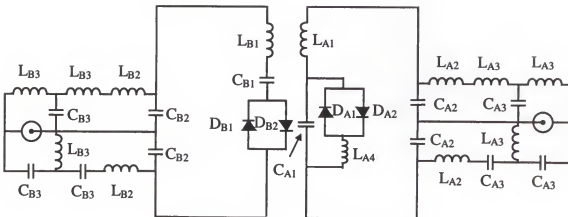


Figure 4-3. Configuration and schematic diagram of a transmit-only and receive-only linear surface coil pair.

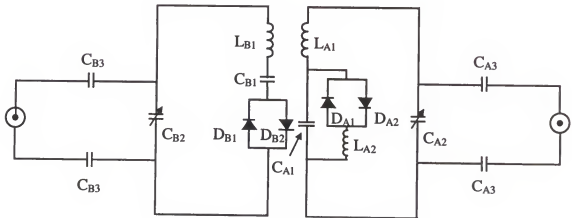
(a). Configuration: Coil A (10 cm x 6 cm) is the receive-only (RX) linear surface coil and coil B (14 cm x 20) is the transmit-only (TX) linear surface coil.

(b). Schematic Diagram: the right is the transmit-only excitation coil and the left is the receive-only reception coil, both coils used a balanced matching circuit shown in Figure 2-7.

(c). Schematic Diagram: the right is the transmit-only excitation coil and the left is the receive-only reception coil, both coils used a conventional balanced matching circuit shown in Figure 2-5.

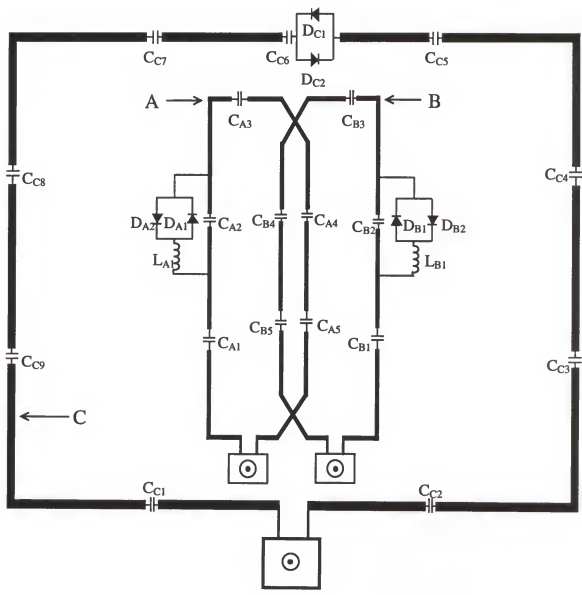


(b)



(c)

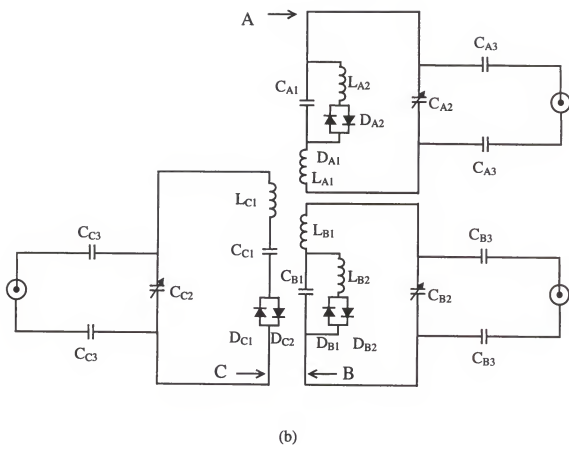
Figure 4-3 (continued)



(a)

Figure 4-4. Configuration and schematic diagram of a transmit-only linear surface coil and receive-only quadrature surface coil.

- (a) Configuration: Coil C (14 cm x 20 cm) is the transmit-only linear surface coil. Coil A and B (10 cm x 6 cm overall) together form the receive-only quadrature surface coil.
- (b) Schematic diagram: C is the schematic diagram of the transmit-only linear excitation surface coil. A and B are the schematic diagram of the receive-only quadrature detection coil.



(b)

Figure 4-4 (continued)

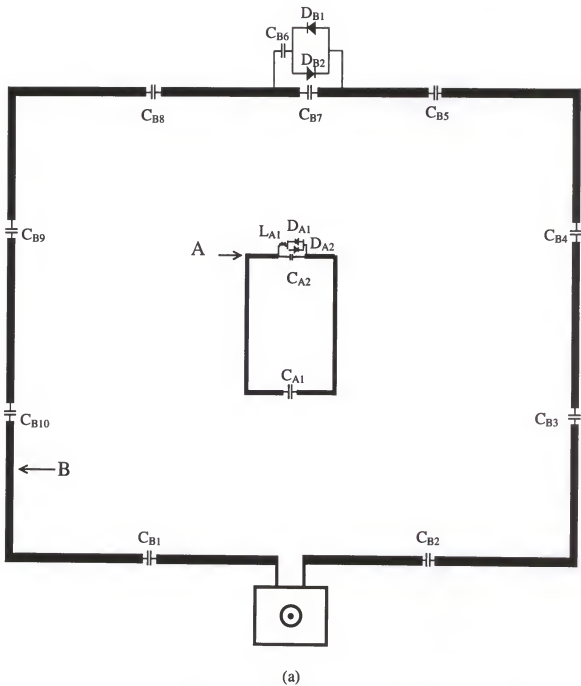


Figure 4-5. Configuration and schematic of an inductively coupled linear implanted coil.
 (a) Configuration of the linear implanted coil system. Coil A (a saddle shape with length, width and height of 4 cm x 2 cm x 1 cm) is the receive-only linear implanted coil. Coil B (14 cm x 20 cm) is the transmit-receive linear surface coil.

(b). Schematic diagram of the linear implanted coil system. A is the schematic diagram of the transmit-receive linear surface coil, which is used for excitation and reception of the signal detected by the implanted coil. B is the schematic diagram of the implanted coil.

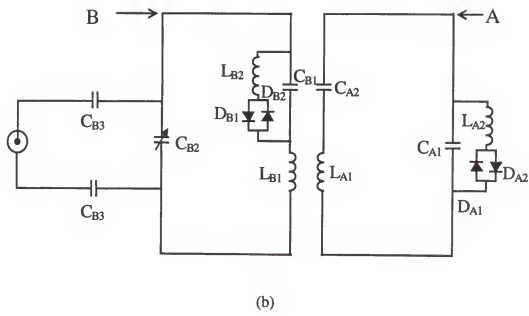


Figure 4-5 (continued)

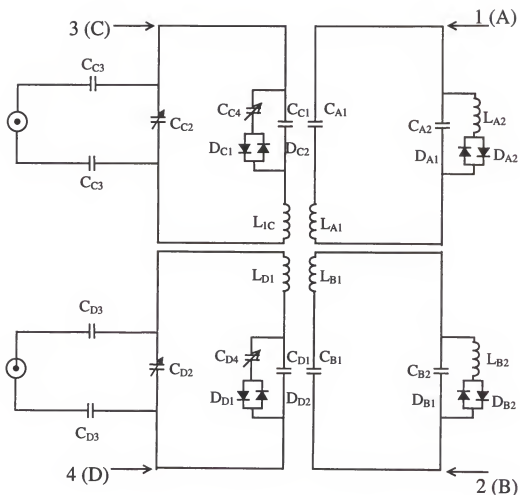


Figure 4-6. Schematic diagram of a quadrature inductively coupled implanted coil. The external coil serves as both an excitation coil and as a pick-up coil to inductively detect signal emitted by the implanted probe. The external coils C and D (right) are mutually coupled to implanted coils A and B (directly coupling M_{AC} and M_{BD} ; crossed coupling M_{AD} and M_{BC}). Implanted coil pair and external coil pair themselves are also mutually coupled (M_{AB} and M_{CD} respectively). The balanced matching circuit is used to match the external coil to 50Ω and tuned to 200 MHz. The matching of the implanted coil is achieved through the external coils. 1, 2, 3, and 4 were the labels in the inductively coupled quadrature implanted coil layout.

In cases a, b, and c, the transmission coil was constructed to be large so that the excitation could be performed in a relatively homogeneous RF magnetic field over the ROI (i.e., the spinal cord). The ROI was 1 cm³ region located 2 cm along a line perpendicular to the plane of the external coil. As shown in Figure 4-7, the variation of the field in ROI was less than 10%. The large excitation coil, 14 cm x 20 cm, illustrated in Figures 4-3 (a), 4-4 (a), and 4-5 (a) (outer loop) was constructed of 12 mm wide copper foil with adhesive backing and nonmagnetic capacitors and the coil was mounted on a cat cradle. A pair of crossed PIN diodes (UM-7201, Unitrode, Corp. Inc, Lexington, MA) was placed in series with the transmit coil to minimize coupling with the receive-only RF coil during signal acquisition for case a and b.

In case d, a large external quadrature surface coil with overall dimension of 14 cm x 20 cm was constructed to have a relatively homogeneous RF magnetic field over the ROI (i.e., the spinal cord). The quadrature surface coil consisted of two 14 cm x 12 cm coils overlapped by a specific amount (when the two peaks merged to one peak, if each coil resonated at the same frequency) to minimize their mutual inductance. In cases c and d the large external surface coil was used for excitation and as a pickup coil to detect the signal from the implanted coil. This was accomplished by simply not adding PIN diodes in series to the external coil. Since two circuits tuned to the same frequency would split into two separate resonances when placed in close proximity, the implanted coil was pretuned to a frequency below or above 200 MHz. After coupling with the external coil, the higher or the lower of the two resonance peaks could be tuned to be 200 MHz. The lower frequency was in the co-rotating mode (the direction of current flowing in a coil is

the same as that in the coupled coil). The higher resonance was in the counter-rotating mode (the direction of current flowing in a coil is opposite to that in the coupled coil). We chose to use the co-rotating mode, since this mode within the ROI the magnetic field would be the sum of the field from the implanted and external coil and provided higher SNR.

A resonant blocking circuit, in parallel with the receiving coil, is shown in Figure 4-3, Figure 4-4, Figure 4-5 and Figure 4-6. This was accomplished by placing a series combination of an inductor (L_2) (L_4 in Figure 4-3 (b)), crossed PIN diodes D_1 and D_2 (Motorola, MBD-301, Motorola Semiconductor Products, Tempe, AZ) in parallel with a capacitor (C_1) of the receive coil. The value of the inductor was chosen such that resonance was attained at 200 MHz for 1H (the Larmor frequency for 1H on a 4.7 Tesla system) with the value of the parallel capacitor (C_1). The labels in the schematic diagram had index A, B, C or D that corresponded to coil A, B, C or D respectively.

For the transmit-only and the receive-only surface coil systems, we also provided crossed diodes in series with the transmit-only coil. During transmission, a strong current flows in the transmitting coil and the receiving coil resonant blocking circuit, which activated the diodes in both the transmitter coil and the receiver coil. The resonant circuit L_2-C_1 , therefore, has a high impedance circuit and prevented significant current flowing in the receiving coil. Thus, RF excitation got through to the sample essentially unaffected by the presence of the receive coil. Eq. [2-56] states that the value of Q must be substantially greater than the number of capacitors distributed around the coil, so that the uniformity of the excitation RF B_1 field is unaffected by the currents in the receiver coil. For the 10 cm x 6 cm receiving coil, the number of the capacitors was 6, the unloaded Q

was 35 and loaded Q was 27; for the implanted coils, there were two breaks, the unloaded Q was 150 and the loaded Q was 50 so the condition in Eq. [2-56] held. The greater the Q damping with the implanted coils means that they are coupled to the sample better and, thus, should have higher SNR (Fitzsimmons et al., 1987).

During the receiving phase of the experiment, a small current flows in the receiving coil so that the diodes in the resonant blocking circuit and in the transmitting coil are not activated. Therefore the impedance of the resonant blocking circuit is small and all the induced current is in the receiving coil. The diodes in the transmitting coil are not activated either and a negligible current flows in the transmitting coil, which produces a very small B_1 field, which only slightly distorts the field from the receiving coil, and no extra noise appeared in the NMR signal from transmitting coil. The signal from the receiving coil is therefore not degraded.

Once the electronic components of the implanted coils were soldered in place, it was sealed in a biomedical grade silicone elastomer with excellent dielectric properties (Dow Corning, MDX4-4210). After silicone sealant had fully cured (approximately 24 hours), the coils were sealed in sterilization bags and gas sterilized by ethylene oxide.

A 1 cm diameter cylindrical tube phantom filled with 0.3% saline and 0.01 M CuSO₄ was used for the quantitative comparison of the SNR of the four types of coil systems. The center point of the phantom was located at 20 mm, 26 mm and 32 mm from the surface center of the external coil pair, where the phantom and the cradle are parallel. The NMR image slice was perpendicular to the long axis of the phantom (z direction of the main magnetic field). The power level was adjusted to achieve a 90° flip angle at the targeted region. A conventional spin echo pulse sequence was used with TR=0.5 s and

TE=26 ms. The attenuation and gain were held constant for all four coil systems. Transverse images with a FOV of 8 cm x 8 cm (256 x 256 points) were acquired with a slice thickness of 1 mm. The SNR of the image at the target region was determined by the ratio of the mean signal intensity minus the mean noise background, to the mean standard deviation of the noise in the background, i.e., in the regions devoid of signal:

$$\text{SNR} = \frac{\text{mean of signal} - \text{mean of noise}}{\text{standard deviation of noise}} \quad [4-1]$$

Then SNR was measured from the images taken by the four types of coil systems. Subsequently, the SNR was measured from the images of a "cat phantom". The "cat phantom" consisted of a 1-cm diameter cylindrical saline tube and two bags (1 litter) filled with 0.3% saline. One bag was placed underneath the saline tube and another bag was placed above the saline tube. The saline tube to used to mimic a cat's spinal cord and the two saline bags were used to mimic the body tissue above and underneath the spinal cord. For the SNR comparison the linear surface coil was optimized by using a balanced matching circuit shown in Figure 2-7. Finally the implanted quadrature coil pair was evaluated with an extracted spinal cord. The extracted spinal cord was placed in a 1 cm tube. Images were acquired from this phantom to show the clarity of the images taken by the four coils.

Results

The optimal coil dimensions were determined from the plots of the magnetic field of various sizes of coils to be 10 cm x 6 cm for the receive-only linear surface coil and 14

cm x 20 cm for the transmit-only surface coil. The plot of magnetic field (B_1)_{xy} is shown in Figure 4-7 and Figure 4-8.

A 1 cm radius coil is the smallest size coil that will fit over the upper lumbar cat spine. Therefore, we simulated the magnetic field of this coil with various lengths. The optimal dimensions for the quadrature implanted coil pair were determined to be 1 cm radius, and 4 cm length, 180 degrees combined total arc length, 100 degree arc length for each coil of the pair. Coils with these dimensions matched the symmetry of the cat vertebrae and produced the most homogeneous magnetic field over the ROI while maintaining a stronger magnetic field than other dimensions. Figure 4-9 shows a simulation of the transverse cross sectional magnetic field, B_1 of the implanted coil. The two coils are driven with a unit current and 90 degrees phase difference between the current in each coil.

Table 4-1 shows the calculated self-inductance and the mutual-inductance between coils when the implanted pair and the external pair are concentric. The corresponding coupling constants shown in Table 4-2 and Figure 4-10 indicate that the coupling between each coil of the implanted coil pair is very small and the cross coupling of implanted coils and external coils is much less than the direct coupling between them. The coupling between each coil in the external coil pair is larger than the direct coupling between the implanted and external coil. Adjusting the amount of the overlap can minimize the coupling between the external coil pair and the coupling between the implanted coil pair.

The simulation results (see Figure 4-11) shows that the direct and cross coupling constants between the implanted and the external coils vary with the distance between

their centers. The direct coupling of the implanted coil and the external coil changes more rapidly than that of the cross coupling. Since we want strong direct coupling and weak cross coupling, the distance between the centers of the implanted and the external coil pairs were put as close as possible. However, the location of the spinal cord limits the farthest distance to be 4 cm between the coil centers.

The 4 cm x 2 cm x 1 cm quadrature implanted coil with two-capacitor breaks in the arcs was found to be the construction that produced the best SNR. The overlapping of the pair of coils can be adjusted to minimize the mutual inductance so that there is only one resonance frequency peak for the combined coils. The sum of the overlapping is constrained to be 180 degrees.

Table 4-1. Inductance matrix of a quadrature inductively coupled implanted coil.

Unit (nH)	Implanted coils		External coils	
	coil 1	Coil 2	coil 3	coil 4
Coil 1	73.0±5.00	0.00±0.00	2.50±0.02	0.20±0.00
Coil 2	0.00±0.00	73.0±5.00	0.20±0.00	2.50±0.00
Coil 3	2.50±0.02	0.20±0.00	815.±55.0	25.0±1.00
Coil 4	0.20±0.00	2.50±0.02	25.0±1.00	815.±55.0

Table 4-2. Coupling constant between coils in a quadrature implanted coil system.

Implanted Coils	Implanted Coils--External Coils		External Coils
Coil 1-coil 2	coil 1-coil 3 coil 2-coil 4	coil 1-coil 4 coil 2-coil 3	coil 3-coil 4
0.0 0±0.000	0.010± 0.001	0.001±0.000	0.030+0.002

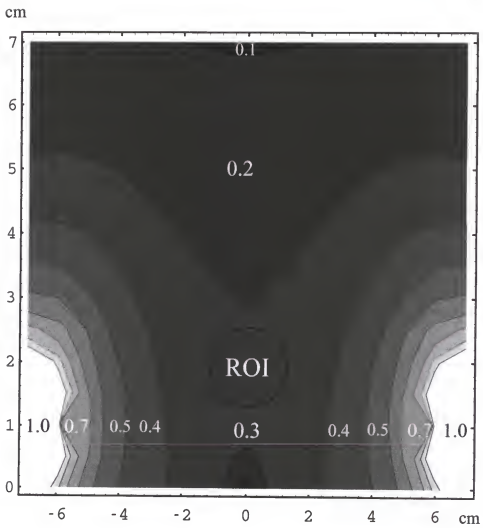


Figure 4-7. B_1 field mapping of a 14 cm x 20 cm transmit-only linear surface coil.

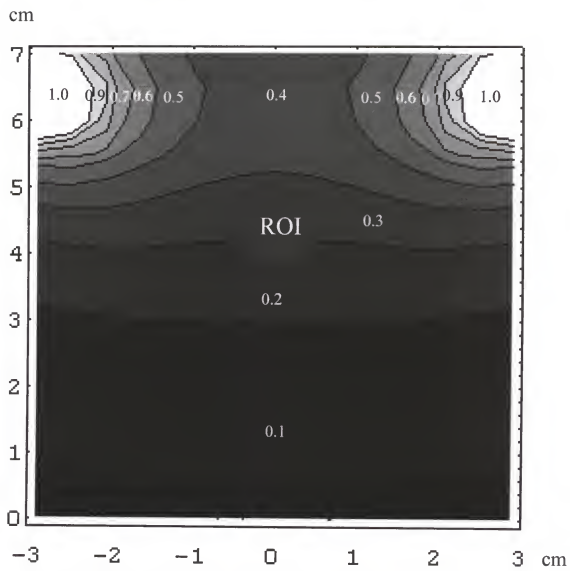


Figure 4-8. B_1 field mapping of a 10 cm x 6 cm receive-only linear surface coil.

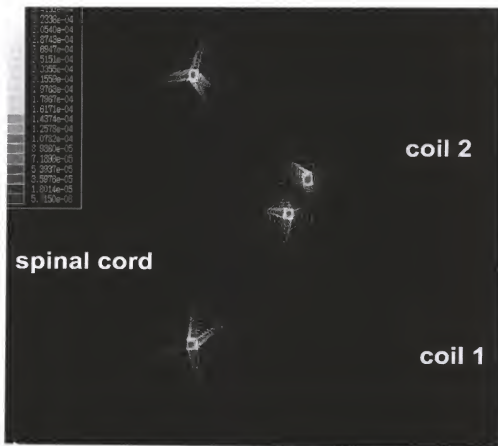


Figure 4-9. Cross sectional B₁ field mapping of a quadrature inductively coupled implanted coil.

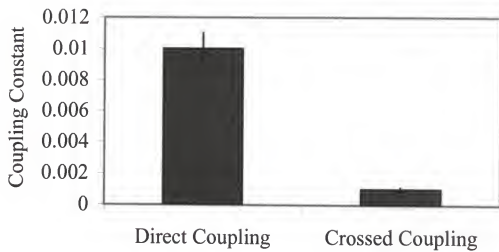


Figure 4-10. Comparison of the direct coupling and the crossed coupling constants of a quadrature implanted coil. The direct coupling is the coupling between coil 1 and coil 3 or between coil 2 and coil 4 and the crossed coupling is the coupling between coil 2 and coil 3 or between coil 1 and coil 4.

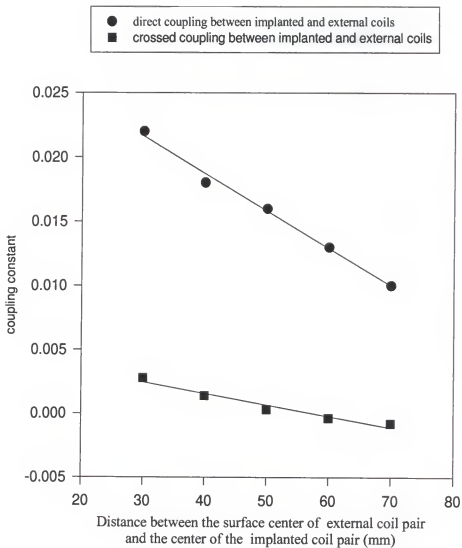


Figure 4-11. Direct and crossed coupling constants varied with distance.

Figure 4-12 and Table 4-3 indicate the SNR improvement for the linear surface coil by using the balanced matching circuit shown in Figure 2-7 over the balanced matching circuit shown in Figure 2-5. So the SNR from the linear surface coil using the balanced matching circuit was compared with the SNRs from other coil system.

Either with a light or a heavy loading, the quadrature implanted coil exhibited a significant increase in SNR relative to the surface coils and higher SNR than that of the linear implanted coil. Images were taken by the four coil system with a light loading, a 1 cm saline tube, whose center is 20 mm, 26 mm and 32 mm (20mm to 32 mm is the range of the distance from different spinal cord levels of a cat to its skin) from the surface center of the external coil pair and the SNR of the four coil systems are shown in Figure 4-13. Figure 4-14 shows the SNR comparison of the quadrature surface coil to the linear surface. The relative SNR comparison of the other three types of coil systems to the linear surface is shown in Tables 4-4. The images with a heavy loading, a “cat phantom”, taken by the four coil system are shown in Figure 4-15 and the SNR measured from the images are shown in Figure 4-16. Figure 4-17 shows the SNR comparison of the quadrature surface coil to the linear surface with the heavy loading. The relative SNR comparison to the linear surface coil and the comparison between the linear and implanted are showed in Tables 4-5. The quadrature-implanted coil exhibited a factor of 1.54 increase in SNR relative to the linear implanted coil, 3.05 to the quadrature surface coil and 5.68 to the linear surface coil. The improved SNR for the quadrature implanted coil, the linear implanted coil and the quadrature surface coil was observed as a dramatic improvement in the clarity of the images from the excised rat spinal cord, as shown in Figure 4-18.

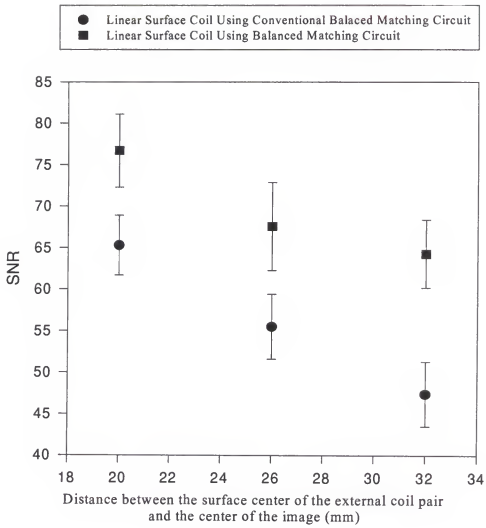


Figure 4-12. SNR comparison a coil with a conventional balanced matching circuit and a coil with a balanced matching circuit. The matching circuits are shown in Figure 2-5 and 2-7 and the coil is a linear surface coil. The error bars are the standard deviation of the SNR.

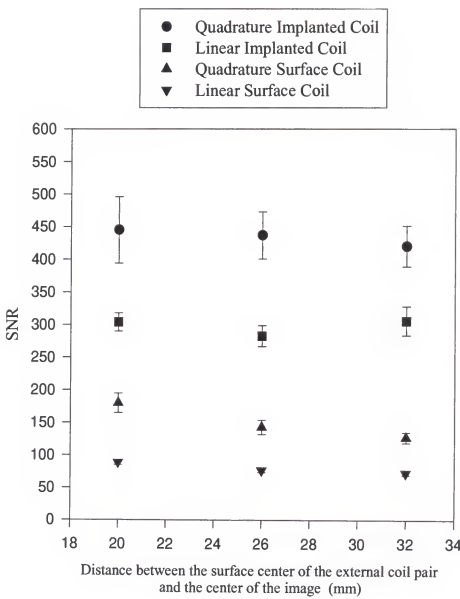


Figure 4-13. SNR (measured on a 1 cm tube phantom) comparison between the four coil systems. The error bars are the standard deviation of the SNR.

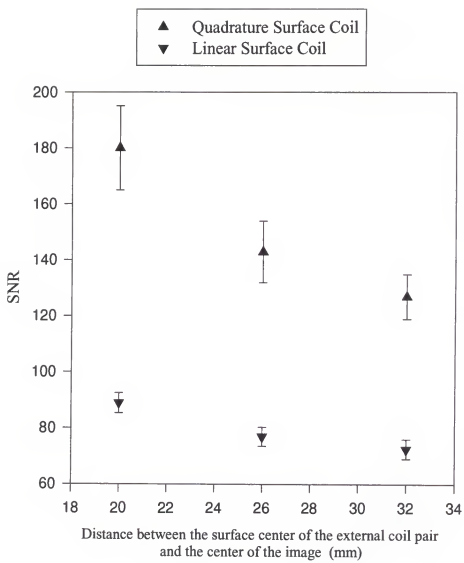


Figure 4-14. SNR (measured on a 1 cm tube phantom) comparison between the quadrature and linear surface coil systems. The error bars are the standard deviation of the SNR.

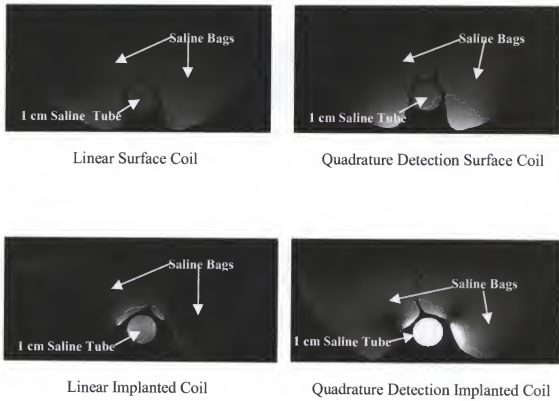


Figure 4-15. Images of the cat phantom taken with the four coil systems.

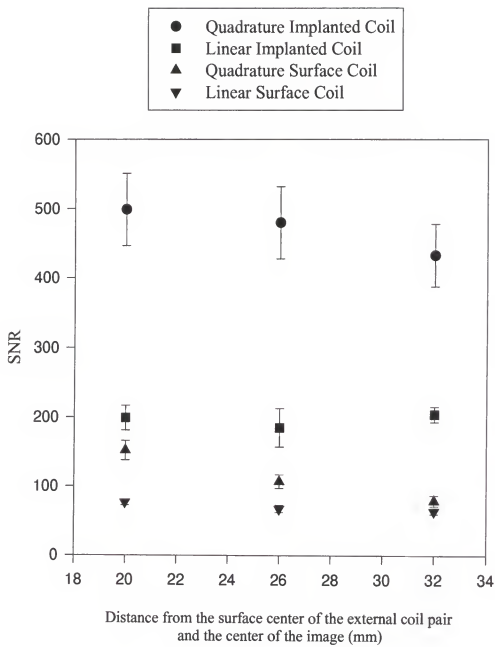


Figure 4-16. SNR (measured on a cat phantom) comparison between the four coil systems. The error bars are the standard deviation of the SNR.

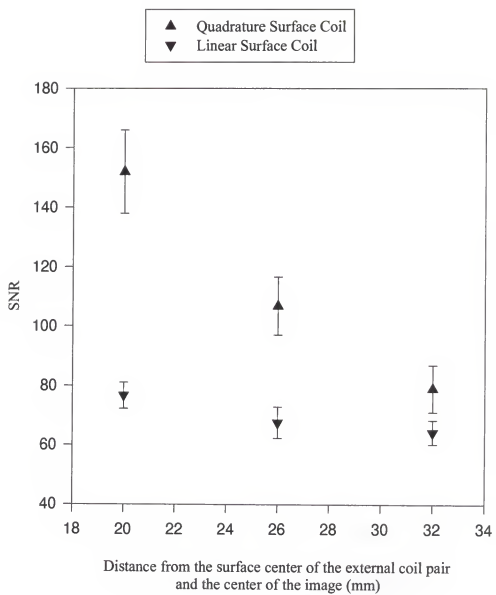
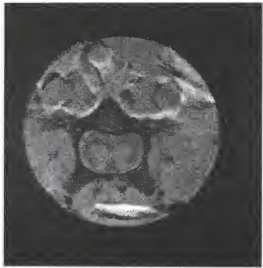
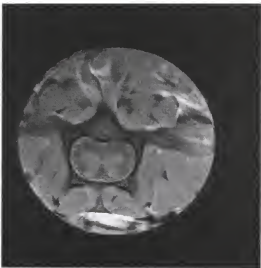


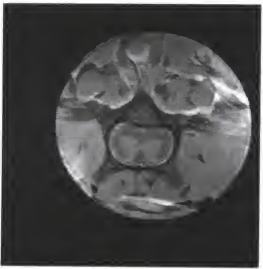
Figure 4-17. SNR (measured on the cat phantom) comparison between the quadrature and the linear surface coil systems. The error bars are the standard deviation of the SNR.



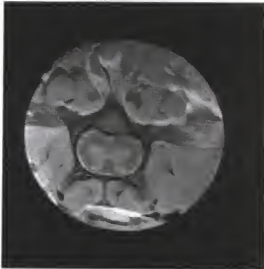
Linear Surface Coil



Quadrature Detection Surface Coil



Linear Implanted Coil



Quadrature Detection Implanted Coil

Figure 4-18. Comparison of excised rat spinal cord images taken with the four coil systems.

Table 4-3. Relative SNR comparison between a coil with a conventional balanced matching circuit and a coil with a balanced matching circuit. The circuits are shown in Figure 2-5 and Figure 2-7 respectively. The SNR was measured a cat phantom. The SNR of a coil with a conventional balanced matching circuit is normalized to be 1.

Distance *(mm)	20	26	32
Conventional Balanced Matching	1.0	1.0	1.0
Balanced Matching	1.1	1.2	1.3

Table 4-4. Relative SNR (measured on a 1 cm tube phantom) comparison between the four coil systems and the linear surface coil (whose SNR is normalized to be 1).

Distance* (mm)	20	26	32
Linear Surface Coil	1.00	1.00	1.00
Quadrature Surface Coil	2.02	1.86	1.75
Linear Implanted Coil	3.42	3.68	4.22
Quadrature Implanted Coil	5.00	5.68	5.75

Table 4-5. Relative SNR (measured on the cat phantom) comparison between the four coil systems and a linear surface coil (whose SNR is normalized to be 1).

Distance* (mm)	20	26	32
Linear Surface Coil	1.00	1.00	1.00
Quadrature Surface Coil	1.97	1.57	1.23
Linear Implanted Coil	2.58	2.72	3.19
Quadrature Implanted Coil	6.47	7.04	6.76

Note: * The distance is between the surface center of the external coil pair to the center of the image (the center of the 1 cm tube).

Discussion

In order to obtain the maximum filling factor possible, the ideal coil would be a cylindrical probe situated immediately around the spinal cord with a length slightly greater than that of the ROI. However, the severe space constraints and the possibility of nerve root damage within the spinal cord limit the practicality of this coil design in living subjects. Thus, it is more feasible to situate the coil on the dorsal surface of the spine. This reduces the chance for the nerve root damage while maintaining a field of view that is primarily limited to the spine.

Due to the low concentrations of biochemical compounds, it is important to optimize the sensitivity of NMR coils. The SNR observed during *in vivo* experiments may be improved by reducing losses associated with the electric fields generated by currents in ground loops and the associated resistive and radiative losses (Hoult, Lauterbur, 1979; Hoult, Richards, 1976; Murphy-Boesch, Koretsky, 1983). SNR is also improved when resonance frequency shifts of the coil are reduced. The resonance frequency shifts are due to movements of the patient or the animal under study, which modulates the free induction signals and results in a loss of signal coherence. Also a series capacitor inserted in the coil can reduce the electric losses in the sample and the frequency shift of the coil resonance frequency upon introduction of the sample or the movements of the animal under study. A balanced matching circuit shown in Figure 2-7 is used to optimize the linear surface coil for the SNR comparison. An implanted coil inductively coupled to a transmit-receive coil is a nearly perfectly balanced coil with respect to the sample (Murphy-Boesch, 1985), so only a conventional matching circuit shown in Figure 2-5 is required for implanted coils. The inductively coupled coils also

reduce radiative and resistive losses in the ground loops and the frequency shift of the coil resonance frequency due to the introduction of the sample or the movements of the animal under study.

The results of this study indicate that a quadrature inductively coupled implanted RF coil on the spine offers a significant improvement in SNR over both linear and quadrature surface coils. It also provides higher SNR than the inductively coupled linear implanted coils. The comparison with a linear implanted coil is important, because the linear implanted coil currently offers the best images of the spinal cord in experimental NMR systems (Wirth et al., 1993). The fact that the quadrature surface coil offers more than expected 1.4 improvement in SNR over the linear surface coils can be contributed to the small width of each loop in the quadrature pair (4 cm instead of 6 cm). Relative to the linear surface coil, the more rapid decrease in quadrature coil performance (see Figures 4-14 and 4-16) can also be contributed to the reason mentioned above. Since the field decreases more rapidly with the depth in a small coil than in a large coil and the field decreases more rapidly with the depth in a quadrature surface coil than in a linear surface coil. The performance of a linear implanted coil does not decrease with the depth in the small range, the separation between a cat different spinal cord levels to its skin. This is because the implanted coil dominated the performance and the coupling between the implanted coil and the external coil changes slightly with the depth. However, the performance of quadrature implanted coil decreases with the depth, which is due to the two reasons for the quadrature surface coil and to the coupling between the quadrature implanted coil pair and the external coil pair decreasing with the depth. The range of the depth (20 mm to 32 mm from the surface center of the external coil pair, i.e. 12.5 mm to

24.5 mm from a cat's skin) is chosen to match the range of the depth of a cat's spinal cord. In addition the penetration depth of the surface coils is about 30 mm (half of its diameter, 6 cm) and the transmitting power is maximized when the depth is increased to 38 mm.

Since the load increases the isolation between the external coil pair, the quadrature implanted coil tends to have higher SNR with the larger load. Having good isolation between the quadrature coil pair, especially the implanted quadrature coil pair is critical for the SNR improvement. If each of the implanted coil pair is resonant at the same frequency and is well isolated (no coupling) from the other coil only one peak will be observed.

Even the quadrature surface coil in this study provides decent SNR at the second lumbar spinal cord level (12.5 mm from a cat's skin), the quadrature implanted coil offers significantly greater SNR. In addition, our results (see Table 4-4 and Table 4-5) have shown that with implanted coils even greater relative performance gains can be realized at deeper levels of the spine (e.g., cervical, 20 mm from a cat's skin). Although the relative gain of the quadrature implanted coil over the linear implanted coil is less, the quadrature implanted coil still offers a greater SNR.

In addition, the small size of the implanted coil has the advantage of limiting the FOV to the spine. Hence, the aliasing of the signal from tissues outside of the coil onto the spinal cord portion of the image is much less of a problem than with large external coils. Thus, the FOV can be restricted to the spine without the aliasing problems. Also using the miniature components makes the surgery easier, since it does not require a large blunt dissection of the muscle from the spine. It also can help to minimize the

deformation and resulting inflammation of the adjacent musculature. Solder joints will not break easily either.

Conclusion

We are first to design an inductively coupled quadrature implanted coil and show that an inductively coupled quadrature implanted coil offers a high SNR. In the ROI (i.e., a cat spinal cord), the quadrature implanted coil exhibited a factor of 7.04 increase in SNR relative to the linear surface coil; a factor of 4.48 relative to the quadrature surface coil and a factor of 2.59 relative to the linear implanted coil. The improved SNR for an inductively coupled quadrature implanted coil is observed as a dramatic improvement in the clarity of the images of a rat's spinal cord.

The high SNR available with the inductively coupled implanted coils allows the acquisition of high resolution NMR images and opens up the possibility of measuring localized spectroscopy *in vivo*. The extra boost in SNR with the quadrature implanted coil can be particularly beneficial in certain types of experiments involving the spinal cord or other deep small structures. Studies of small structures such as fetal spinal cord transplants demand the maximum SNR possible be obtained to extract the most useful information. The increased image quality and reduced FOV will definitely help to more clearly identify the host cord anatomy as well as apposition to the graft. The improved SNR also makes it possible to acquire *in vivo* localized NMR spectra of the spinal cord in about 20 minutes. From the localized spectrum of the spinal cord, physiological data related to transplant survival and its effect on the host spinal cord could be acquired.

CHAPTER V CONCLUSION

Application of ^{31}P Implanted Coils in Rat Spinal Cord Injury and Repair

The optimized ^{31}P implanted coil system can be applied to the study of animals receiving contusion injury (graft controls) and contused animals receiving suspensions of E₁₄ fetal neural cells. This technology can be used to noninvasively detect metabolic differences between injured and non-injured animals and applied to follow metabolic improvements in transplanted animals. These methods provide relative measurements of ^{31}P levels associated with the different molecules of interest--ATP, PCr, and Pi. Fetal neural tissue successfully transplanted into an injured rat spinal cord may restore metabolic health to injured cord. This can be tested by monitoring the levels of phosphorous-containing metabolites in rat spinal cord after fetal neural tissue transplantation into a cord with previous contusion injury.

Our data also indicate that the comparisons of metabolite levels could be obtained in a relatively short time period because of the improved SNR available using the implanted RF coils described in this work. Since there was only a small change in the ^{31}P signal, longer acquisition can be considered for future studies of the sub-acute phase of SCI and for studies of fetal CNS transplants.

The relative levels of PCr, ATP, Pi, and PME can be determined relative to the level of phenylphosphonic acid in the reference. The reference can be placed on the

opposite side of the spinal cord with the same distance from the plane of the implanted coil as the cord is from that plane; this would provide a constant reference throughout the experiment. The comparisons of metabolite peak areas to the reference peak will show changes in metabolite levels over the course of the experiment.

Applications of Quadrature Inductively Coupled Implanted Coil in Cat Spinal Cord Injury and Repair

The design of inductively coupled quadrature implanted coils allows the coil to be positioned on the dorsal surface of the spine. As result, the implanted coils restrict the FOV in an image without folding signals outside the region of interest. More importantly the small size of these quadrature implanted coils generates a significant increase in SNR relative to optimized surface coil or even the linear implanted coil. The high SNR available with the inductively coupled quadrature implanted coil allows the acquisition of high quality MRI. In addition, NMR with the inductively coupled implanted coils has the capacity for repeated observations of individual subjects. Thus, MRI may eventually provide important long-term anatomical changes at multiple time points. Such anatomical data would allow for longitudinal comparison of various injury parameters, (e.g., lesion size or damaged axonal tracts) and thereby reduce the number of the required samples. In chronic injuries of the spinal cord, MRI could be used to determine the location and volume of the lesion cavity prior to grafting.

In addition to surgical planning and follow up, MRI may also allow for monitoring of progressive or unexpected pathology in the host spinal cord. MRI may also indicate the extent of demyelination in the host spinal cord rostral and caudal to the transplant or injury site (Wirth, 1992). In addition to the anatomical information obtained

through MRI, the metabolic environment of spinal cord injuries and transplants may be studied with the magnetic resonance spectroscopy (MRS). Although a number of studies have used MRS to observe the metabolic derangement following ischemia or traumatic injury to the brain (Vink et al., 1987), there is only one such report for spinal cord injury (Vink et al., 1989). The primary technical hurdle for MRS of spinal cord injuries is the relatively small volume of the spinal cord. In the cat, the upper lumbar cord is approximately 4 mm in diameter. Thus, a 1 cm segment of the cord has a volume of roughly 125 μ l. In contrast, NMR spectroscopy of brain regions is usually performed on volumes of several milliliters or more. This limitation may eventually be overcome by with higher field magnets and /or high SNR RF coils. The extra boost in SNR with the quadrature implanted coil opens up the possibility of measuring spectra *in vivo* localized in a cat spinal cord region. MRS may also aid in determining transplant survival. Thus, localized spectroscopy of a transplant site in which a majority of the host gray matter is previously eliminated can establish the presence of a viable graft by detecting an n-acetyl aspartate (NAA) signal (Wirth, 1992). NMR spectroscopy offers the potential for direct observation of transplant metabolism in an essentially unperturbed setting.

MRI and MRS, individually and collectively, hold great promise for evaluating the success of fetal spinal cord transplants in living subjects. Within certain spatial and contrast resolution limits, MRI already has a high predictive value for determining graft survival at subacute and chronic postgrafting intervals. This diagnostic reliability will be further enhanced through optimized RF coils. Thus, these studies have demonstrated the value of MRI and MRS with high SNR quadrature implanted coils in relation to the experimental spinal cord transplantation and have provided a framework that should

enable the clinician-investigator to follow the progress of transplanted neural tissue in the injured human spinal cord.

Future of Implanted Coil Development

First the inductively coupled quadrature implanted ^1H coil can be extended to applications on other organs/tissues (e.g., liver, heart, kidney etc.). However, the geometry of the quadrature implanted coil needs to be optimized for the structure under study.

^{31}P NMR spectra can provide potentially very useful information on changes in metabolite concentration, pathology and neural tissue development of spinal cord. It would be very useful to have a $^1\text{H}/^{31}\text{P}$ double tuned inductively coupled linear implanted coil system or even a $^1\text{H}/^{31}\text{P}$ double tuned inductively coupled quadrature implanted coil system. The miniature components enhance the possibility to build such coil systems and implant them on a cat spinal column. However, more precise calculation and modeling of the coil systems need to be done.

The inductively couple quadrature implanted coil system may also be extended to make inductively coupled phase arrayed implanted coils or even inductively coupled phase arrayed implanted $^{31}\text{P}/^1\text{H}$ doubled tuned coils. Special attention should be paid to the coupling of the coils when they are resonant at different (^{31}P or ^1H) frequencies.

APPENDIX

According to Biot-Savart law, the field of a half-saddle shape (arbitrary subtend angle) coil, shown as Figure 2-2,

$$\vec{B} = \frac{\mu I}{4\pi} \oint \frac{d\vec{l} \times \vec{r}}{r^3} \quad [A-1]$$

Let $\frac{\mu I}{4\pi}$ to be one unit and then we obtain

$$\vec{B} = \oint \frac{1}{r^3} d\vec{l} \times \vec{r} = \int_{(1)} \frac{1}{r^3} d\vec{l} \times \vec{r} + \int_{(2)} \frac{1}{r^3} d\vec{l} \times \vec{r} + \int_{(3)} \frac{1}{r^3} d\vec{l} \times \vec{r} + \int_{(4)} \frac{1}{r^3} d\vec{l} \times \vec{r} \quad [A-2]$$

where

$$(1) \quad \int_{-L}^L \frac{d\vec{l} \times \vec{r}}{r^3} = \int_{-L}^L d\vec{l} \times \vec{r} / r^3$$

$$= \int_{-L}^L \begin{vmatrix} \vec{i} & \vec{j} & \vec{k} \\ 0 & 0 & dl \\ x + R \sin \varphi_1 & y - R \cos \varphi_1 & z - l \end{vmatrix} / [(x + R \sin \varphi_1)^2 + (y - R \cos \varphi_1)^2 + (z - l)^2]^{3/2} \quad [A-3]$$

$$= \int_{-L}^L \frac{-(y - R \cos \varphi_1) d\vec{i} + (x + R \sin \varphi_1) d\vec{j}}{[(x + R \sin \varphi_1)^2 + (y - R \cos \varphi_1)^2 + (z - l)^2]^{3/2}}$$

$$(2) \quad \int_{-\varphi_1}^{\varphi_1} \frac{d\vec{l} \times \vec{r}}{r^3} = \int_{-\varphi_1}^{\varphi_1} d\vec{l} \times \vec{r} / r^3$$

$$= \int_{-\varphi_1}^{\varphi_1} \begin{vmatrix} \vec{i} & \vec{j} & \vec{k} \\ R \cos \varphi d\varphi & R \sin \varphi d\varphi & 0 \\ x - R \sin \varphi & y - R \cos \varphi & z - L \end{vmatrix} / [(x - R \sin \varphi)^2 + (y - R \cos \varphi)^2 + (z - L)^2]^{3/2} \quad [A-4]$$

$$= \int_{-\varphi_1}^{\varphi_1} \frac{-(z - L) R \sin \varphi d\varphi \vec{i} - (z - L) R \cos \varphi d\varphi \vec{j} + (y R \cos \varphi + x R \sin \varphi - R^2) d\varphi \vec{k}}{[(x - R \sin \varphi)^2 + (y - R \cos \varphi)^2 + (z - L)^2]^{3/2}}$$

$$\begin{aligned}
 \int d\vec{l} \cdot \vec{x} \cdot \vec{r} / r^3 &= \int_{-L}^{+L} d\vec{l} \cdot \vec{x} \cdot \vec{r} / r^3 \\
 (3) \quad &= \int_{-L}^{+L} \begin{vmatrix} \vec{i} & \vec{j} & \vec{k} \\ 0 & 0 & dl \\ x - R \sin \varphi_1 & y - R \cos \varphi_1 & z + l \end{vmatrix} / [(x - R \sin \varphi_1)^2 + (y - R \cos \varphi_1)^2 + (z + l)^2]^{3/2} \\
 &= \int_{-L}^{+L} \frac{-(y - R \cos \varphi_1)dl\vec{i} + (x - R \sin \varphi_1)dl\vec{j}}{[(x - R \sin \varphi_1)^2 + (y - R \cos \varphi_1)^2 + (z + l)^2]^{3/2}} \\
 &= -\int_{-L}^{+L} \frac{-(y - R \cos \varphi_1)dl\vec{i} + (x - R \sin \varphi_1)dl\vec{j}}{[(x - R \sin \varphi_1)^2 + (y - R \cos \varphi_1)^2 + (z + l)^2]^{3/2}}
 \end{aligned} \tag{A-5}$$

$$\begin{aligned}
 \int d\vec{l} \cdot \vec{x} \cdot \vec{r} / r^3 &= \int_{-\varphi_1}^{\varphi_1} d\vec{l} \cdot \vec{x} \cdot \vec{r} / r^3 \\
 (4) \quad &= \int_{-\varphi_1}^{\varphi_1} \begin{vmatrix} \vec{i} & \vec{j} & \vec{k} \\ R \cos \varphi d\varphi & R \sin \varphi d\varphi & 0 \\ x - R \sin \varphi & y - R \cos \varphi & z - l \end{vmatrix} / [(x - R \sin \varphi)^2 + (y - R \cos \varphi)^2 + (z + L)^2]^{3/2} \\
 &= \int_{-\varphi_1}^{\varphi_1} \frac{-(z + L)R \sin \varphi d\varphi \vec{i} - (z + L)R \cos \varphi d\varphi \vec{j} + (yR \cos \varphi + xR \sin \varphi - R^2)d\varphi \vec{k}}{[(x - R \sin \varphi)^2 + (y - R \cos \varphi)^2 + (z + L)^2]^{3/2}} \\
 &= -\int_{-\varphi_1}^{\varphi_1} \frac{-(z + L)R \sin \varphi d\varphi \vec{i} - (z + L)R \cos \varphi d\varphi \vec{j} + (yR \cos \varphi + xR \sin \varphi - R^2)d\varphi \vec{k}}{[(x - R \sin \varphi)^2 + (y - R \cos \varphi)^2 + (z + L)^2]^{3/2}}
 \end{aligned} \tag{A-6}$$

$$\begin{aligned}
 \vec{B} = & \\
 & + \int_{-L}^{L} \frac{-(y - R \cos \varphi_1)dl}{-L[(x + R \sin \varphi_1)^2 + (y - R \cos \varphi_1)^2 + (z - l)^2]^{3/2}} \vec{i} + \int_{-L}^{L} \frac{(y - R \cos \varphi_1)dl}{-L[(x - R \sin \varphi_1)^2 + (y - R \cos \varphi_1)^2 + (z - l)^2]^{3/2}} \vec{i} \\
 & + \int_{-\varphi_1}^{\varphi_1} \frac{-(z - L)R \sin \varphi d\varphi}{-\varphi_1[(x - R \sin \varphi)^2 + (y - R \cos \varphi)^2 + (z - L)^2]^{3/2}} \vec{i} + \int_{-\varphi_1}^{\varphi_1} \frac{(z + L)R \sin \varphi d\varphi}{-\varphi_1[(x - R \sin \varphi)^2 + (y - R \cos \varphi)^2 + (z + L)^2]^{3/2}} \vec{i} \\
 & + \int_{-L}^{L} \frac{(x + R \sin \varphi_1)dl}{-L[(x + R \sin \varphi_1)^2 + (y - R \cos \varphi_1)^2 + (z - l)^2]^{3/2}} \vec{j} + \int_{-L}^{L} \frac{-(x - R \sin \varphi_1)dl}{-L[(x - R \sin \varphi_1)^2 + (y - R \cos \varphi_1)^2 + (z + l)^2]^{3/2}} \vec{j} \\
 & + \int_{-\varphi_1}^{\varphi_1} \frac{-(z - L)R \cos \varphi d\varphi}{-\varphi_1[(x - R \sin \varphi)^2 + (y - R \cos \varphi)^2 + (z - L)^2]^{3/2}} \vec{j} + \int_{-\varphi_1}^{\varphi_1} \frac{(z + L)R \cos \varphi d\varphi}{-\varphi_1[(x - R \sin \varphi)^2 + (y - R \cos \varphi)^2 + (z + L)^2]^{3/2}} \vec{j} \\
 & + \int_{-\varphi_1}^{\varphi_1} \frac{(Rycos\varphi + Rxsin\varphi - R^2)d\varphi}{-\varphi_1[(x - R \sin \varphi)^2 + (y - R \cos \varphi)^2 + (z - L)^2]^{3/2}} \vec{k} + \int_{-\varphi_1}^{\varphi_1} \frac{-(Rycos\varphi + Rxsin\varphi - R^2)d\varphi}{-\varphi_1[(x - R \sin \varphi)^2 + (y - R \cos \varphi)^2 + (z + L)^2]^{3/2}} \vec{k}
 \end{aligned} \tag{A-7}$$

In the x-y plane, where z=0, the RF field is

$$B_z = 0$$

$$B_x = \int_{-L}^L \frac{(y - R \cos \varphi_1) dl}{[(x - R \sin \varphi_1)^2 + (y - R \cos \varphi_1)^2 + l^2]^{3/2}} - \int_{-L}^L \frac{(y - R \cos \varphi_1) dl}{[(x + R \sin \varphi_1)^2 + (y - R \cos \varphi_1)^2 + l^2]^{3/2}} \\ + \int_{-\varphi_1}^{\varphi_1} \frac{2LR \sin \varphi d\varphi}{[(x + R \sin \varphi)^2 + (y - R \cos \varphi)^2 + L^2]^{3/2}}$$

[A-8]

$$B_y = \int_{-L}^L \frac{(x + R \cos \varphi_1) dl}{[(x + R \sin \varphi_1)^2 + (y - R \cos \varphi_1)^2 + l^2]^{3/2}} - \int_{-L}^L \frac{(x - R \cos \varphi_1) dl}{[(x - R \sin \varphi_1)^2 + (y - R \cos \varphi_1)^2 + l^2]^{3/2}} \\ + \int_{-\varphi_1}^{\varphi_1} \frac{2LR \cos \varphi d\varphi}{[(x - R \sin \varphi)^2 + (y - R \cos \varphi)^2 + L^2]^{3/2}}$$

[A-9]

$$\text{Since } \int \frac{dx}{(a + x^2)^{3/2}} = \frac{x}{a\sqrt{a + x^2}},$$

$$B_x = \int_{-L}^L \frac{(y - R \cos \varphi_1) dl}{[(x - R \sin \varphi_1)^2 + (y - R \cos \varphi_1)^2 + l^2]^{3/2}} \\ = \frac{(y - R \cos \varphi_1) l}{[(x - R \sin \varphi_1)^2 + (y - R \cos \varphi_1)^2] \sqrt{[(x - R \sin \varphi_1)^2 + (y - R \cos \varphi_1)^2 + l^2]}} \Big|_{-L}^L$$

$$\text{Since } \int \frac{dx}{\sqrt{(a + bx + cx^2)^3}} = \frac{2(2cx + b)}{(4ac - b^2)\sqrt{a + bx + cx^2}} ;$$

$$\int \frac{d\varphi}{\sqrt{a + b \cos \varphi + c \sin \varphi}} = 2 \int \frac{d\psi}{\sqrt{a - p + 2p \cos^2 \psi}} ; \\ [\varphi = 2\psi + \alpha, \tan \alpha = \frac{c}{b}, p = \sqrt{b^2 + c^2}]$$

$$\int \frac{dx}{\Delta^3} = \frac{1}{k^2} E(x, k) - \frac{k^2}{k^2} \frac{\sin x \cos x}{\Delta} ;$$

$$\int \frac{\sin^2 x dx}{\Delta^3} = \frac{1}{k^2} \frac{1}{k^2} E(x, k) - \frac{1}{k^2} R(x, k) - \frac{1}{k^2} \frac{\sin x \cos x}{\Delta} .$$

$$\begin{aligned}
& \int_{-\varphi_1}^{\varphi_1} \frac{2LR \sin \varphi d\varphi}{[(x - R \sin \varphi)^2 + (y - R \cos \varphi)^2 + L^2]^{3/2}} \\
&= \int_{-\varphi_1}^{\varphi_1} \frac{2LR \sin \varphi d\varphi}{[x^2 + y^2 + L^2 + R^2 - 2Rx \sin \varphi - 2Ry \cos \varphi]^{3/2}} \\
&= \frac{\varphi_1 - \alpha}{2} \int_{-\varphi_1 - \alpha}^{\varphi_1 - \alpha} \frac{2LR \sin(2\psi + \alpha) d\psi}{[A - P + 2P \cos^2 \psi]^{3/2}} \\
&= \frac{\varphi_1 - \alpha}{2} \int_{-\varphi_1 - \alpha}^{\varphi_1 - \alpha} \frac{2LR (\sin 2\psi \cos \alpha + \cos 2\psi \sin \alpha) d\psi}{[A - P + 2P(1 - \sin^2 \psi)]^{3/2}} \\
&= \frac{\varphi_1 - \alpha}{2} \int_{-\varphi_1 - \alpha}^{\varphi_1 - \alpha} \frac{2LR [2 \sin \psi \cos \psi \cos \alpha + (1 - 2 \sin^2 \psi) \sin \alpha] d\psi}{\sqrt{A + P} [1 - \frac{2P}{A + P} \sin^2 \psi]^{3/2}} \\
&= \frac{2LR}{\sqrt{A + P}} \left\{ 2 \cos \alpha \int_{-\varphi_1 - \alpha}^{\varphi_1 - \alpha} \frac{\sin \psi \cos \psi d\psi}{[1 - k^2 \sin^2 \psi]^{3/2}} + \sin \alpha \int_{-\varphi_1 - \alpha}^{\varphi_1 - \alpha} \frac{(1 - 2 \sin^2 \psi) d\psi}{[1 - k^2 \sin^2 \psi]^{3/2}} \right\} \\
&= \frac{2LR}{\sqrt{A + P}} \left\{ 2 \cos \alpha \int_{-\varphi_1 - \alpha}^{\varphi_1 - \alpha} \frac{\sin \psi \cos \psi d\psi}{\Delta^3} + \sin \alpha \int_{-\varphi_1 - \alpha}^{\varphi_1 - \alpha} \frac{(1 - 2 \sin^2 \psi) d\psi}{\Delta^3} \right\} \\
&= \frac{2LR}{\sqrt{A + P}} \left\{ 2 \cos \alpha \frac{1}{k^2 \Delta} + \sin \alpha \left[\frac{1}{k^2} E(\psi, k) - \frac{k^2}{k^2} \frac{\sin \psi \cos \psi}{\Delta} - 2 \left(\frac{1}{k^2 k^2} E(\psi, k) - \frac{1}{k^2} F(\psi, k) - \frac{\sin \psi \cos \psi}{k^2 \Delta} \right) \right] \right\} \Big|_{-\varphi_1 - \alpha}^{\varphi_1 - \alpha} \\
&= \frac{2LR}{\sqrt{A + P}} \left\{ 2 \cos \alpha \frac{1}{k^2 \Delta} + \sin \alpha \left[\frac{1}{k^2} \left(1 - \frac{2}{k^2} \right) E(\psi, k) - \frac{1}{k^2} (2 + k^2) \frac{\sin \psi \cos \psi}{\Delta} + \frac{2}{k^2} F(\psi, k) \right] \right\} \Big|_{-\varphi_1 - \alpha}^{\varphi_1 - \alpha} \\
&\quad [A-10]
\end{aligned}$$

Where

$$A = x^2 + y^2 + L^2 + R^2, \tan \alpha = x/y, \psi = \frac{\varphi - \alpha}{2}; P = 2R\sqrt{x^2 + y^2} \geq 0;$$

$$k = \frac{2P}{A + P}; k' = \sqrt{1 - k^2}; \Delta = \sqrt{1 - k^2 \sin^2 \psi}.$$

Similarly

$$\begin{aligned} & \int_{-\varphi_1}^{\varphi_1} \frac{2LR \cos \varphi d\varphi}{[(x + R \sin \varphi)^2 + (y - R \cos \varphi)^2 + L^2]^{3/2}} \\ &= \frac{2LR}{\sqrt{A+P}} \int_{-\frac{\varphi_1 - \alpha}{2}}^{\frac{\varphi_1 - \alpha}{2}} \frac{\cos(2\psi + \alpha) d\psi}{\Delta^3} \\ &= \frac{2LR}{\sqrt{A+P}} \int_{-\frac{\varphi_1 - \alpha}{2}}^{\frac{\varphi_1 - \alpha}{2}} \frac{(\cos 2\psi \cos \alpha - \sin 2\psi \sin \alpha) d\psi}{\Delta^3} \\ &= \frac{2LR}{\sqrt{A+P}} \left\{ \cos \alpha \int_{-\frac{\varphi_1 - \alpha}{2}}^{\frac{\varphi_1 - \alpha}{2}} \frac{1 - 2 \sin^2 \psi d\psi}{\Delta^3} - 2 \sin \alpha \int_{-\frac{\varphi_1 - \alpha}{2}}^{\frac{\varphi_1 - \alpha}{2}} \frac{\sin \psi \cos \psi d\psi}{\Delta^3} \right\} \\ &= \frac{2LR}{\sqrt{A+P}} \left\{ \cos \alpha \left[\frac{1}{k^2} \left(1 - \frac{2}{k^2} \right) E(\psi, k) - \frac{1}{k^2} (2 + k^2) \frac{\sin \psi \cos \psi}{\Delta} + \frac{2}{k^2} F(\psi, k) \right] - \frac{2 \sin \alpha}{k^2 \Delta} \right\} \end{aligned}$$

[A-11]

So we have

$$\begin{aligned}
 B_x = & \\
 & 2L \left\{ \frac{(y - R \cos \varphi_1)}{[(x - R \sin \varphi_1)^2 + (y - R \cos \varphi_1)^2] \sqrt{(x - R \sin \varphi_1)^2 + (y - R \cos \varphi_1)^2 + L^2}} \right. \\
 & - \frac{(y - R \cos \varphi_1)}{[(x + R \sin \varphi_1)^2 + (y - R \cos \varphi_1)^2] \sqrt{(x + R \sin \varphi_1)^2 + (y - R \cos \varphi_1)^2 + L^2}} \} \\
 & + \frac{2LR}{\sqrt{A+P}} \left\{ 2 \cos \alpha \frac{1}{k^2 \Delta} + \sin \alpha \left[\frac{1}{k^2} \left(1 - \frac{2}{k^2} \right) E(\psi, k) - \frac{1}{k^2} (2+k^2) \frac{\sin \psi \cos \psi}{\Delta} + \frac{2}{k^2} F(\psi, k) \right] \right\} \Big|_{-\frac{\varphi_1 - \alpha}{2}}^{+\frac{\varphi_1 - \alpha}{2}}
 \end{aligned}$$

[A-12]

$$\begin{aligned}
 B_y = & \\
 & 2L \left\{ \frac{(x - R \cos \varphi_1)}{[(x - R \sin \varphi_1)^2 + (y - R \cos \varphi_1)^2] \sqrt{(x - R \sin \varphi_1)^2 + (y - R \cos \varphi_1)^2 + L^2}} \right. \\
 & - \frac{(x + R \cos \varphi_1)}{[(x + R \sin \varphi_1)^2 + (y - R \cos \varphi_1)^2] \sqrt{(x + R \sin \varphi_1)^2 + (y - R \cos \varphi_1)^2 + L^2}} \} \\
 & + \frac{2LR}{\sqrt{A+P}} \left\{ \cos \alpha \left[\frac{1}{k^2} \left(1 - \frac{2}{k^2} \right) E(\psi, k) - \frac{1}{k^2} (2+k^2) \frac{\sin \psi \cos \psi}{\Delta} + \frac{2}{k^2} F(\psi, k) \right] - \frac{2 \sin \alpha}{k^2 \Delta} \right\} \Big|_{-\frac{\varphi_1 - \alpha}{2}}^{+\frac{\varphi_1 - \alpha}{2}}
 \end{aligned}$$

[A-13]

REFERENCES

- Ackerman J.J.H., Grove T.H., Wong G.G., Gadian D.G., Radda G.K. (1980) Mapping of metabolites in whole animals by ^{31}P NMR using surface coils. *Nature* 283:167-170.
- Adriany G., Gruetter R. (1997) A half-volume coil for efficient proton decoupling in humans at 4 Tesla. *J.Magn.Reson.* 125:178
- Akino M., O'Donnell, J.M., Robitaille, P.M., Stokes B.T. (1997) Phosphorus-31 magnetic resonance spectroscopy studies of pig spinal cord injury. Myelin changes, intracellular pH, and bioenergetics. *Invest.Radiol.* 32:382-388
- Arnder L.L., Shattuck M.D., Black R.D. (1996) Signal-to-noise ratio comparison between surface coils and implanted coils. *Magn.Reson.Med.* 35:733-733.
- Arnder L.L., Zhou X., Cofer G.P., Hedlund L.W., Johnson G.A. (1994) Magnetic resonance microscopy of the rat carotid artery at 300 MHz. *Invest.Radiol.* 29:822-826.
- Bendall M.R., Connelly A., McKendry J.M. (1986) Elimination of coupling between cylindrical transmitting coils and surface-receive coils for *in vivo* NMR. *Magn.Reson.Med.* 3:157-163.
- Bendall M.R., McKendry J.M., Cresshull I.D., Ordidge R.J. (1984) Active detune switch for complete sensitive-volume localization in *in vivo* spectroscopy using multiple RF coils and depth pulses. *J.Magn.Reson.* 60:473-478.
- Bendall M.R., Pegg D.T. (1985) Theoretical description of depth pulse sequences, on and off resonance, including improvements and extensions theory. *Magn.Reson.Med.* 2:91-113.
- Bottomley P.A. (1987) Spatial localization in NMR spectroscopy *in vivo*. *Ann.N.Y.Acad.Sci.* 508:333-348.
- Chen C.N., Hoult D.I. (1989) Signal and noise. In: Biomedical magnetic resonance technology. New York: Adam Hilger, pp. 118.
- Chen C.N., Hoult D.I. (1993) The visualization of RF probe electric fields. *Magn.Reson.Med.* 29:386-390.

- Chen C.N., Sank V.J., Hoult D.I. (1983) Quadrature detection coils--A further $\sqrt{2}$ improvement in sensitivity. *J.Mag.Reson.* 54:324-327.
- Chen W. (1992) The antisense coaxial surface-coil probe, an improved method for coil-to-coil electromagnetic decoupling of coaxial surface coils. *J.Mag.Reson.* 238-258.
- Crowley M.G., Elelhoch J.L., Ackerman J.J.H. (1985) The surface-coil NMR receiver in the presence of homogeneous B_1 excitation. *J.Magn.Reson.* 64:20-31.
- De Graaf R.A., Luo Y., Terpstra M., Merkle H., Garwood M. (1995) A new localization method using an adiabatic pulse, BIR-4. *J.Magn.Reson.* 106:245-252.
- Decorps M., Blondet P., Reutenuer H., Albrand J.P., Remy C. (1985) An inductively coupled, series-tuned NMR probe. *J.Magn.Reson.* 65:100-109.
- Edelstein W.A., Glover G.H., Hardy C.J., Redington R.W. (1986) The intrinsic signal-to-noise ratio in NMR imaging. *Magn.Reson.Med.* 3:604-618.
- Faden A.I., Vink R., McIntosh T.K. (1989) Thyrotropin-releasing hormone and central nervous system trauma. *Ann.N.Y.Acad.Sci.* 553:380-384.
- Faden A.I., Yum S.W., Lemke M., Vink R. (1990) Effects of TRH-analog treatment on tissue cations, phospholipids and energy metabolism after spinal cord injury. *J.Pharmacol.Exp.Ther.* 255:608-614.
- Farmer T.H.R., Cofer G.P., Johnson G.A. (1990) Maximizing contrast to noise with inductively coupled implanted coils. *Invest.Radiol.* 25:552-558.
- Farmer T.H.R., Johnson G.A., Cofer G.P., Maronpot R.R., Dixon D., Hedlund L.W. (1989) Implanted coil MR microscopy of renal pathology. *Magn.Reson.Med.* 10:310-323.
- Fitzsimmons J.R., Beck B.L. (1992) The application of quadrature technology to quasi-volume geometries. *Proceedings Soc.Magn.Reson.Med.*, 11th Annual Meeting 977-977.(Abstract)
- Fitzsimmons J.R., Beck B.L., Brooker H.R. (1993) Double resonant quadrature birdcage. *Magn.Reson.Med.* 30:107-114.
- Fitzsimmons J.R., Brooker H.R., Beck B. (1989) A comparison of double-tuned surface coils. *Magn.Reson.Med.* 10:302-309.
- Fitzsimmons J.R., Brooker H.R., Beck B. (1987) A transformer-coupled double-resonant probe for NMR imaging and spectroscopy. *Magn.Reson.Med.* 5:471-477.

- Ford J.C., Hackney D.B., Joseph P.M., Phelan M., Alsop D.C., Tabor S.L., Hand C.M., Markowitz R.S., Black P. (1994) A method for *in vivo* high resolution MRI of rat spinal cord injury. *Magn.Reson.Med.* 31:218-223.
- Frahm J., Michaelis T., Merboldt K.D., Hanicke W., Gyngell M.L., Chien D., Bruhn H. (1989) Localized NMR spectroscopy *in vivo*. Progress and problems. *NMR.Biomed.* 2:188-195.
- Francisz W., Jesmanowicz A., Hyde J.S. (1986) Inductive (flux linkage) coupling to local coils in magnetic resonance imaging and spectroscopy. *J.Magn.Reson.* 66:135-143.
- Gadian D.G., Robinson F.N.H. (1979) Radiofrequency losses in NMR experiments on electrically conducting samples. *J.Magn.Reson.* 34:449-455.
- Gonzalez G. (1997) Microwave transistor amplifiers analysis and design. Upper Saddle River, New Jersey: Prentice Hall, pp. 15.
- Gradshteyn I.S., Ryzhik I.M. (1980) Table of integrals, series, and products. New York: Academic Press, pp. 83-164.
- Haase A. (1984a) A new method for the decoupling of multiple-coil NMR probes. *J.Magn.Reson.* 61:130-136.
- Haase A., Hanicke W., Frahm J. (1984b) The influence of experimental parameters in surface-coil NMR. *J.Magn.Reson.* 56:401-412.
- Harman R.R., Butson P.C., Hall AS, Young I.R. (1988) Some observations of the design of RF coils for human internal use. *Magn.Reson.Med.* 6:49-62.
- Harris R.K. (1983) Nuclear magnetic resonance spectroscopy. London: Pitman Books Limited, pp. 11.
- Hida K., Kwee L.L., Nakada T. (1993) *In vivo* ^1H and ^{31}P NMR spectroscopy of the developing rat brain. *Magn.Reson.Med.* 23:31-36.
- Hollett M.D., Cofer G.P., Johnson G.A. (1987) In situ magnetic resonance microscopy. *Invest.Radiol.* 22:965-968.
- Hoult D.I. (1984) NMR imaging techniques. *Br.Med.Bull.* 40:132-138.
- Hoult D.I., Busby S.J., Gadian D.G., Radda G.K., Richards R.E., Seeley P.J. (1974) Observation of tissue metabolites using ^{31}P nuclear magnetic resonance. *Nature* 252:285-287.
- Hoult D.I., Chen C.N., Sank V.J. (1984) Quadrature detection in the laboratory frame. *Magn.Reson.Med.* 1:339-353.

- Hoult D.I., Lauterbur P.C. (1979) The sensitivity of the zeugmatographic experiemnt involving human samples. *J.Magn.Reson.* 34:425-433.
- Hoult D.I., Richards R.E. (1976) The signal-to-noise ratio of the nuclear magnetic resonance experiment. *J.Magn.Reson.* 24:71-85.
- Hyde J.S., Jesmanowicz A., Grist T.M., Froncisz W., Kneeland J.B. (1987) Quadrature detection surface coils. *Magn.Reson.Med.* 4:179-184.
- Hyde J.S., Rilling R.J., Jesmanowicz A. (1990) Passive decoupling of surface coils by pole insertion. *J.Magn.Reson.* 89:485-495.
- Kantor H.L., Briggs R.W., Balaban R.S. (1984) *In vivo* ^{31}P nuclear magnetic resonance measurements in canine heart using a catheter-coil. *Circ.Res.* 55:261-266.
- Koretsky A.P., Wang S., Murphy-Boesch J., Klein M.P., James T.L., Weiner M.W. (1983) ^{31}P NMR spectroscopy of rat organs, *in situ*, using chronically implanted radiofrequency coils. *Proc.Natl.Acad.Sci.U.S.A.* 80:7491-7495.
- Ludeke K.M., Roschmann P., Tischler R. (1985) Susceptibility artefacts in NMR imaging. *Magn.Reson.Imaging* 3:329-343.
- Morikawa S., Inubushi T., Kito K., Amano S (1995) Long-term observation of *in vivo* ^{31}P NMR spectra in carbon tetrachloride-intoxicated rabbit liver using implanted wireless surface coil. *NMR.Biomed.* 8:3-8.
- Murphy-Boesch J. (1985) Sensitivity improvement via coil and probe design. *Biomed.Magn.Reson.* 47-61.
- Murphy-Boesch J., Koretsky A.P. (1983) An *in vivo* NMR probe circuit for improved sensitivity. *J.Magn.Reson.* 54:1983-1983.
- Nagel T.L., Alderman D.W., Schoenborn R.R., Hendrickson M., Shelby J., Saffle J., Schweizer M.P. (1990) The slotted crossover surface coil: a detector for *in vivo* NMR of skin. *Magn.Reson.Med.* 16:252-268.
- Nakada T., Kwee I.L., Miyazaki T., Iriguchi N., Maki T. (1987) ^{31}P NMR spectroscopy of the stomach by zig-zag coil. *Magn.Reson.Med.* 5:449-455.
- Nicolay K., Aue W.P., Seelig J., van Echteld C.J., Ruigrok T.J., de Kruijff B. (1987) Effects of the anti-cancer drug adriamycin on the energy metabolism of rat heart as measured by *in vivo* ^{31}P -NMR and implications for adriamycin-induced cardiotoxicity. *Biochim.Biophys.Acta* 929:5-13.
- O'Donnell J.M., Akino M., Zhu H., Stokes B.T. (1996) Phosphorus-31 nuclear magnetic resonance spectroscopy of the spinal cord in the pig, rat, and rabbit. *Invest.Radiol.* 31:121-125.

- Ordidge R.J., Counsell C., Lohman J.A. (1986) Image-selected *in vivo* spectroscopy (ISIS), a new technique for spatial selective NMR spectroscopy. *J.Magn.Reson.* 66:283-294.
- Peck T.L., Magin R.L., Lauterbur P.C. (1995) Design and analysis of microcoils for NMR microscopy. *J.Magn.Reson.B* 108:114-124.
- Peterson, D.M., Duensing, G.R., and Fitzsimmons, J.R. (1997) MRI basics and coil design principle. RF Design 1:56.
- Picard L., Blackledge M., Decors M. (1995) Improvements in electronic decoupling of transmitter and receiver coils. *J.Magn.Reson.Series B* 106:110-115.
- Pierce, G.W. (1920) Electric oscillation and electric waves. New York, McGraw-Hill, pp. 157-175.
- Prichard J.W., Alger J.R., Behar K.L., Petroff O.A., Shulman R.G. (1983) Cerebral metabolic studies *in vivo* by ^{31}P NMR. *Proc.Natl.Acad.Sci.U.S.A.* 80:2748-2751.
- Schnall M.D., Barlow C., Subramanian V.H., Leigh J.S.J. (1986a) Wireless implanted magnetic resonance probes for *in vivo* NMR. *J.Magn.Reson.* 68:161-167.
- Schnall M.D., Barlow C., Summers J.J., Subramanian V.H., Leigh J.S.J. (1986b) Subcutaneous relay implanted magnetic resonance probe. *Proceedings Soc.Magn.Reson.Med.*, 5th Annual Meeting 1:223-224.(Abstract)
- Schnall M.D., Subramanian V.H., Leigh J.S.J., Chance B. (1985a) A new double-tuned probe for concurrent ^1H and ^{31}P NMR. *J.Magn.Reson.* 65:122-129.
- Schnall M.D., Subramanian V.H., Leigh J.S.J., Gyulai L. (1985b) A technique for simulations ^1H and ^{31}P NMR at 2.2T *in vivo*. *J.Magn.Reson.* 63:401-405.
- Schwartz G.G., Steinman S.K., Weiner M.W., Matson G.B. (1992) *In vivo* ^{31}P -NMR spectroscopy of right ventricle in pigs. *Am.J.Physiol.* 262:H1950-4.
- Slichter C.P. (1989) Principles of magnetic resonance. Springer-New York, pp. 11-33.
- Smythe W.R. (1968) Static and dynamic electricity. New York: McGraw-Hill, pp. 291.
- Summers R.M., Hedlund L.W., Cofer G.P., Gottsman M.B., Manibo J.F., Johnson G.A. (1995) MR microscopy of the rat carotid artery after balloon injury by using an implanted imaging coil. *Magn.Reson.Med.* 33:785-789.
- Terman F.E. (1955) Coupled circuits. In: Electronic and radio engineering. New York: McGraw-Hill Book Company, INC, pp. 78-79.
- Vink R., Knoblach S.M., Faden A.I. (1987) ^{31}P magnetic resonance spectroscopy of traumatic spinal cord injury. *Magn.Reson.Med.* 5:390-394.

- Vink R., Noble L.J., Knoblauch S.M., Bendall M.R., Faden A.I. (1989a) Metabolic changes in rabbit spinal cord after trauma: magnetic resonance spectroscopy studies. Ann.Neurol. 25:26-31.
- Vink R., Yum S.W., Lemke M., Demediuk P., Faden A.I. (1989b) Traumatic spinal cord injury in rabbits decreases intracellular free magnesium concentration as measured by ^{31}P MRS. Brain Res. 490:144-147.
- Wirth E.D. (1992) MRI studies of fetal spinal cord transplants. Ph.D. Dissertation, University of Florida.
- Wirth E.D., Mareci T.H., Beck B.L., Fitzsimmons J.R., Reier P.J. (1993) A comparison of an inductively coupled implanted coil with optimized surface coils for *in vivo* NMR imaging of the spinal cord. Magn.Reson.Med. 30:626-633.
- Wirth E.D., Mareci T.H., Teele D.P., Brown S.A., Anderson D.K., Reier P.J. (1989) Magnetic resonance imaging (MRI) of fetal cat neural tissue transplants in the adult cat spinal cord. Soc.Neurosci.Abst. 15:1241.
- Zelaya F.O., Chalk J.B., Mullins P., Brereton I.M. (1996) Localized ^1H NMR spectroscopy of rat spinal cord *in vivo*. Magn.Reson.Imaging 35:449-456.
- Zhou X., Maronpot R.R., Cofer G.P., Hedlund L.W., Johnson G.A. (1994) Studies on bromobenzene-induced hepatotoxicity using *in vivo* MR microscopy with surgically implanted RF coils. Magn.Reson.Med. 31:619-627.

BIOGRAPHICAL SKETCH

Wenhua Xu Ni was born in Pucheng, Fujian Province, People's Republic of China on July 31, 1966. As an honor high school student she was admitted to the Department of Physics, University of Xiamen, Fujian Province, through the standard national college entrance examinations. She received her B.S. in Physics in July 1987 and M.S. in Physics in July 1990. After graduating from the University of Xiamen and before coming to study in the Department of Physics, at the University of Hawaii, Honolulu in 1992, she worked as an electrical engineer at Xiaxin Solid Electronic Ltd., Xiamen, Fujian.

In August 1993, she transferred from the University of Hawaii to the University of Florida to pursue her Ph.D. degree in Physics. She was attracted to Dr. Tom Mareci and Dr. Raymond Andrew's NMR program in the Department of Physics, at the University of Florida. She has worked under the supervision of Dr. Thomas Mareci in the spinal cord research since 1994. As a strategy to broaden her computer skills, she also obtained her concurrent M.S. degree in Computer Information and Science in May 1997.

She was married to Dr. Wenhui Ni on March 16, 1996.

I certify that I have read this study and that in my opinion it conforms to acceptable standards of scholarly presentation and is fully adequate, in scope and quality, as a dissertation for the degree of Doctor of Philosophy.

Thomas H. Mareci

Thomas H. Mareci, Chair
Associate Professor of Physics

I certify that I have read this study and that in my opinion it conforms to acceptable standards of scholarly presentation and is fully adequate, in scope and quality, as a dissertation for the degree of Doctor of Philosophy.

E. R. Andrew

Edward R. Andrew, Cochair
Graduate Research Professor of Physics

I certify that I have read this study and that in my opinion it conforms to acceptable standards of scholarly presentation and is fully adequate, in scope and quality, as a dissertation for the degree of Doctor of Philosophy.

Neil S. Sullivan

Neil S. Sullivan
Professor of Physics

I certify that I have read this study and that in my opinion it conforms to acceptable standards of scholarly presentation and is fully adequate, in scope and quality, as a dissertation for the degree of Doctor of Philosophy.

S. Blackband

Stephen J. Blackband
Associate Professor of Neuroscience

I certify that I have read this study and that in my opinion it conforms to acceptable standards of scholarly presentation and is fully adequate, in scope and quality, as a dissertation for the degree of Doctor of Philosophy.

G. R. Duensing

George R. Duensing
Assistant Scientist of Electrical and Computer Engineering